MODELLING AND DESIGN THEORY OF MULTI-FACETED ANTENNA ARRAYS FOR HEMISPHERICAL SCAN COVERAGE

by

Inas Taymour Khalifa
B.Sc., Cairo University, 1996
M.A.Sc., University of Waterloo, 2000

A THESIS SUBMITTED IN PARTIAL FULFILLMENT
OF THE REQUIREMENTS FOR THE DEGREE OF
DOCTOR OF PHILOSOPHY
in the School
of
Engineering Science

SIMON FRASER UNIVERSITY
Spring 2007

APPROVAL

Name: Inas Taymour Khalifa

Degree: Doctor of Philosophy

Title of thesis: Modelling and Design Theory of Multi-Faceted Antenna Arrays for Hemispherical Scan Coverage

Examining Committee: Dr. Daniel Lee
Chair

Dr. Rodney Vaughan, Senior Supervisor

Dr. James Cavers, Supervisor

Dr. Shawn Stapleton, Supervisor

Dr. Paul Ho, Internal Examiner

Dr. Lotfollah Shafai, External Examiner,
Professor, Electrical and Computer Engineering,
University of Manitoba

Date Defended: January 19, 2007

SIMON FRASER UNIVERSITY library

DECLARATION OF
PARTIAL COPYRIGHT LICENCE

The author, whose copyright is declared on the title page of this work, has granted to Simon Fraser University the right to lend this thesis, project or extended essay to users of the Simon Fraser University Library, and to make partial or single copies only for such users or in response to a request from the library of any other university, or other educational institution, on its own behalf or for one of its users.

The author has further granted permission to Simon Fraser University to keep or make a digital copy for use in its circulating collection (currently available to the public at the "Institutional Repository" link of the SFU Library website <www.lib.sfu.ca> at: <http://ir.lib.sfu.ca/handle/1892/112>) and, without changing the content, to translate the thesis/project or extended essays, if technically possible, to any medium or format for the purpose of preservation of the digital work.

The author has further agreed that permission for multiple copying of this work for scholarly purposes may be granted by either the author or the Dean of Graduate Studies.

It is understood that copying or publication of this work for financial gain shall not be allowed without the author's written permission.

Permission for public performance, or limited permission for private scholarly use, of any multimedia materials forming part of this work, may have been granted by the author. This information may be found on the separately catalogued multimedia material and in the signed Partial Copyright Licence.

The original Partial Copyright Licence attesting to these terms, and signed by this author, may be found in the original bound copy of this work, retained in the Simon Fraser University Archive.

Simon Fraser University Library
Burnaby, BC, Canada

Revised: Fall 2006

Abstract

Hemispherical scan coverage, where the antenna beam may be positioned anywhere above horizon, is required in many applications such as satellite communications, and surveillance and tracking radar systems. This work involves the modelling and design of multi-faceted antenna arrays for providing general hemispherical coverage.

Two classes of multi-faceted antenna arrays are used, namely, pyramids and pyramidal frusta, and four stages of their design process are considered. The first stage concerns the geometric design of the antenna and presents simple and novel methods to determine the optimal antenna geometry. Investigations of how the maximum scan angle is affected by far-field approximation and by the number of faces are also presented.

The second stage focuses on the design of the circularly polarized circular patch antenna element. Its polarization purity is investigated over angular sectors about broadside. The results show that there is a well-defined optimal patch size which produces extremely pure polarization. This size corresponds to specific low values of the relative substrate permittivity.

The third stage deals with the design of the planar array supported by each of the antenna faces. It presents a comparison between the two methods typically used to compute the element spacing over all coverage ranges and using different antenna configurations.

The final stage presents a performance evaluation framework which compares planar, pyramidal, and pyramidal frustum arrays. Four increasingly detailed levels of evaluation are performed: using the geometric structure only; then incorporating the array factor; and finally including both the modelled; and the simulated element patterns. The results demonstrate that the performance advantages of multi-faceted arrays over planar arrays increase as the coverage range becomes wider and/or closer to horizon, and when the directional radiation characteristics of the antenna element are considered. They also show that no clear improvement is gained by using more than about 10 faces, given the added area, cost, and complexity involved. Moreover, under most circumstances, there is no significant difference in performance among pyramids with 4 to 7 faces or among pyramidal frusta with 5 to 9 faces.

Keywords: Antennas, phased array antennas, microstrip antennas, hemispherical coverage, maximum scan angle.

Acknowledgments

I would like to express my gratitude to my senior supervisor, Prof. Rodney Vaughan, for giving me the chance to be a part of his research team. I deeply appreciate the continuous guidance, support, encouragement, and optimism he has shown throughout my program.

I would like to thank my supervisors, Prof. James Cavers and Prof. Shawn Stapleton, for their constructive feedback and valuable suggestions which helped improve the contents and presentation of this work. I would also like to acknowledge the support of Dr. Peter Strickland, of Antenna Science Corporation, for this work.

I would also like to thank my colleagues at the Wireless Communication Lab, especially, Mr. Vadim Antonchik, Dr. Nima Mahanfar, and Ms. Jane Yun.

Last but not least, my deep gratitude goes to my husband and my parents for their constant encouragement, patience, and support.

Contents

List of Tables

List of Figures

List of Symbols

a	The effective radius of the circular patch antenna
D	Directivity
$\tilde{D}$	Geometric directivity
d, d_x, d_y	Element spacing in an antenna array
d_b	Basic element spacing
d_o	Optimal element spacing
$\mathbf{E}^{[n]}$	Far-field pattern of the linearly-polarized nth mode patch antenna
$E_\theta^{[n]}$	θ-component of $\mathbf{E}^{[n]}$
$E_\phi^{[n]}$	ϕ-component of $\mathbf{E}^{[n]}$
E_a	Number of element per array
E_t	Total number of element in a planar, pyramidal, or frustum array
F_A	Isotropic array factor
$F_{co}^{[n]}$	Co-polar pattern
$F_{cr}^{[n]}$	Cross-polar pattern
$\mathbf{f}^{[n]}$	Far-field pattern of the circularly-polarized nth mode patch antenna
$f_\theta^{[n]}$	θ-component of $\mathbf{f}^{[n]}$
$f_\phi^{[n]}$	ϕ-component of $\mathbf{f}^{[n]}$
f_0	Free-space center frequency
G	Gain
J_n	Bessel function of the first kind and nth order
J_n'	Derivative of Bessel function of the first kind and nth order
k	Wave number
k_0	Free-space wave number

L	Scan loss
L_m	Mismatch loss
N	Total number of faces (arrays) in a pyramid or a frustum
n	Patch mode
R	Footprint radius
$R^{[n]}$	Cross polarization ratio (linear scale) for mode n
$R_{\mathrm{dB}}^{[n]}$	Cross polarization ratio (dB scale) for mode n
R_{BW}	Ratio of broadside to scanned beamwidth for mode n
$R_{\max}^{[n]}$	Maximum cross polarization ratio for mode n
$\overline{R}^{[n]}$	Distributed cross polarization ratio for mode n
γ_f	Maximum scan angle encountered by a pyramidal frustum array
γ_l	Maximum scan angle encountered by a planar array
γ_p	Maximum scan angle encountered by a pyramidal array
ϵ_r	Relative permittivity
θ_1	Minimum zenith angle in a hemisherical coverage range
θ_2	Maximum zenith angle in a hemisherical coverage range
$\theta_{3\mathrm{dB}}$	3-dB beamwidth
θ_b	Zenith angle at the border between the coverage areas of the top and side faces in a pyramidal frustum
λ	Wavelength
λ_0	Free-space wavelength
ρ_C	Circular polarization ratio
τ_a	Amplitude tolerance
τ_f	Feed position tolerance
τ_p	Phase shift tolerance
ϕ_s	Angle subtended by a side face in a pyramid or a frustum
ϕ_0	Feed position in a circular patch antenna
ψ_f	Elevation angle of the side faces in a pyramidal frustum
ψ_p	Elevation angle of the side faces in a pyramid
ω	Radian frequency

Chapter 1

Introduction

Hemispherical scan coverage refers to the ability to position the antenna beam, and hence transmit or receive a communication signal using the gain of the beam, in any direction above horizon. It is required for many applications such as satellite communications, including navigation and search and rescue systems, surveillance and tracking systems, radio astronomy, and military warning systems. One way to achieve hemispherical scan coverage is to use multiple, adequately positioned, phased array antennas, i.e., multi-faceted antenna arrays.

This research involves the design of multi-faceted antenna arrays for hemispherical scan coverage. The benefits and structure of multi-faceted antenna arrays are first described, followed by an overview of their existing and potential applications. The motivations for this research are then identified, and the original contributions are briefly outlined.

1.1 Phased Array Antennas

A phased array antenna consists of multiple stationary antennas, called antenna elements. In a transmitting antenna, each element is excited using an electric current with a possibly variable amplitude and/or variable phase or time delay. Manipulation of the relative amplitudes of element excitations allows shaping the far-field pattern produced by the array. On the other hand, manipulation of the relative time delays allows scanning, or directing, the beam produced by the array to different directions in space.

Antenna arrays can by used instead of fixed aperture antennas, such as reflectors, in a variety of applications. This is due to their ability to: (a) realize apertures that may be expensive, difficult, or even impossible to realize using a single fixed aperture antenna; (b) allow shaping of the far-field pattern; and (c) produce beams that can be re-positioned electronically.

Large apertures are required to achieve high spatial resolution in radio astronomy applications, for example, where the requirement of aperture diameters of several kilometers is not uncommon [Fourikis, 1997]. Realizing such large apertures would be practically impossible, let alone mechanically steering them toward specific directions. Even if it were possible, the cost would be prohibitive, as the aperture area is typically directly related to cost. In such scenarios, thinned array antennas can be used, where the extent of thinning can be governed by the system budget. For example, the very large array (VLA) radio astronomy facility [Napier et al., 1983] consists of 27 25-meter reflector antennas arranged in a Y-shaped array. The length of each arm of the Y is about 21 kilometers.

Array antennas can also be used to produce far-field patterns with highly directive main beams and low side lobes, required by satellite ground stations, for example. They can be less expensive than fixed apertures and easy to manufacture, e.g., using microstrip antenna elements. Moreover, the electronic scanning capability of array antennas makes them suitable for surveillance and radar applications. For example, they can replace the reflectors which are continuously mechanically-rotated in azimuth to perform detection and tracking at airports. Electronic scanning can be done much faster than mechanical steering, while requiring minimal maintenance.

The main disadvantage of array antennas is the deformation of the far-field pattern as the main beam is scanned away from the broadside direction (perpendicular to the array). As the scan angle increases, the antenna gain decreases and the width of its main beam increases. This drawback can be alleviated to a great extent by using multi-faceted arrays.

The receive performance of high gain antenna arrays is often measured as a signal-to-noise ratio, or specifically as the gain-to-noise temperature ratio, G/T. The gain is achieved by the structure of the antenna, comprising the array directivity and element gain, and is reduced by factors such as mutual coupling, element ohmic loss, feed ohmic loss, and impedance mismatch (linked somewhat to the mutual coupling). The noise temperature has contributions from how the receiving beam is illuminated by noise sources (antenna noise); for example the sky has a temperature of about 3°K, and the earth is about 290°K. The temperature also has contributions from ohmic losses in the elements and in the feed between the elements and the receiver, and finally from the receiver itself. So losses are important because they contribute twice in the G/T performance metric- both in reducing the gain and also in increasing the noise power. For example, a 2dB loss in each of the elements with feeds will contribute -2dB to the gain and +2dB to the noise, so the G/T changes by -4dB. In this thesis, these losses are not explored further; the research emphasis is directed towards the array geometric configuration and the performance metric is generally confined to only the geometric directivity. For the element example, discussed in Chapter 3, again the ohmic losses are not addressed, just the polarization loss in the sense of optimizing the polarization purity, and the feeding accuracy for the circular polarization modes. So the performance metrics in this thesis are essentially independent of the losses in the feeds and elements. However, the choice of substrate permittivity for the element size, addressed in Chapter 3, has some impact on the losses in the sense that this choice influences the choice of substrate (and the substrate losses) and may also affect the mutual coupling, depending on how the antennas are built. It should also be noted that the scan loss, which is modelled here from established experimental results, actually includes some mutual coupling impact. To summarize, it is emphasized that it is the array geometry that is being addressed, and that the element, feed and mutual coupling losses are not treated directly in this thesis.

The thesis also focuses on high directivity (about 20dB or higher) arrays. This means that obstacles and the mounting platform do not have a major impact on the beams, with the possible exception of the details such as the off-beam cross-polarization of Chapter 3. For low directivity arrays (about 10dB or lower) there are fewer elements of course and the impact of nearby physical obstacles and the likely stronger presence of the far field intersecting the earth, will be greater than for the high directivity case. So the low gain array has some different design issues from the high gain array, and the specific issues for low gain design are not explicitly addressed in the thesis.

1.1.1 Multi-Faceted Antenna Arrays

In order for a single planar array to allow full elevation and azimuth, or full hemispherical coverage, expressed as:

$$\{(\theta, \phi) : \theta \in [0, \frac{\pi}{2}], \phi \in [0, 2\pi)\}, \tag{1.1}$$

its main beam will need to be scanned by up to 90° away from broadside. In practice, however, the losses incurred when the main beam is scanned to such an extent are prohibitive, as outlined in Section A.5.3. Multi-faceted antenna arrays are composed of multiple, adequately arranged, phased array antennas. They allow sectoral coverage, where the hemispherical coverage requirement in (1.1) is divided among the antenna faces. Sectoral coverage significantly reduces the angular interval over which the main beam from each array is to be scanned, and consequently the losses are reduced, relative to a single planar array.

This work concerns two classes of multi-faceted antenna arrays, namely, pyramids and pyramidal frusta. Sample schematics of both structures are shown in Figure 1.1.

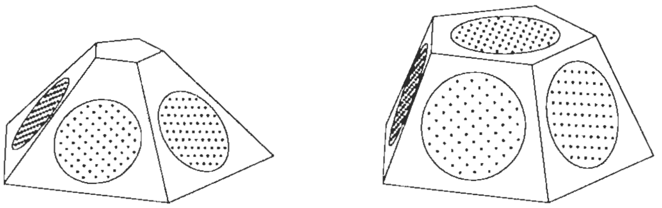

(a) 5-face pyramid

(b) 6-face pyramidal frustum

Figure 1.1: Schematics of a 5-face pyramidal and a 6-face pyramidal frustum antenna array.

In the figure, each face supports a planar array with a circular aperture. However, in practice, any aperture shape may be used. The individual antenna elements are shown as dots. Moreover, the planar facets need not be connected, and may be spatially distributed such as on a ship board, e.g., [Felstead, 2000], instead. Such arrangements still "logically" resemble pyramids (a collection of tilted side-facing arrays) or pyramidal frusta (multiple tilted side-facing arrays plus a zenith-facing array). Therefore, almost all the results derived for pyramids and pyramidal frusta apply to these arrangements, and the terms pyramids and pyramidal frusta are used here to refer to both connected and non-connected arrays.

1.1.2 Conformal Antenna Arrays

Conformal antenna arrays present an alternative for achieving hemispherical scan coverage. They include singly- or doubly-curved surfaces, such as cylinders and spheres, respectively. Conformal arrays may also be approximated by planar facets, such as the half-sphere approximation proposed in [Brandwood, 1998] and the cone approximation used in [Caille et al., 2002].

Both conformal and multi-faceted arrays have their advantages and disadvantages. Multi-faceted arrays inherit from planar arrays, and thus their advantages over conformal arrays include: well-established technologies that have matured over the past few decades, simpler analysis, simpler beam control, lower cross polarization, and easier manufacturing and packaging of their electronic components using printed circuit technology. Conformal arrays, on the other hand, offer relatively lower scan losses and wider bandwidth than multi-faceted arrays [Josefsson and Persson, 2006], in addition, of course, to their ability to seamlessly conform to aerodynamic structures. The scope of this work is limited to the multi-faceted arrays.

1.2 Applications of Multi-Faceted Antenna Arrays

Early applications of multi-faceted antenna arrays were limited to defense systems. However, as the cost of antenna arrays continues to decrease, applications now include civilian and commercial systems, as elaborated below and summarized in Table 1.1.

Examples of existing applications include the missile site radar (MSR) system and the PAVE phased array warning system (PAWS). The MSR system, built in the 1970s, provides hemispherical coverage. It is a 4-face pyramid supporting identical planar arrays each containing 5000 radiating elements and has a diameter of about 4 meters and a face elevation angle of 65° [Bell Laboratories, 1975]. The PAVE PAWS system was designed for warning of missiles and satellite tracking [Hoft, 1978]. It is composed of two arrays which together cover 240° in azimuth (i.e., 2 faces of a 3-face pyramid). Each array has a diameter of about 31 meters and contains 1792 crossed dipoles over a conducting ground plane [Fourikis, 1997].

Table 1.1: Examples of existing and potential applications of multi-faceted antenna arrays.

Area	Applications
Military and defense	• Missile site radar system [Bell Laboratories, 1975]. • PAVE PAWS warning system [Hoft, 1978].
Satellite communications	• High-performance GPS receiver for radio navigation and landing help at commercial airports [Padros et al., 1997]. • LEO satellites [Caille et al., 2002].
Mobile satellite communications	• Communication to landrovers moving over rough terrain [Brandwood, 1998]. • Multiple Shipboard SATCOM antennas [Felstead, 2000] • Satellite tracking for aeronautical SATCOM [Miura et al., 2002]. • Replacing motorized gimbaled reflector antennas [Targonski, 2004] for SOTM.
Radar	• Horizon [Trunk and Patel, 1997] and volume-scanning surveillance [Waters et al., 1998], [Trunk, 2003]. • Shipboard and land-based antennas for tracking and discrimination [Jablon and Agrawal, 2006].
Wireless LANs	• Remote terminals of indoor wireless LAN systems [Ihara et al., 1997].
Radio astronomy	• Replacement for NASA's Deep Space Network 70-meter reflector antenna [Jamnejad et al., 2002].

The use of multi-faceted antenna arrays has also been proposed for a variety of applications. Padros, et al. (1997), investigated the use of a multi-faceted antenna composed of two stacked 6-face pyramids for a high-performance global positioning system (GPS) receiver to be used at commercial airports for navigation and landing help. Caille, et al. (2002), demonstrated the use of a 24-face pyramidal antenna, which conforms to a low earth orbit (LEO) satellite. Each array was composed of six microstrip patch antennas. The antenna covered 360° in azimuth and 0° to 62° in elevation, and allowed forming up to three simultaneous beams to enable communication with several ground stations.

Applications in mobile satellite communications include using an antenna made up of 6 faces of a dodecahedron (12-face polyhedron) for satellite communication (SATCOM) to landrovers moving over rough terrain [Brandwood, 1998], and for providing aeronautical SATCOM [Felstead, 2000], [Miura et al., 2002]. Multi-faceted antenna arrays can potentially replace motorized gimbaled reflector antennas mounted on mobile terminals [Targonski, 2004] to provide satellite communications on-the-move (SOTM).

Multi-faceted antenna arrays were also proposed for use as active phased array radars. Applications include horizon surveillance [Trunk and Patel, 1997] (i.e., scanning in azimuth only), volume-scanning surveillance [Waters et al., 1998], [Trunk, 2003], and shipboard and land-based tracking and discrimination [Jablon and Agrawal, 2006] (the coverage requirement per face of the former exceeds that of the latter).

The use of a 4-face pyramidal array for remote terminals of indoor wireless LAN systems was demonstrated in [Ihara et al., 1997], where circularly polarized patch antenna elements were used to suppress unwanted multi-path. Jamnejad, et al. (2002), investigated the use of a 4-face pyramid and a 7-face pyramidal frustum antenna to replace the current 70-meter reflector antenna used for NASA's Deep Space Network [Imbriale, 2003]. Finally, multi-faceted arrays may be used in smart antenna systems, where multiple independent beams may be produced simultaneously by a single or multiple faces.

As a final note on applications, it should be noted that the indoor propagation environment is very different from that of satellite and most radar environments. For indoor, there is dense multipath. Different beamforming algorithms would probably be used (for example optimal combining), and the number of uncorrelated elements becomes more important than the size of the array aperture, for the performance. However, for future systems, we can expect much higher frequencies than are currently used for indoor systems. In this case, the spatially directive beams, addressed in this thesis, may have an advantage, because they would be able to illuminate selectively the individual target users in a room, and this would give a simple method of increasing the Signal-to-Noise-plus-Interference Ratio (SNIR) for each link and therefore increase the system capacity.

1.3 Motivation and Approach

Antenna arrays make different forms of wireless communication possible. Research in the area of antennas and antenna arrays, in general, is fueled by the need for more efficient and compact antenna systems. Such systems are required to satisfy an ever increasing demand for high bandwidth wireless applications from a rapidly growing customer base.

In particular, this research is motivated by the need for hemispherical scan coverage for many communications applications, and the ability to achieve it using multi-faceted antenna arrays, as elaborated in Section 1.2. Research in multi-faceted antenna arrays and their applications started as early as the 1960s, e.g. [Knittel, 1965] and [Kefalas, 1965], and continues to be active, e.g. [Jablon and Agrawal, 2006], as will be shown in Chapters 2 and 5.

This work deals with four stages involved in the design of multi-faceted antenna arrays. The first stage is concerned with the geometric design of the antenna, which is mainly governed by the scan coverage requirements. Concepts from geometric optics are used to determine the optimal face elevation of the antenna faces. The work in this stage is motivated by the need for optimal algorithms to determine the geometry of pyramidal and pyramidal frustum antenna arrays, given a general hemispherical coverage requirement. More details about previous work in this stage are be given in Chapter 2.

The second stage focuses on the design of the antenna element used here, which is the circularly polarized circular patch antenna. The use of the circular patch antenna is motivated by its low profile, light weight, compactness, and ease of manufacturing and integration with other circuit elements [Waterhouse, 2003]. Circular polarization is essential for many applications, such as satellite communications, as will be shown in Chapter 3. The investigation of the circular polarization purity of the patch antenna is motivated by the lack of such a study in the literature and its importance for designing multi-faceted antenna arrays.

The third stage deals with the design of the individual antenna array, which is supported by each of the antenna faces. The design of phased array antennas is a very extensive and mature research area that has been addressed by numerous excellent texts, e.g., [Mailloux, 1994] and [Hansen, 1998]. Therefore, the work in this stage aims at choosing the array parameters that suit the nature of multi-faceted antennas, and assessing the state of the art in this area.

The final stage involves the evaluation of the performance of multi-faceted antenna arrays. The evaluation aspect of this work is motivated by the lack of a comprehensive framework that uses widely applicable cost functions to compare the performance of planar, pyramidal, and pyramidal frustum antenna arrays. As will be elaborated in Chapter 5, previous work only dealt with a limited number of antenna structures, mostly pyramids, and often presented results that are only useful for the underlying case studies.

1.4 Contributions

Designing any antenna requires multiple experimental iterations. This research builds upon and improves the state of the art in designing multi-faceted antenna arrays, and aims at providing efficient paths to first cut designs to minimize the number of experimental iterations. The contributions of this research to the four design stages outlined in Section 1.3, are briefly introduced here and elaborated in the following chapters. They include:

- Simple and novel methods to determine the optimal geometry of pyramids and pyramidal frusta given a general hemispherical scan coverage requirement, and investigations of how the maximum scan angle is affected by the far-field approximation and by the number of faces.

- An investigation of the circular polarization purity of the circular patch antenna over angular sectors about the antenna broadside and its relationship to the patch size and construction. The results presented are not only applicable to multi-faceted antennas, but also to a wide variety of wireless and mobile communications applications that use circular polarization.
- A comparison between the two methods typically used to compute the element spacing in the individual face arrays over all valid hemispherical coverage ranges and how they are affected by the number of faces.
- A performance evaluation framework which compares planar, pyramidal, and pyramidal frustum antenna arrays at four increasingly detailed levels. The levels include using the geometric structure only, then incorporating the isotropic array factor, and finally including both the modelled and simulated far-field patterns of the patch antenna element.

1.5 Organization of The Thesis

This thesis is organized as follows. Chapters 2 through 5 present the contributions of this work to the four design stages. Detailed information about previous work in each stage is presented in the respective chapter. Chapter 2 involves the geometric design of pyramidal and pyramidal frustum antenna arrays and introduces new techniques to determine their optimal configurations. Chapter 3 investigates the circularly polarized circular patch antenna used as the antenna element, presents a thorough evaluation of its polarization performance, and outlines the criteria for selecting the patch dimensions that optimize polarization purity. Chapter 4 focuses on the design of the planar arrays supported by the antenna faces and explains how to select the array parameters of multi-faceted antenna arrays for the purpose of performance evaluation. Chapter 5 presents the comprehensive evaluation framework used to compare the performance of planar, pyramidal, and pyramidal frustum antenna arrays. A summary of contributions and conclusions are given in Chapter 6.

Three appendices are provided. Appendix A presents some basic background information in the theory of antennas and antenna arrays which is frequently referred to throughout the thesis. Appendix B presents information about the numerical methods used in the geometric design stage. Finally, Appendix C describes how the dimensions of pyramids and pyramidal frusta are computed for use in the geometric design and performance evaluation stages.

Chapter 2

Geometric Design of Multi-Faceted Arrays

This chapter addresses the problem of optimizing the geometric design of multi-faceted antenna arrays. Two classes of multi-faceted antenna arrays are considered, namely, pyramids and pyramidal frusta. The optimization involves choosing the face elevation which minimizes the overall maximum scan angle encountered by the arrays, given a general hemispherical scan coverage requirement. Firstly, the geometric structure of the antenna arrays and the corresponding sectoral coverage criteria are described. Secondly, an overview of previous research in this area is presented. Thirdly, two methods for determining the optimal face elevation of the arrays are described and compared. The first method is based on the traditional approach of equalizing the maximum scan angles. The second method introduces a novel approach based on minimax optimization. Finally, a discussion of the lower bounds on the maximum scan angles, and how the maximum scan angle is affected by the number of faces in each structure is presented.

2.1 Antenna Structure and Scan Requirement

A multi-faceted antenna array is simply a convex polyhedron. A polyhedron is a three-dimensional solid that consists of polygons joined at their edges. A line that connects any two non-coplanar points on the surface of a convex polyhedron always lies within the interior of the polyhedron. This work is only concerned with two classes of convex polyhedra, namely, regular right pyramids and their frusta.

A regular right pyramid (or pyramid for brevity) is a polyhedron where: (a) one face, the base, is a regular N-sided polygon, (b) all other N side faces are identical isosceles triangles that meet at a common apex, and (c) the axis connecting the apex and the centroid of the base is perpendicular to the base [Weisstein, 2003]. A pyramidal antenna array supports arrays on its side faces. An example of a 5-face pyramid is shown in Figure 2.1(a).

On the other hand, the frustum of a regular right pyramid (or pyramidal frustum for brevity) is a frustum made by truncating the top of the pyramid. The base and top faces are regular $(N-1)$-sided polygons, while the $(N-1)$ side faces are isosceles trapezoids. In a pyramidal frustum structure, antenna arrays are mounted on the side faces, as well as the top face of the pyramid. The addition of the top array reduces the elevation scan requirement for the side arrays, and hence reduces the overall maximum scan angle. Figure 2.1(b) illustrates an example of a 6-face pyramidal frustum.

Without loss of generality, it can be assumed that the base of either structure lies in the xy-plane, its axis is the z-axis, and its first side face is aligned with the xz-plane as shown in Figure 2.1. Moreover, each side face subtends an azimuthal angle, ϕ_s,

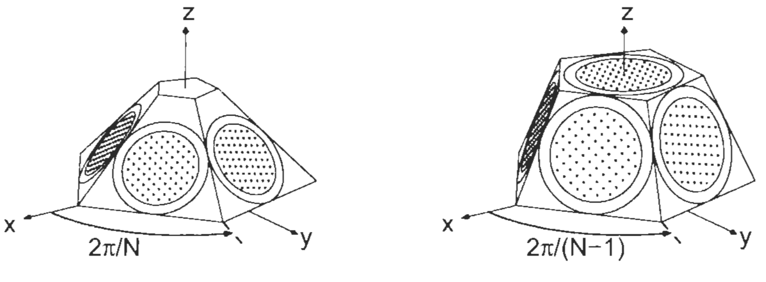

(a) 5-face pyramid (N=5) (b) 6-face pyramidal frustum (N=6)

Figure 2.1: The structure of (a) the pyramidal and (b) the pyramidal frustum antenna array. Both antenna arrays occupy a footprint of the same radius and use the optimal face elevation. Each structure supports identical arrays on all of its faces.

which is given by:

$$\phi_s = \begin{cases} \frac{2\pi}{N} & \text{for a pyramid,} \\ \frac{2\pi}{(N-1)} & \text{for a pyramidal frustum,} \end{cases} \tag{2.1}$$

where N is the total number of faces (or arrays) in the structure.

Figures 2.2(a) and 2.2(b) illustrate the full and general hemispherical scan coverage requirements, respectively. Using spherical coordinates, general hemispherical coverage can be expressed as the angular interval:

$$\{(\theta, \phi) : \theta \in [\theta_1, \theta_2], 0 \leqslant \theta_1 < \theta_2 \leqslant \frac{\pi}{2}, \phi \in [0, 2\pi)\}. \tag{2.2}$$

For full (zenith to horizon) coverage, θ_1=0 and θ_2=$\pi/2$. Using a pyramidal array, the scan requirement is divided among the N side faces of the pyramid using a simple criterion: use face i when $\phi \in ((i-1)\frac{2\pi}{N}, i\frac{2\pi}{N}]$, regardless of θ. This criterion is illustrated in Figures 2.2(c) and 2.2(d) for the 5-face pyramid in Figure 2.1(a). The coverage area of each face is bordered by thick lines.

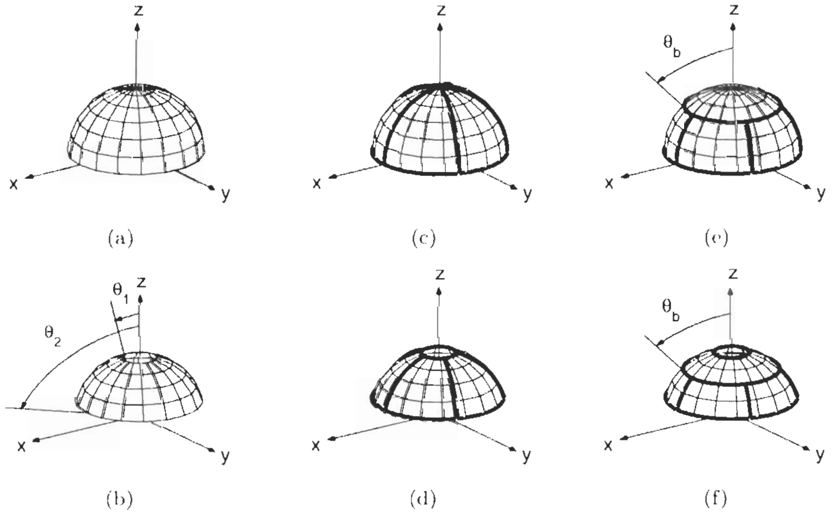

(a) (c) (e)

(b) (d) (f)

Figure 2.2: Illustration of the (a) full, and (b) general hemispherical scan coverage requirement, and the corresponding sectoral coverage criteria using a 5-face pyramid (c and d), and a 6-face pyramidal frustum (e and f).

For the pyramidal frustum, face 1 (the top face) is used when $\theta \in [\theta_1, \theta_b)$, while the ith side face, i=2 . . . N, is used when $\theta \in [\theta_b, \theta_2]$ and $\phi \in (i-2)\frac{2\pi}{N-1}, (i-1)\frac{2\pi}{N-1}]$. These criteria are shown in Figures 2.2(e) and 2.2(f) for the 6-face frustum in Figure 2.1(b), for the full and general coverage requirements, respectively. The value of θ_b is set such that the maximum scan angle is minimized. Other criteria for sectoral coverage by the pyramidal frustum were used in [Knittel, 1965]. However, the criteria used here, which are the same as in [Kmetzo, 1967], are simpler.

2.2 Previous Work

Research in optimizing the geometry of pyramidal and pyramidal frustum antenna arrays began as early as the 1960s and has continued to be active since then. The optimization process involves choosing the elevation angle, ψ, of the side faces of either structure. This was typically accomplished by equalizing the maximum off-axis scan angles, in order to minimize the overall maximum scan angle, γ. This approach is referred to below as the equalization-based approach. Determining the optimal number of faces of pyramids and pyramidal frusta is a more involved process, that can be approached using many different figures of merit, e.g., scan loss and number of antenna elements. A detailed discussion of this process is given in Chapter 5.

Knittel (1965) computed the face elevation of 3- and 4-face pyramids and 5- and 6-face pyramidal frusta, with the aid of stereographic projection, given a full hemispherical scan coverage requirement. Kmetzo (1967) used geometric transformations to determine the face tilt (which is the complementary angle of ψ) of N-face pyramids and N-face pyramidal frusta. He only considered full hemispherical coverage and showed that as $N \to \infty$, the maximum scan angles can not be reduced beyond 45° and 30° for the pyramids and pyramidal frusta, respectively.

Corey (1985) proposed a graphical, iterative technique to determine the face elevation and element spacing of a single phased array for a given scan requirement (This single array can represent one face in a multi-faceted antenna). A graph is obtained by projecting the scan requirement for the array on the plane, and the face elevation is determined graphically based one of two criteria. The first criterion involves minimizing the maximum scan angle, while the other criterion involves minimizing the total number of array elements (i.e., maximizing the element spacing), such that grating lobes do not appear in visible space. The designs resulting from the two criteria are not the same. In other words, the former is equalization-based, while the latter is not. The latter criterion results in a larger maximum scan angle, and hence more scan losses, as will be seen in Chapter 5. Waters, et al. (1998) applied Corey's method to determine the face elevation of 3-, 4-, and 5-face pyramidal active array radars for coverage extending from zenith (θ_1=0°) to horizon (θ_2=90°) or to 45° elevation (θ_2=45°).

Felstead (2000) used an approach similar to that of Kmetzo to compute the elevation of collections of 3-, 4-, and 5-side facing antennas and 3-, 4-, and 5-side facing antennas plus a zenith-facing antenna, distributed around a ship. The geometry is thus equivalent to that of pyramids and pyramidal frusta, respectively. He considered full hemispherical coverage with and without roll and pitch effects. He determined the elevation angles numerically using a symbolic mathematics software. Jablon and Agrawal (2004) provided an expression to compute the face elevation of N-face pyramids given a general hemispherical coverage requirement. Their derivation was based on Kmetzo's technique and was provided in [Jablon and Agrawal, 2006]. They also used Corey's graphical approach to determine the face elevation which maximizes the element spacing for 3- and 4-face pyramids.

The contributions of previous research are summarized in Table 2.1. The table shows that the face elevation of N-face pyramidal frusta for the case of general hemispherical coverage requirement has not been addressed before. It will be addressed in Section 2.3. It also shows that almost all methods are equalization-based, except for Corey's method that maximizes the element spacing at the expense of a larger maximum scan angle. It will be demonstrated in Section 2.3.2 that the equalization-based approach is not always optimal, and a new optimal approach will be presented.

Table 2.1: A summary of previous work in determining the face elevation of pyramidal and pyramidal frustum antenna arrays.

Source	Structure	Coverage	Approach
Knittel (1965)	3- and 4-face pyramids and 5- and 6-face pyramidal frusta	Full	Equalization-based
Kmetzo (1967)	N-face pyramids and N-face pyramidal frusta	Full	Equalization-based
Corey (1985)	A single array	General	Equalization-based or maximum element spacing†
Felstead (2000)	3-, 4- and 5-face pyramids and 4-, 5- and 6-face pyramidal frusta	General	Equalization-based
Jablon and Agrawal (2004)	N-face pyramids	General	Equalization-based

† The maximum element spacing criterion is explained in Section 2.2.

2.3 Optimal Face Elevation

The face elevation, ψ, of the side faces of the pyramid or the pyramidal frustum minimizes the overall maximum scan angle, γ. The subscripts "p" and "f" are used below to refer to the pyramid and the frustum, respectively. This section presents a direct approach to determine the face elevation of N-face pyramids, ψ_p, that is simpler than that used in [Kmetzo, 1967] and [Jablon and Agrawal, 2006]. The approach is then extended to N-face pyramidal frusta, and is applicable to both full and general hemispherical coverage.

In a pyramidal structure, since all of the side faces are identical, γ_p is the maximum scan angle encountered by any of the faces. Figures 2.3(a) and 2.3(b) depict the geometry of the whole pyramid and its first face, respectively. The face elevation angle $\psi_p = \angle op_1p_1$ and the corresponding normal vector to the face, $\hat{n}_{p_1}$, are shown in Figure 2.3(c).

If full hemispherical coverage is required, it is clear that the maximum scan angle

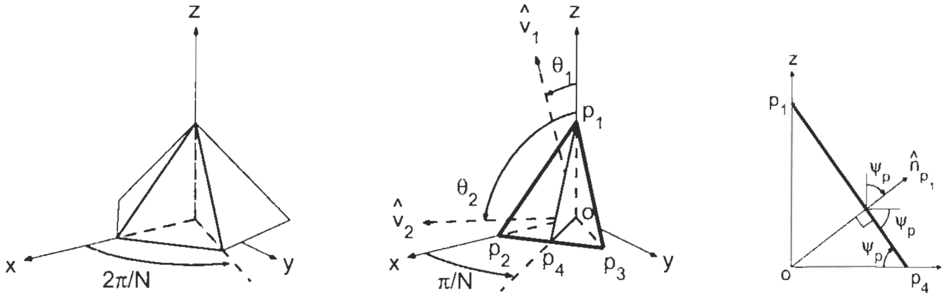

(a) Pyramid (b) First face (c) Face elevation

Figure 2.3: The geometry of a pyramidal array: (a) a 5-face pyramid, (b) the first pyramid face and elevation scan requirement, θ_1 and θ_2, and (c) the face elevation and face normal vector.

occurs when the main beam is scanned from the broadside direction, $\hat{n}_{p_1}$, to either of the three directions $o\vec{p}_1$, $o\vec{p}_2$, or $o\vec{p}_3$. These directions correspond to the (θ, ϕ) pairs: $(0, 0)$, $(\frac{\pi}{2}, 0)$, and $(\frac{\pi}{2}, \frac{2\pi}{N})$. On the other hand, for the case of general coverage, γ_p occurs when the antenna beam is scanned from broadside to the corners of the coverage area of the face, i.e., the (θ, ϕ) pairs: $(\theta_1, 0)$, $(\theta_1, \frac{2\pi}{N})$, $(\theta_2, 0)$, and $(\theta_2, \frac{2\pi}{N})$. Owing to symmetry about the shaded plane Δop_4p_1, only two directions need to be considered. In other words, γ_p occurs when the beam is scanned from $\hat{n}_{p_1}$ to either $\hat{v}_1$ or $\hat{v}_2$. Assuming that the distance from the target to the antenna is sufficiently large, and hence, the antenna dimensions can be neglected (far-field case), these unit vectors are given by:

$$\begin{aligned} \hat{n}_{p_1} &= \cos\tfrac{\pi}{N}\sin\psi_p\hat{x} + \sin\tfrac{\pi}{N}\sin\psi_p\hat{y} + \cos\psi_p\hat{z}, \\ \hat{v}_i &= \sin\theta_i\hat{x} + \cos\theta_i\hat{z}, \qquad i = 1, 2, \end{aligned} \tag{2.3}$$

where $\hat{x}$, $\hat{y}$, and $\hat{z}$ are unit vectors along the x, y, and z axes, respectively. The maximum scan angle of the pyramid, γ_p, is thus given by the max-function, e.g., [Borwein and Lewis, 2000]:

$$\gamma_p = \max_{i=1,2} \gamma_{p_i}, \tag{2.4}$$

where

$$\gamma_{p_i} = \cos^{-1}\hat{n}_{p_1}.\hat{v}_i = \cos^{-1}\left(\cos\frac{\pi}{N}\sin\psi_p\sin\theta_i + \cos\psi_p\cos\theta_i\right). \tag{2.5}$$

Similarly, for the pyramidal frustum, the overall maximum scan angle, γ_f, is the maximum of the scan angle encountered by the top face and that encountered by any of the side faces. Figure 2.4 depicts the first (top) and second (side) faces of the frustum. For the top face, the maximum scan angle occurs when the antenna beam is scanned from the broadside direction (or zenith), $\hat{n}_{f_1}=\hat{z}$, to the borders of its coverage area, $\hat{v}_1$ and $\hat{v}_b$. However, since $\theta_1 < \theta_b$, only $\hat{v}_b$ needs to be considered. Therefore, the maximum scan angle for the top face is:

$$\gamma_{f_1} = \cos^{-1} \hat{n}_{f_1}.\hat{v}_b = \cos^{-1} \cos\theta_b = \theta_b. \tag{2.6}$$

For the side face, owing to the symmetry about the shaded plane, which contains the face elevation angle $\psi_f = \angle op_4p_1$, maximum scan occurs when the antenna beam is scanned from the broadside direction, $\hat{n}_{f_2}$, to either $\hat{v}_b$ or $\hat{v}_2$, where,

$$\begin{aligned} \hat{n}_{f_2} &= \cos\tfrac{\pi}{N-1}\sin\psi_f\hat{x} + \sin\tfrac{\pi}{N-1}\sin\psi_f\hat{y} + \cos\psi_f\hat{z}, \\ \hat{v}_b &= \sin\theta_b\hat{x} + \cos\theta_b\hat{z}, \end{aligned} \tag{2.7}$$

and $\hat{v}_2$ is given in (2.3). Therefore, the maximum scan angle for the side face is the largest of either:

$$\begin{aligned} \gamma_{f_2} &= \cos^{-1}\hat{n}_{f_2}.\hat{v}_b &= \cos^{-1}\left(\cos\tfrac{\pi}{N-1}\sin\psi_f\sin\theta_b + \cos\psi_f\cos\theta_b\right), \\ \gamma_{f_3} &= \cos^{-1}\hat{n}_{f_2}.\hat{v}_2 &= \cos^{-1}\left(\cos\tfrac{\pi}{N-1}\sin\psi_f\sin\theta_2 + \cos\psi_f\cos\theta_2\right). \end{aligned} \tag{2.8}$$

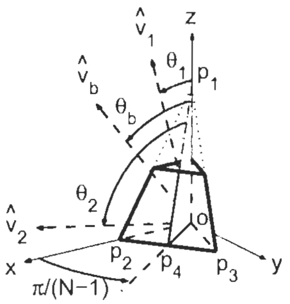

Figure 2.4: The geometry of a pyramidal frustum. The face elevation, ψ_p, is measured in the shaded plane as $\angle op_4p_1$. In the xz-plane, θ_1 and θ_2 denote the elevation scan requirement. The angle θ_b defines the border between the coverage areas of the top and side faces.

Thus, the maximum scan angle of the pyramidal frustum, γ_f, is given by the max-function:

$$\gamma_f = \max_{i=1,2,3} \gamma_{f_i}. \tag{2.9}$$

2.3.1 The Equalization-Based Approach

Pyramidal Arrays

In previous research, e.g., [Knetzo, 1967], [Corey, 1985], [Jablon and Agrawal, 2006], [Khalifa and Vaughan, 2006b], the face elevation was obtained by equalizing the maximum off-axis scan angles. For the pyramidal antenna array, this is done by equating the angles γ_{p_1} and γ_{p_2} given by (2.5). The resulting face elevation and maximum scan angle for general hemispherical coverage are computed as follows [Khalifa and Vaughan, 2006b]. Since the number of faces of the pyramid, N, is at least 3, then γ_{p_1} and γ_{p_2} are acute angles. Moreover, since the cosine function is monotonically decreasing in the interval $[0°, 90°]$, then instead of equating $\cos^{-1} \hat{n}_{p_1}.\hat{v}_1$ and $\cos^{-1} \hat{n}_{p_1}.\hat{v}_2$, one can equate:

$$\begin{aligned} \hat{n}_{p_1}.\hat{v}_1 &= \hat{n}_{p_1}.\hat{v}_2 \\ \cos\tfrac{\pi}{N}\sin\psi_p\sin\theta_1 + \cos\psi_p\cos\theta_1 &= \cos\tfrac{\pi}{N}\sin\psi_p\sin\theta_2 + \cos\psi_p\cos\theta_2 \\ \sin\psi_p\cos\tfrac{\pi}{N}(\sin\theta_1 - \sin\theta_2) &= \cos\psi_p(\cos\theta_2 - \cos\theta_1). \end{aligned} \tag{2.10}$$

Therefore, the face elevation and the corresponding scan angle are given by:

$$\begin{aligned} \psi_p &= \tan^{-1}\tfrac{\cos\theta_1 - \cos\theta_2}{\cos\frac{\pi}{N}(\sin\theta_2 - \sin\theta_1)}, \\ \gamma_p &= \cos^{-1}\left(\cos\tfrac{\pi}{N}\sin\psi_p\sin\theta_1 + \cos\psi_p\cos\theta_1\right). \end{aligned} \tag{2.11}$$

Figures 2.5(a) and 2.5(b) plot the face elevation, ψ_p, and the maximum scan angle, γ_p, of the pyramid versus N, respectively, for four different coverage ranges. The figure shows that ψ_p and γ_p decrease as N increases. However, the rate of decrease becomes negligible for N larger than about 7.

Pyramidal Frustum Arrays

For the pyramidal frustum, only the full hemispherical coverage requirement has been treated [Knetzo, 1967], while the general coverage case has not been addressed before.

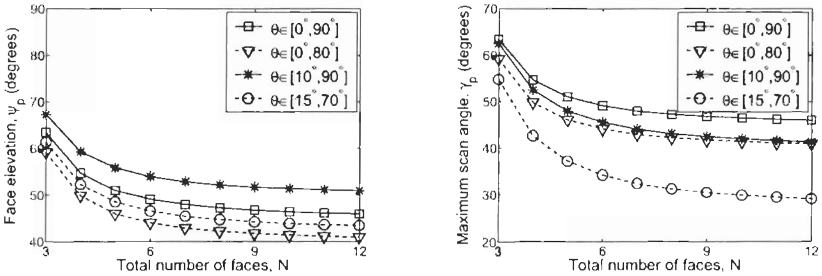

(a) Face elevation, ψ_p, vs. N (b) Maximum scan angle, γ_p vs. N

Figure 2.5: The relationship between (a) the face elevation angle and (b) the maximum scan angle of the pyramidal array and the total number of faces. Four different coverage ranges are considered. ψ_p and γ_p are computed using the equalization-based approach.

It is treated here as follows. For general coverage, ψ_f and γ_f are found by equating the three angles γ_{f_i}, i=1,2,3, given by (2.6) and (2.8). Since all three angles are acute, the cosine function is monotonically decreasing, and hence ψ_f is found by setting $\cos\gamma_{f_1}=\cos\gamma_{f_2}=\cos\gamma_{f_3}$. This results in a system of two non-linear equations in the two unknowns ψ_f and θ_b:

$$\begin{aligned} \cos\tfrac{\pi}{N-1}\sin\psi_f\sin\theta_b+\cos\psi_f\cos\theta_b &= \cos\theta_b, \\ \cos\tfrac{\pi}{N-1}\sin\psi_f\sin\theta_2+\cos\psi_f\cos\theta_2 &= \cos\theta_b. \end{aligned} \tag{2.12}$$

The maximum scan angle, γ_f, thus becomes equal to θ_b, which defines the border between the coverage areas of the top and side faces, as can be seen from (2.6).

A simple closed-form solution of (2.12) is only possible for the case of full coverage, i.e., when $\theta_1 = 0$ and $\theta_2 = \pi/2$, as in [Kmetzo, 1967]. Using substitution, (2.12) reduces to a quadratic equation in θ_b, which can be easily solved. However, attempting to solve the equations for the case of general coverage using substitution, results in a complicated high degree polynomial, to which a simple closed-form solution does not exist. In other words, an analytic solution may exist, but it is so involved that it is neither intuitive nor tractable. This is why the system in (2.12) should be solved numerically or graphically. It is solved here numerically as described in Appendix B.

Figures 2.6(a) and 2.6(b) depict the relationship between ψ_f and γ_f of the pyramidal frustum versus N, respectively, for four different coverage ranges. Similar to Figure 2.5, this figure shows that γ_f decreases as N increases, and that the rate of decrease becomes negligible for N larger than about 10. By comparing Figures 2.5(b) and 2.6(b), one can see that as N increases, pyramidal frusta provide a larger reduction in γ than pyramids.

Note that the minimum zenith angle, θ_1, does not appear explicitly in (2.12). Instead, it appears as a constraint on its solution, $\theta_1 < \theta_b < \theta_2$. Therefore, for a given value of θ_2; ψ_f, θ_b, and γ_f do not change, regardless of θ_1. In other words, for any coverage range of the form $[\theta_1, \theta_2]$, ψ_f, θ_b, and γ_f are the same as those found for the coverage range $[0, \theta_2]$, i.e.,

$$\begin{aligned} \psi_f|_{\theta\in[0,\theta_2]} &= \psi_f|_{\theta\in[\theta_1,\theta_2]}, \\ \theta_b|_{\theta\in[0,\theta_2]} &= \theta_b|_{\theta\in[\theta_1,\theta_2]}, \\ \gamma_f|_{\theta\in[0,\theta_2]} &= \gamma_f|_{\theta\in[\theta_1,\theta_2]}. \end{aligned} \tag{2.13}$$

This is why the curves for the coverage ranges $[0°, 90°]$ and $[10°, 90°]$ in Figure 2.6 are identical.

Given the constraint $\theta_1 < \theta_b < \theta_2$, a feasible ($\psi_f \neq 0$ and $\theta_b \neq \theta_2$) solution of (2.12) may not exist for some coverage ranges. Using (2.13), for the coverage range $[\theta_1, \theta_2]$,

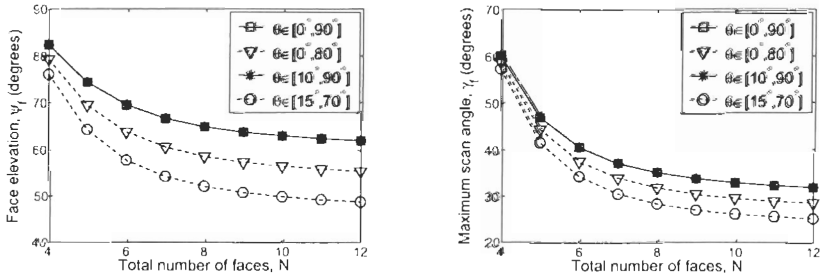

(a) Face elevation, ψ_f, vs. N

(b) Maximum scan angle, γ_f vs. N

Figure 2.6: The relationship between (a) the face elevation angle and (b) the maximum scan angle of pyramidal frusta and the total number of faces. Four different coverage ranges are considered. ψ_f and γ_f are computed using the equalization-based approach.

if θ_1 is chosen such that:

$$\theta_1 > \theta_b|_{\theta\in[0,\theta_2]}, \tag{2.14}$$

then a feasible solution will not exist. For example, when N=4 and θ_2=90°, then θ_b=60.3°. Therefore, a feasible solution of (2.12) cannot be found for coverage ranges $[\theta_1, 90°]$, where $\theta_1 > 60.3°$. The lack of a feasible solution indicates that a pyramidal array should be used instead, since the coverage range lies so far below zenith that the use of the top face becomes unnecessary.

2.3.2 The Minimax-Based Approach

The problem of finding the optimal face elevation which minimizes the maximum scan angle may be expressed as a minimax (or min-max) optimization problem, e.g., [Giorgi et al., 2004]. For the pyramidal antenna array, the problem is defined as:

$$\min_{0\leqslant\psi_p\leqslant\frac{\pi}{2}} \gamma_p = \min_{0\leqslant\psi_p\leqslant\frac{\pi}{2}} \max_{i=1,2} \gamma_{p_i}; \tag{2.15}$$

and for the more complicated case of the pyramidal frustum, the problem is defined as:

$$\min_{\substack{0\leqslant\psi_f\leqslant\theta_2\\ \theta_1\leqslant\theta_b\leqslant\theta_2}} \gamma_f = \min_{\substack{0\leqslant\psi_f\leqslant\theta_2\\ \theta_1\leqslant\theta_b\leqslant\theta_2}} \max_{i=1,2,3} \gamma_{f_i}. \tag{2.16}$$

Minimax optimization problems are typically solved numerically, e.g., [Madsen and Schjær-Jacobsen, 1977].

Note that, unlike the equalization-based approach, a feasible solution of (2.16) always exists for any valid coverage range. In such cases, when the solution of (2.12) is infeasible, the solution of (2.16) has θ_b=θ_1. This indicates that the top face is not needed, i.e., a pyramid rather than a pyramidal frustum should be used. Information about the numerical methods used to solve (2.15) and (2.16) is given in Appendix B.

The values of ψ and γ obtained by solving (2.15) and (2.16) are not always the same as those found using the equalization-based approach (Section 2.3.1). In fact, in many cases, the minimax-based approach results in lower (i.e., better) values of γ, as will be elaborated in Section 2.3.3. In other words, the equalization-based approach does not always give the optimal values of ψ and γ. An example is shown in Figure 2.7.

It plots the individual scan angles, γ_{p_1} and γ_{p_2}, as well as their maximum, γ_p, versus the face elevation of a 3-face pyramidal array. The minimax-based solution is denoted by $\gamma_{p_{\text{mm}}}$ and the equalization-based solution is denoted by $\gamma_{p_{\text{eq}}}$. For full hemispherical coverage, Figure 2.7(a) shows that the two solutions are identical. However, for the coverage range $[0°, 40°]$, the minimax-based solution is lower by over 2°, as shown in Figure 2.7(b).

A similar example can be given for the pyramidal frustum. For a 4-face frustum, a coverage range of $[0°, 90°]$ gives $\gamma_{f_{\text{mm}}}=\gamma_{f_{\text{eq}}}=60.3°$. On the other hand, for the range $[0°, 40°]$, $\gamma_{f_{\text{mm}}}=33.8°$ and $\gamma_{f_{\text{eq}}}=40°$, i.e., the minimax-based approach provides a saving of over 6° in the maximum scan angle. A graphical illustration of this example will not be as simple as that shown in Figure 2.7 for the pyramidal array. This is because the individual scan angles, γ_{f_1}, γ_{f_2}, and γ_{f_3}, as well as their maximum, γ_f, are functions of two variables, ψ_f and θ_b, not just one, as in the case of the pyramid.

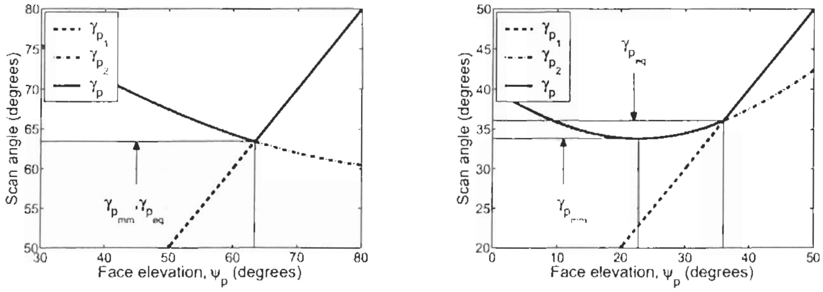

(a) $\theta \in [0°, 90°]$ (b) $\theta \in [0°, 40°]$

Figure 2.7: Two examples illustrating when the the maximum scan angles computed using the equalization-based and minimax-based approaches are the same and when they are different, for a 3-face pyramidal array: (a) $\gamma_{p_{\text{mm}}}=\gamma_{p_{\text{eq}}}$ when the coverage range is $[0°, 90°]$, and (b) $\gamma_{p_{\text{mm}}} < \gamma_{p_{\text{eq}}}$ when the coverage range is $[0°, 40°]$.

2.3.3 Comparison

Figures 2.8 and 2.9 compare the equalization-based and the minimax-based approaches described above, for pyramids and pyramidal frusta, respectively. The results presented in the figures help the antenna system designer decide which approach to use in order to optimize the geometric design of multi-faceted arrays.

The figures plot the difference between the maximum scan angles computed by the two methods, denoted by γ_{eq} and γ_{mm}, respectively. Both pyramidal and pyramidal frustum arrays are considered with different values of N. All valid coverage ranges defined by (2.2), i.e., $\theta_1 < \theta_2$, are examined with increments of $1°$ in both θ_1 and θ_2. The difference is gray-scale coded. So, for example, white areas indicate that γ_{eq}=γ_{mm}, while the darkest shade of gray indicates that γ_{eq}-$\gamma_{\mathrm{mm}} > 10°$. For the pyramidal frustum, the dotted areas in Figure 2.9 indicate the lack of a feasible

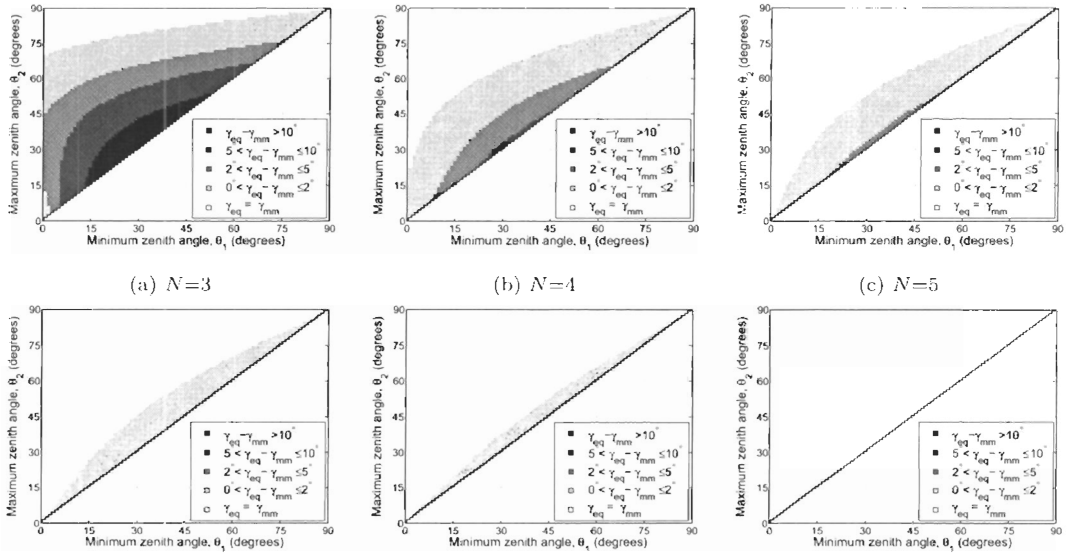

(a) N=3 (b) N=4 (c) N=5

(d) N=6 (e) N=8 (f) $N \rightarrow \infty$

Figure 2.8: The difference between the maximum scan angle obtained using the equalization-based approach, γ_{eq}, and that obtained using the minimax-based approach, γ_{mm}, for pyramidal arrays with different values of N. The darker the shade, the larger the difference between $\gamma_{p_{eq}}$ and $\gamma_{p_{mm}}$. Valid coverage ranges have $\theta_1 < \theta_2$.

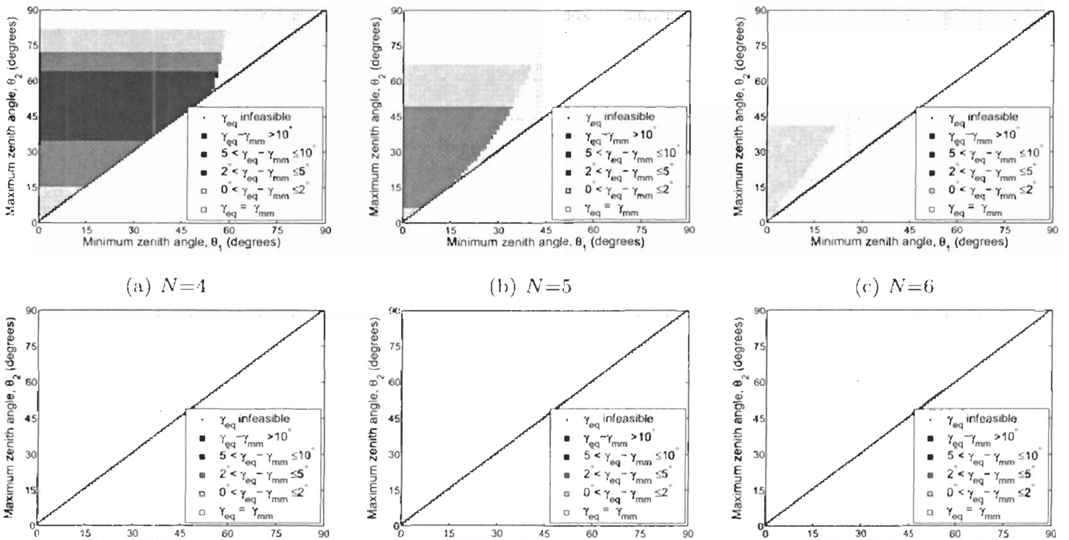

(a) N=4 (b) N=5 (c) N=6

(d) N=7 (e) N=9 (f) $N \to \infty$

Figure 2.9: The difference between the maximum scan angle obtained using the equalization-based approach, γ_{eq}, and that obtained using the minimax-based approach, γ_{mm}, for pyramidal frustum arrays with different values of N. The dotted areas indicate the lack of feasible solutions as described by (2.14).

solution as described by (2.14).

For both classes of multi-faceted arrays, the two methods are equivalent asymptotically, i.e., as $N \to \infty$, as shown in Figures 2.8(f) 2.9(f). For the pyramid, Figure 2.8 shows that the two methods are equivalent at and near full hemispherical coverage (θ_1=0 and $\theta_2 \to \pi/2$) for small N. However, the difference between $\gamma_{p_{\mathrm{eq}}}$ and $\gamma_{p_{\mathrm{mm}}}$ increases as N decreases and as θ_1 approaches θ_2. The small values of N are the most useful, as will be shown in Chapter 5. Therefore, using the minimax-based approach provides a significant improvement over previously reported results.

On the other hand, for the pyramidal frustum, the two methods are equivalent for $\theta_2 \to \pi/2$, of course, only when a feasible solution exists. Moreover, the difference between $\gamma_{f_{\mathrm{eq}}}$ and $\gamma_{f_{\mathrm{mm}}}$ increases as N decreases. This highlights the benefit of using the minimax-based approach, similar to the pyramid case. Finally, the portion of coverage ranges where feasible solutions do not exist increases as N increases, as shown in Figure 2.9, which demonstrates the indispensability of the minimax-based approach for such coverage ranges. The minimax-based approach is used throughout the rest of the thesis to compute the maximum scan and face elevation angles for both pyramids and pyramidal frusta.

2.4 Impact of Far-Field Approximation

When the optimal face elevation and the corresponding maximum scan angle were derived in Section 2.3, it was assumed that the distance from the target to the antenna is sufficiently large and so the antenna dimensions were neglected. However, for quasi far-field pattern measurement, finite distances and antenna dimensions need to be considered. Pattern measurements for scanning antenna arrays are expensive, since many beam directions (perhaps several thousands) need to be checked for gain, as well as other parameters, such as directional polarization purity. This section examines how considering finite dimensions affects the results presented in Section 2.3 [Khalifa and Vaughan, in press].

Figure 2.10 illustrates how the distance from the target to the array affects the maximum scan angles of the pyramid and pyramidal frustum; γ_p and γ_f, respectively. In the figure, the face elevation angles, ψ_p and ψ_f are computed using the minimax-based approach assuming infinite distance, and the thick horizontal lines show the corresponding values of γ_p and γ_f. It is assumed that each face supports a circular array of diameter D, and four different values of D are considered. Then, γ_p and γ_f are computed at different distances, d, to the array, where d is measured from the target to the origin. A full hemispherical coverage requirement is assumed. The computation details can be found in Appendix C.

The figure illustrates how both γ_p and γ_f approach the asymptotic values (thick lines) as d or D increase, and as N decreases (To facilitate visual comparison, the y-axis in all of the sub-figures spans 10°). As a matter of fact, the difference is within 2° for distances larger than $10D^2/\lambda$, which is the minimum far-field distance used for measuring extremely low sidelobe patterns [Mailloux, 1994]. For example, at a

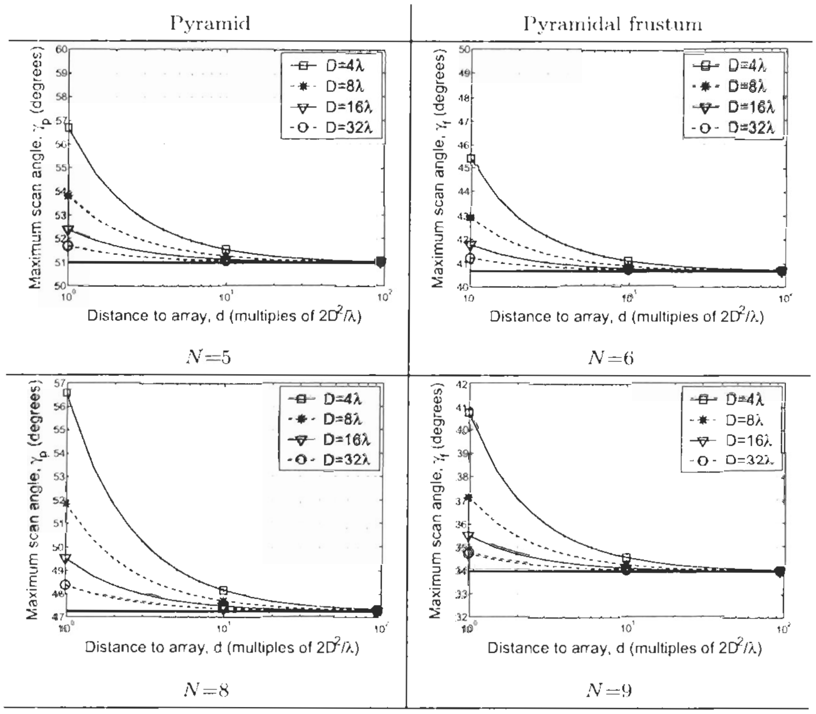

Figure 2.10: The relationship between the maximum scan angles of pyramidal (left) and pyramidal frustum (right) arrays, and the distance from the target to the antenna, d, at different values of the array diameter, D, and the total number of array faces, N. Full hemispherical coverage is assumed.

frequency of 1.54 GHz, and using D=8λ, $10D^2/\lambda$ amounts to a distance of about 125 meters to the antenna.

2.5 Lower Bounds on the Maximum Scan Angles

Section 2.3 presented methods to compute the exact optimal maximum scan angles for pyramids and pyramidal frusta with a given number of faces, N. However, it is also useful to examine the lower bounds on the maximum scan angles, $\gamma_{\min}$, obtained as $N \to \infty$, for a given coverage range $\theta \in [\theta_1, \theta_2]$. Such information helps the antenna designer to determine the maximum reduction in maximum scan that can be achieved by a given antenna array structure, i.e., planar, pyramidal, or pyramidal frustum.

For a planar array, the maximum scan angle is always equal to θ_2, and hence the lower bound is:

$$\gamma_{l_{\min}} = \theta_2. \tag{2.17}$$

For the pyramidal array, the minimax-based and equalization-based approaches are equivalent for large N. Therefore, $\gamma_{p_{\min}}$ occurs when $\gamma_{p1} = \gamma_{p2}$. Also, as $N \to \infty$, the azimuthal scan requirement becomes infinitesimal ($2\pi/N \to 0$) and γ_p becomes dominated by the elevation scan requirement only. Therefore, as shown in Figure 2.11(a), $\gamma_{p_1} + \gamma_{p_2} = \theta_2 - \theta_1$, and the lower bound is given by:

$$\gamma_{p_{\min}} = (\theta_2 - \theta_1)/2. \tag{2.18}$$

Similarly, the lower bound for the pyramidal frustum can be derived using the equalization-based approach, as shown in Figure 2.11(b), where $\gamma_{f_1}+\gamma_{f_2}+\gamma_{f_3}=\theta_2$. However, the equalization-based approach fails to find a feasible solution under the condition in (2.14). But since that condition indicates that a pyramid, rather than a pyramidal frustum should be used (Section 2.3.2), then the lower bound is given by:

$$\gamma_{f_{\min}} = \begin{cases} \theta_2/3 & \text{if } \theta_1 \leqslant \theta_b|_{\theta\in[0,\theta_2]}, \\ (\theta_2 - \theta_1)/2 & \text{otherwise.} \end{cases} \tag{2.19}$$

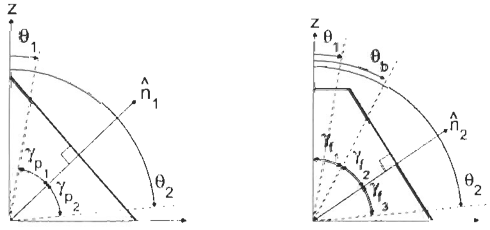

(a) Pyramid (b) Pyramidal frustum

Figure 2.11: Illustration of how the lower bounds on the maximum scan angles are determined for the (a) pyramidal and (b) pyramidal frustum antenna arrays. As $N \to \infty$, the azimuthal scan requirement becomes infinitesimally small and the maximum scan angle becomes dominated by the elevation scan requirement only.

Equations (2.18) and (2.19) show that the lower bounds on γ achieved using the pyramid and the pyramidal frustum are 45° and 30°, respectively, given a full hemispherical coverage requirement, in agreement with [Kmetzo, 1967]. Moreover, they show that using multi-faceted arrays reduces the maximum scan angles for any coverage range. For very limited coverage ranges (θ_2 close to zenith), however, it may be sufficient to use a single planar array. This is because the increase in γ, and the associated scan loss and mutual coupling increase, are offsetted by the lower antenna complexity. A more elaborate discussion on choosing the array structure (planar, pyramidal, or pyramidal frustum) and the number of faces, N, is presented in Section 2.6 and Chapter 5.

In order to reduce the maximum scan angle beyond the bounds given above, antenna arrays made of other, more complex polyhedra can be used. One alternative is the stacked pyramids shown in Figure 2.12, which is similar to that used in [Padros et al., 1997]. The faces of the polyhedron cover non-overlapping sectors of the hemispherical volume, and γ is reduced by dividing the elevation scan requirement among two side faces, instead of one. This idea is similar to dividing the azimuthal scan range among the side faces of a pyramid or a pyramidal frustum. It can be shown that the lower bound on γ achieved using this structure is 22.5° for full hemispherical coverage (using a similar argument to that in Figure 2.11(a)). This further reduction in γ, however, comes at the expense of more complex analysis and implementation.

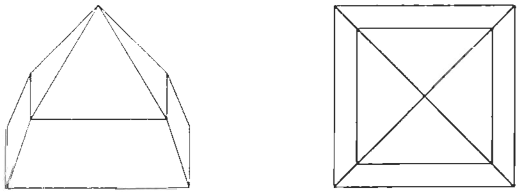

Figure 2.12: An example of a multi-faceted array configuration that provides a further reduction in the maximum scan angle: oblique view (left) and plan view (right).

2.6 The Effect of the Number of Faces on the Maximum Scan Angle

The results displayed in Figures 2.5(b) and 2.6(b) suggested that increasing the number of faces of pyramids beyond 7, or pyramidal frusta beyond 10, brings only diminished returns to reducing the maximum scan angle. These figures, however, only considered very few coverage ranges. The effect of the total number of faces, N, on reducing the maximum scan angle is investigated more thoroughly here.

Figure 2.13 depicts the maximum scan angle, γ_p, achieved using N-face pyramids, where $N = 3, 4, \ldots, 10$, for all valid coverage ranges. The figure on the bottom right corner shows the lower bound, $\gamma_{p_{\min}}$, which is achieved as $N \rightarrow \infty$ and computed using (2.18). The value of γ_p is gray-scale coded, where the seven shades of gray correspond to consecutive 10°-ranges of γ_p. The figure shows how γ_p decreases as N increases for a given coverage range, and how γ_p increases as the coverage range gets wider for a given value of N. It also shows how γ_p decreases quickly for values of N less than about 8, and how it slowly approaches $\gamma_{p_{\min}}$ by increasing N further. For N=7, the difference between γ_p and $\gamma_{p_{\min}}$ is around 10°.

Figure 2.14 shows similar results for N-face pyramidal frusta, where $N = 4, 5, \ldots, 11$. The lower bound, $\gamma_{f_{\min}}$, is shown on the bottom right corner of the figure, and is computed using (2.19). Pyramidal frusta exhibit similar trends to pyramids, in terms of how γ_f approaches $\gamma_{f_{\min}}$ as the total number of faces is increased. The figure shows that the γ_f is within around 10° from $\gamma_{f_{\min}}$ for N=9 or 10.

The conclusion to be drawn from these results is that no significant reduction in the maximum scan angle is achieved by increasing the number of faces of pyramids beyond 7, or pyramidal frusta beyond 10, unless only very low scan losses can be tolerated. Large values of N may still be used, for example, to achieve conformity, such as the approximation of a cone by a 24-face pyramid used in [Caille et al., 2002] (Section 1.1.2). The topic of conformal arrays, however, is out of the scope of this work. Moreover, as will be elaborated in Section 5.2.1, given a constant antenna footprint, increasing N results in smaller array apertures and hence less gain. Alternatively, for a given array aperture size, increasing N results in increasing the antenna footprint,

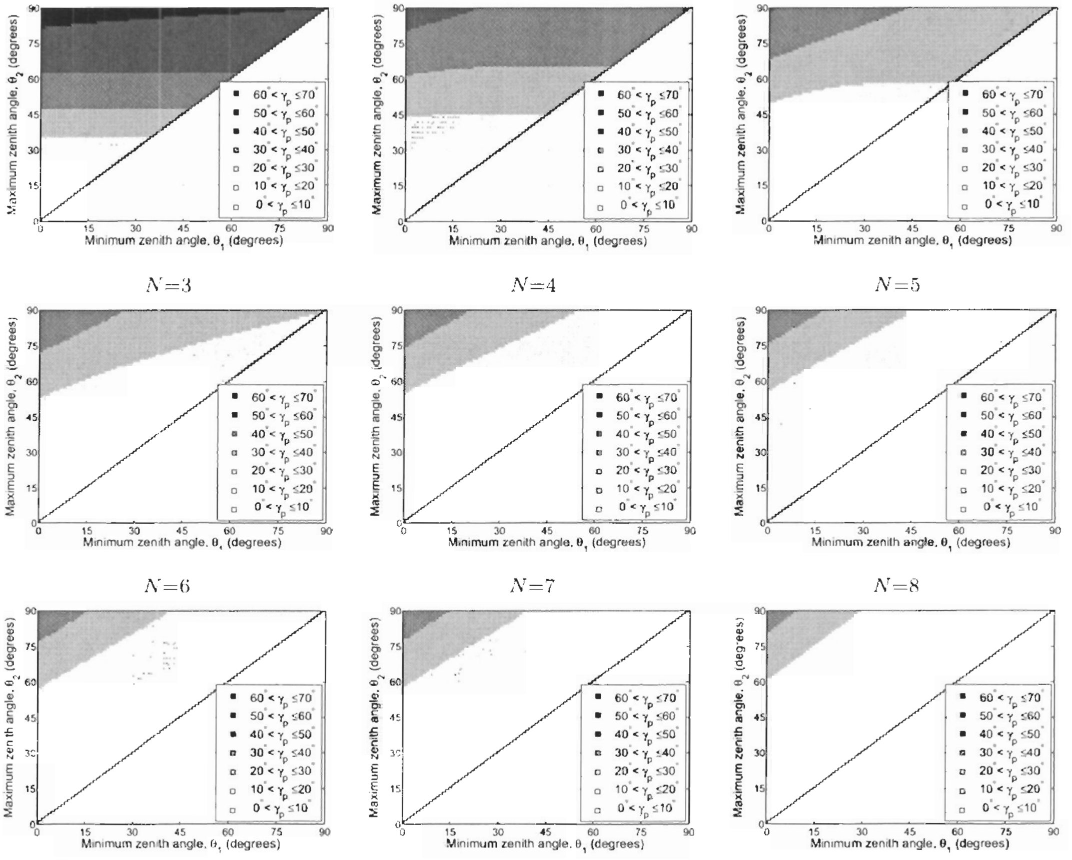

N=3 N=4 N=5

N=6 N=7 N=8

N=9 N=10 $N \to \infty$

Figure 2.13: The maximum scan angle, γ_p, for N-face pyramidal arrays for all valid coverage ranges ($\theta_1 < \theta_2$). The darker the shade, the larger the value of γ_p.

which is typically directly related to the antenna cost. Therefore, only values of N up to 12 will be considered here.

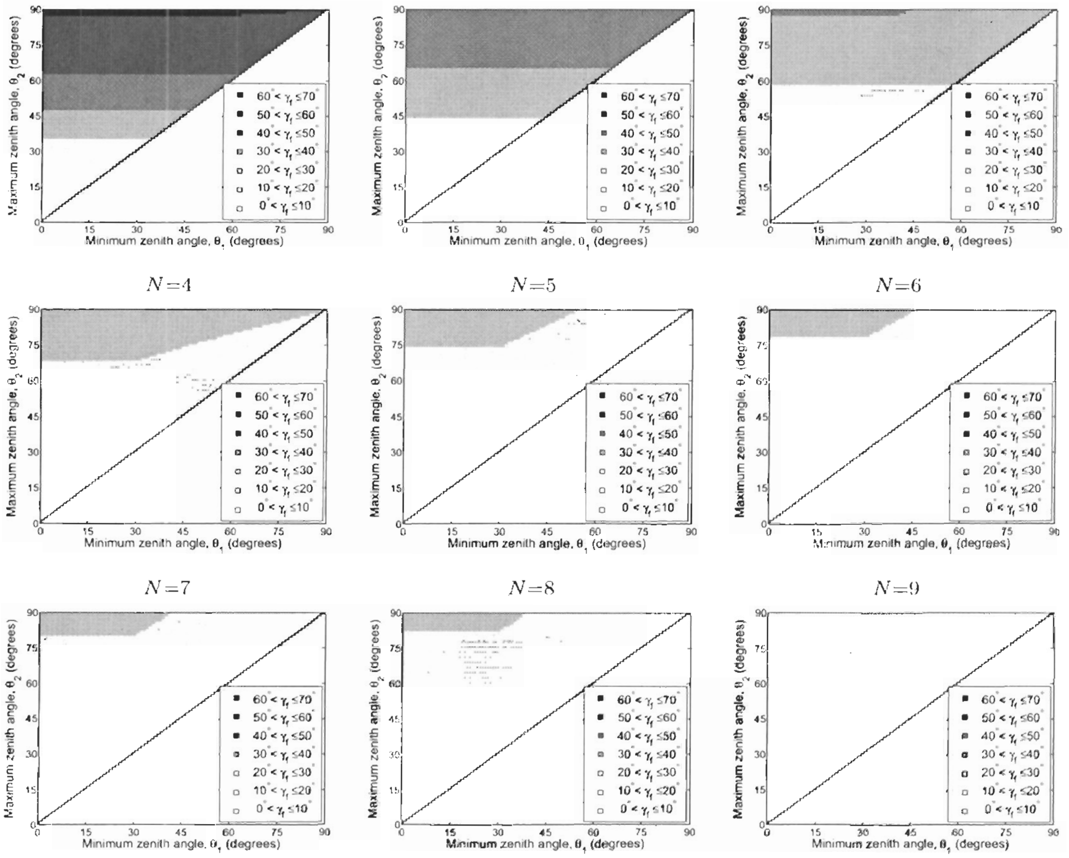

N=4 N=5 N=6

N=7 N=8 N=9

N=10 N=11 $N \to \infty$

Figure 2.14: The maximum scan angle, γ_f, for N-face pyramidal frustum arrays for all valid coverage ranges ($\theta_1 < \theta_2$). The darker the shade, the larger the value of γ_f.

2.7 Summary

This chapter addressed the problem of optimizing the geometric design of pyramidal and pyramidal frustum antenna arrays. The optimization process involved choosing the face elevation which minimizes the overall maximum scan angle, given a general hemispherical scan coverage requirement. The following contributions were presented:

- A simple and direct equalization-based approach to determine the face elevation of pyramidal arrays.

- A new equalization-based method to compute the face elevation of pyramidal frusta.
- A new minimax-based approach to compute the optimal face elevation of both pyramids and pyramidal frusta.

All methods are applicable for the general hemispherical scan coverage requirement. The analysis showed that the equalization-based approach is not always optimal, and a comparison of the two approaches demonstrated the significant design improvement offered by the minimax-based approach.

Moreover, the impact of the far-field approximation has been investigated by considering finite distances to the antenna and finite antenna dimensions. The results show that the maximum scan angle increases only slightly at distances equal to or larger than the far-field approximation, $10D^2/\lambda$, typically used for low-sidelobe far-field pattern measurement. Finally, lower bounds on the maximum scan angles achieved by pyramids and pyramidal frusta were derived, and the effect of increasing the total number of faces on the maximum scan angle was investigated. The results indicated that increasing the number of faces of pyramids beyond 7, or pyramidal frusta beyond 10, brings only diminished returns to reducing the maximum scan angle. A detailed discussion on choosing the number of faces, N, using different figures of merit will be given in Chapter 5.

Chapter 3

The Circular Patch Antenna Element

This chapter focuses on the circularly polarized circular patch antenna, which is chosen here as the antenna element. In particular, it investigates the circular polarization purity of the antenna over angular sectors about the broadside direction. These angular sectors correspond to the coverage areas of the arrays in a multi-faceted antenna. First, the motivation for using the circular patch antenna and studying its polarization purity is outlined, along with an overview of previous work. The antenna structure is then described and expressions for the far-field patterns are derived. An overview of polarization representation and polarization purity is presented, followed by numerical results and their interpretation. Finally, the effects of amplitude, phase shift, and feed position tolerances on polarization purity are outlined.

3.1 Introduction and Previous Work

Circular patch antennas are widely used in many applications owing to their compactness and ease of manufacturing and integration with other circuit elements [Vaughan and Andersen, 2003]. Their applications include satellite, vehicular (aircraft, cars, busses, trains), personal (cellphones, PDAs), and mobile communications. Patch antennas in general are low-gain elements [Hansen, 1998]. Antenna arrays typically employ low-gain elements, especially when scanning is required, in order to minimize the reduction in gain when the array main beam is scanned away from broadside. Moreover, circular patches are slightly smaller than their square or rectangular counterparts [Waterhouse, 2003].

Circular polarization (CP) is typically used in satellite communications, including navigation systems, since its polarization efficiency is not affected by Faraday rotation in the ionosphere, unlike linear polarization (LP). For CP antennas used for multiple satellite communications, the polarization purity is particularly important, both in the direction of maximum gain and also in the off-axis directions. CP can also be used to mitigate line-of-sight multipath fading in mobile communication systems because the multipath tends to be de-polarized, e.g., [Kajiwara, 2000], [Yang and Rahmat-Samii, 2002]. Scanning arrays with CP can use sequential element rotation [Hall et al., 1989], for example, to improve the polarization purity. Nevertheless, whether a single antenna or an antenna array is used, the co-polar gain and the polarization efficiency still depend on the cross-polar patterns of the antenna elements. These factors motivate an investigation of the upper bounds on the polarization purity of the circular patch antennas. Incorporating factors such as most finite groundplane effects or mutual coupling, will normally affect the polarization purity, in particular in the directions along the groundplane. However, in multi-faceted antennas, the directions of interest are away from the groundplane, i.e. within at most 63° about broadside as can be seen in Figures 2.5(b) and 2.6(b).

The polarization purity of an LP or CP antenna may be described by the cross polarization ratio (CPR), defined as the ratio of cross-polarization to co-polarization. Hansen [Hansen, 1987] investigated the CPR of circular and square patches, using the cavity model, but only for the LP case.

The CP far-field patterns and their components are azimuthally symmetric, as will be shown in Section 3.3, unlike the LP patterns illustrated in [Vaughan, 1988]. Correspondingly, their CPR behavior is quite different from the LP case. CP circular patch designs continue to be of interest and several have been proposed, e.g., [Huang, 1984], [Wong and Chiou, 2001], [Boccia et al., 2003], and [Basilio et al., 2005]. For these designs, only pattern cuts of the co- and cross-polar patterns were presented, with an interest in the polarization purity. However, there has been no formal investigation of the effect of the patch size on the CPR of CP patches, as was done in [Hansen, 1987] for the LP case.

An investigation of the CPR of broadside mode CP circular patch antennas was presented in [Khalifa and Vaughan, 2006a]. This treatment is elaborated in this chapter and expanded to higher mode patch antennas. The single mode ring source, with excitation $e^{jn\phi}$, is used for the far-field pattern and the corresponding single mode cavity model is used to define the patch size. The patterns are discussed with interchanging reference to the ring source and the corresponding (single mode) patch parameters. The maximum CPR (used in [Hansen, 1987] for LP) and distributed CPR (introduced here) are computed over different angular intervals about broadside. These intervals represent, for example, the scan sectors of antenna arrays, or the directions of distributed sources such as those found in mobile communications. New results are presented to illustrate the CPR trends. The results show that for the broadside mode, a nominal patch radius of about $\lambda_0/4$ exhibits the best polarization purity. From the cavity model, this corresponds to specific, low values of the substrate relative permittivity. The models are also used to study the effect of amplitude, phase shift, and feed position tolerances that may occur in implemented antennas.

3.2 Antenna Structure

The circular patch antenna is composed of a thin metallic disc mounted above a grounded dielectric substrate. The substrate can be air, which means that the patch must be supported by, for example, dielectric posts. The patch may be fed by microstrip transmission lines along the patch layer of the substrate, or by coaxial lines from the groundplane. There can be multiple feed positions to implement antenna diversity, or for a beamformer to produce specific patterns such as the circular polarizations. Figure 3.1 illustrates an example of a circular patch fed by coaxial lines from the finite groundplane. In this work, we do not consider the physical size of the patch, but rather its effective size, which includes the field fringing at the edge of the patch. Usually, in the literature, the effective size is denoted by the radius a_{eff}. Here

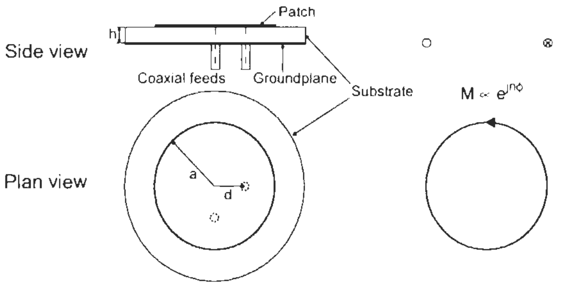

Figure 3.1: Structure of a finite groundplane CP circular patch antenna (left) and the equivalent magnetic ring source with magnetic current M (right).

we abbreviate this to a, so from now on, all mention of the patch radius is taken to be the effective radius, and this is used for the ring source size. The patch radius, a, is approximated as [Derneryd, 1979]:

$$a \approx \frac{\alpha_{n1}}{k_0\sqrt{\epsilon_r}}, \tag{3.1}$$

where α_{n1} is determined by setting $J'_n(\alpha_{n1})=0$, where J'_n is the first derivative of Bessel function of the first kind and order n. Therefore, α_{n1} is set to 3.8317, 1.8412, 3.0542, and 4.2012 for n=0, 1, 2, and 3, respectively. $k_0=\frac{2\pi}{\lambda_0}$ is the wave number in free space and ϵ_r is the relative permittivity of the substrate material. The relationship between the patch radius and the permittivity is illustrated in Figure 3.2 for modes 0, 1, 2, and 3.

A single feed is sufficient to construct a LP circular patch. On the other hand, a CP circular patch antenna can be constructed by using two angularly spaced feeds at the azimuthal positions $\phi_0 = 0°$ and $\phi_0 = \frac{90°}{n}$, where the mode $n \neq 0$ and ϕ_0 is the azimuthal feed position [Huang, 1984]. (CP may not be realized with good polarization purity using the n=0 mode, which is linearly polarized everywhere). The example in Figure 3.1 could be for the n=1 mode. The feeds are excited with a 90° phase shift for right-hand circular polarization (RHCP), or −90° for left-hand circular polarization (LHCP).

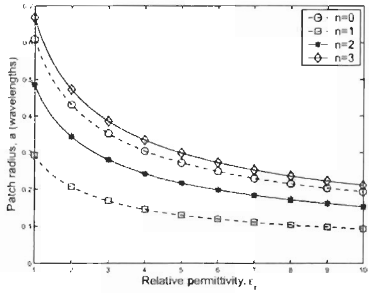

Figure 3.2: The approximate (cavity model) relation between the patch radius and the relative substrate permittivity for the circular patch.

3.3 Far-Field Radiation Pattern

The single mode cavity model treats the patch antenna as a cylindrical cavity with a magnetic wall along its perimeter, which can be resonant in the transverse magnetic (TM) modes [Derneryd, 1979]. Using a single feed at ϕ_0 to excite a single mode, the far-field radiation pattern of the nth cosine mode, to be used below, is well-known, e.g., [Martin, 1960; Derneryd, 1979; James et al., 1981], and is given by:

$$\mathbf{E}^{[n]}(\theta,\phi) = E_\theta^{[n]}(\theta,\phi)\hat{\theta} + E_\phi^{[n]}(\theta,\phi)\hat{\phi}, \tag{3.2}$$

where the linearly polarized components are:

$$\begin{aligned} E_\theta^{[n]}(\theta,\phi) &= j^n V_0^{[n]} \tfrac{k_0 a}{2}\; J_n^- \cos\left[n(\phi-\phi_0)\right], \\ E_\phi^{[n]}(\theta,\phi) &= -j^n V_0^{[n]} \tfrac{k_0 a}{2}\; J_n^+ \cos\theta \sin\left[n(\phi-\phi_0)\right], \end{aligned} \tag{3.3}$$

where $\hat{\theta}$ and $\hat{\varphi}$ are unit vectors along the θ and ϕ directions, $V_0^{[n]}{=}hE_0J_n(ka)$ is the peak voltage at the edge of the patch, a is the patch radius, and $k{=}\frac{k_0}{\sqrt{\epsilon_r}}$. J_n is the Bessel function of the first kind and order n, and $J_n^-{=}(J_{n+1}-J_{n-1})$ and $J_n^+{=}(J_{n+1}+J_{n-1})$, where $J_n{=}J_n(ka\sin\theta)$. A time dependence of $e^{j\omega t}$ is assumed for the fields. Equation (3.3) shows that only the $n{=}1$ mode pattern is non-zero at broadside, as illustrated in [Vaughan, 1988]. Other modes have their peak gains at mid-elevation angles, depending on n and a, as will be elaborated below.

For a CP circular patch, the two feeds (at $\phi_0 = 0^\circ$ and $\phi_0 = \frac{90^\circ}{n}$) lie in the null cavity field of each other. This can be seen from (3.3), e.g., the ϕ dependence of $E_\theta(\theta, \phi)$ due to the two feeds is of the form $\cos n\phi$ and $\cos\left[n(\phi - \frac{90^\circ}{n})\right] = \sin n\phi$, respectively. This produces two identical modes which are orthogonal in the cavity. With negligible mutual coupling between these degenerate modes, the cavity model can be simply extended to represent the far-field pattern due to the two feeds as follows:

$$\mathbf{f}^{[n]}(\theta, \phi) = f_\theta^{[n]}(\theta, \phi)\hat{\theta} + f_\phi^{[n]}(\theta, \phi)\hat{\phi}, \tag{3.4}$$

where the θ- and ϕ-components are:

$$\begin{aligned} f_\theta^{[n]}(\theta, \phi) &= E_\theta^{[n]}(\theta, \phi)\big|_{\phi_0=0^\circ} \mp jE_\theta^{[n]}(\theta, \phi)\big|_{\phi_0=\frac{90^\circ}{n}} &&= j^n V_0^{[n]} \tfrac{k_0 a}{2}\ J_n^- e^{\mp jn\phi}; \\ f_\phi^{[n]}(\theta, \phi) &= E_\phi^{[n]}(\theta, \phi)\big|_{\phi_0=0^\circ} \mp jE_\phi^{[n]}(\theta, \phi)\big|_{\phi_0=\frac{90^\circ}{n}} &&= \mp j^{(n+1)} V_0^{[n]} \tfrac{k_0 a}{2}\ J_n^+ \cos\theta e^{\mp jn\phi}; \end{aligned} \tag{3.5}$$

where the upper and lower signs represent RHCP and LHCP, respectively, and $E_\theta^{[n]}$ and $E_\phi^{[n]}$ are given in (3.3).

To this point, the equations are known, for example equation (3.5) is similar to the pattern expressions given in [Huang, 1984], but the form given here is more compact and more revealing. It shows that the CP pattern magnitudes are symmetric with respect to ϕ, unlike the $\cos n\phi$ modes. For example, Figure 3.3 shows linear plots of the linearly polarized pattern magnitudes for CP patches with modes ±1, ±2, and ±3, assuming air (ϵ_r=1) and alumina (ϵ_r=10) substrates. (Refer to Section A.2 for information about the graphical representation of radiation patterns). The pattern magnitudes are only plotted above the xy-plane. However, they are symmetric about that plane. They are also identical for $+n$ and $-n$. The vertically polarized patterns for ϵ_r=10 exhibit strong gain along the (infinite) groundplane direction. The elevation-cut patterns do not change much for a ϵ_r above 2, and do not change much for the higher modes. So, Figure 3.3 is representative of all practical permittivities in the basic cavity model.

Equations (3.4) and (3.5) may be rewritten to represent the far-field patterns radiated by RHCP and LHCP antennas, respectively, in terms of the LP patterns, as

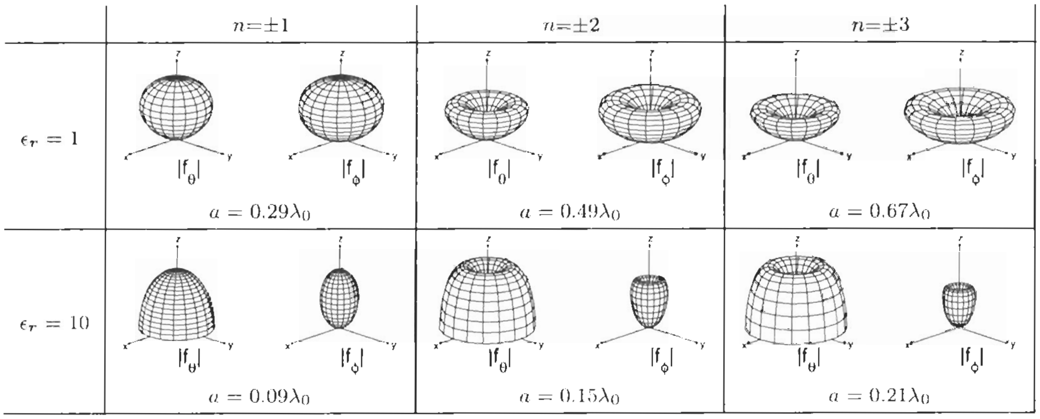

Figure 3.3: Linear plots of the magnitudes of the θ- and ϕ-components of the far-field patterns of CP circular patches for modes ±1, ±2, and ±3, using ϵ_r=1 and ϵ_r=10. The corresponding patch radius, a, is listed for each configuration.

follows:

$$\begin{aligned}
\mathbf{f}_R^{[n]}(\theta,\phi) &= f_{R_\theta}^{[n]}(\theta,\phi)\hat{\theta} + f_{R_\phi}^{[n]}(\theta,\phi)\hat{\phi} &= j^n V_0^{[n]} \tfrac{k_0 a}{2} e^{-jn\phi}\Big(J_n^- \hat{\theta} - jJ_n^+ \cos\theta\hat{\phi}\Big); \\
\mathbf{f}_L^{[n]}(\theta,\phi) &= f_{L_\theta}^{[n]}(\theta,\phi)\hat{\theta} + f_{L_\phi}^{[n]}(\theta,\phi)\hat{\phi} &= j^n V_0^{[n]} \tfrac{k_0 a}{2} e^{jn\phi}\Big(J_n^+ \hat{\theta} + jJ_n^- \cos\theta\hat{\phi}\Big).
\end{aligned} \tag{3.6}$$

The magnitudes of $\mathbf{f}_R^{[n]}$ and $\mathbf{f}_L^{[n]}$ are the same. They are used in Section 3.4 to express the co- and cross-polar patterns.

3.3.1 Assumptions and Limitations

The ring source model for the circular patch antenna, in (3.3), assumes an infinite groundplane. In practice, a finite groundplane can affect the impedance and the pattern–specifically at low-elevation angles. Similarly, any surface waves on a continuous substrate may also affect the pattern. Finite groundplanes may improve the polarization purity at low-elevation angles. However, in these cases, the groundplane structure, including its edges, comprises a necessary part of the antenna and the single magnetic ring source that is used here models only part of such a radiating structure. The impact of a small groundplane is demonstrated in Section 3.5.

The height of the patch above the groundplane, h, influences the patch bandwidth, but has a minor effect on the center frequency. h does not affect the radiation pattern significantly [Kishk and Shafai, 1986]. It is assumed to be electrically small, and does not enter the radiation pattern formulation here. However, it is noted that h does feature in some pattern formulations, for example, [Hansen, 1987]. For single modes, the distance of the coaxial feed from the patch center, d, affects only its impedance. For example, for the n=1 mode, $d \approx 0.3a$ typically gives a good match to a 50Ω feed impedance.

Finally, it is assumed in (3.5) that the mutual coupling between the two feeds is zero. In practice, the finite extent of the feed structures, and the presence of other modes, albeit at relatively low powers, act to create finite coupling.

It is emphasized that the radiation of a pure mode ring source yields the upper bounds on the polarization purity of the circular patch antenna on a large groundplane. Unwanted modes and mutual coupling when used in arrays, etc., will act to decrease the polarization purity from the bounds given in Section 3.5. Polarization purity bounds are of interest because they can be used to set limits on the performance of a fixed antenna or a scanning array. As noted above, this is particularly relevant to satellite applications.

3.4 Cross Polarization Ratio

3.4.1 Co- and Cross-Polar Patterns

The polarization of an antenna is that of the plane wave transmitted by that antenna. The sense of polarization of CP has been a source of ongoing confusion between the antenna and the propagation communities, so the definitions used here are briefly reviewed in order to avoid ambiguity. According to the IEEE standard [IEEE, 1979], and assuming a time dependence of $e^{j\omega t}$, the sense of CP is determined by viewing the polarization plane, which contains the transverse electric field vector, with the wave direction moving away the observer. At a fixed point in space, if the tip of the vector rotates clockwise as a function of time, the wave is right-hand (RH) polarized. For counter clockwise rotation, it is left-hand (LH) polarized. If the time dependence is taken as $e^{-j\omega t}$, then the RHCP and LHCP are reversed.

Using the complex vector representation [Stutzman, 1993], and assuming RHCP is the co-polarization, the complex unit vectors associated with the two orthogonal CP polarization states, i.e., co-polarization (RHCP) and cross-polarization (LHCP), are:

$$\begin{aligned} \hat{e}_{co} &= \tfrac{1}{\sqrt{2}}\Big((\sin\phi + j\cos\phi)\hat{\theta} + (\cos\phi - j\sin\phi)\hat{\phi}\Big) &= \tfrac{1}{\sqrt{2}}\, e^{-j\phi}(\hat{\theta} - j\hat{\phi}), \\ \hat{e}_{cr} &= \tfrac{1}{\sqrt{2}}\Big((\sin\phi - j\cos\phi)\hat{\theta} + (\cos\phi + j\sin\phi)\hat{\phi}\Big) &= \tfrac{1}{\sqrt{2}}\, e^{j\phi}(\hat{\theta} + j\hat{\phi}). \end{aligned} \tag{3.7}$$

If LHCP is the co-polarization, then these vectors are interchanged. Using (3.7), the far-field pattern vector radiated by a RHCP antenna at the nth mode, $\mathbf{f}_R^{[n]}(\theta,\phi)$, can be decomposed into its CP co- and cross-polar patterns using:

$$\begin{aligned} F_{co}^{[n]}(\theta,\phi) &= \mathbf{f}_R^{[n]}(\theta,\phi)\ .\ \hat{e}_{co} \\ &= j^n V_0^{[n]} \tfrac{k_0 a}{2\sqrt{2}} e^{-j(n+1)\phi}\Big((1-\cos\theta)J_{n+1} - (1+\cos\theta)J_{n-1}\Big), \\ F_{cr}^{[n]}(\theta,\phi) &= \mathbf{f}_R^{[n]}(\theta,\phi)\ .\ \hat{e}_{cr} \\ &= j^n V_0^{[n]} \tfrac{k_0 a}{2\sqrt{2}} e^{-j(n-1)\phi}\Big((1+\cos\theta)J_{n+1} - (1-\cos\theta)J_{n-1}\Big), \end{aligned} \tag{3.8}$$

where $\mathbf{f}_R^{[n]}(\theta,\phi)$ is given in (3.6). Equation (3.8) shows that the phases of the co- and cross-polar patterns have different azimuthal dependence. In fact, the difference is $e^{j2\phi}$, independent of the mode. However, their magnitudes, $|F_{co}^{[n]}|$ and $|F_{cr}^{[n]}|$, are azimuthally symmetric. Equation (3.8) also shows that for the n=1 mode, the co-polar pattern reaches its maximum value at broadside ($\theta = 0°$), while the cross-polar pattern vanishes. As expected, for higher modes, both $|F_{co}^{[n]}|$ and $|F_{cr}^{[n]}|$ vanish at broadside. For higher modes, the zenith angle where $|F_{co}^{[n]}|$ peaks depends on the mode and the substrate relative permittivity [Huang, 1984]. Figure 3.4 illustrates the relationship between the zenith angle where $|F_{co}^{[n]}|$ peaks, and ϵ_r for modes 2 and 3. Peak directions move away from broadside as ϵ_r or n are increased. For a given mode, the peak directions do not change significantly for values of ϵ_r larger than about 3.

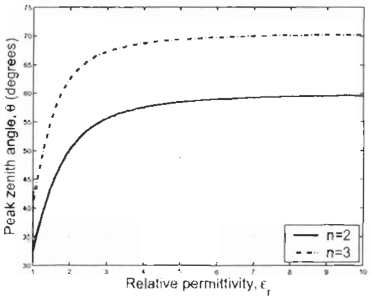

Figure 3.4: The relationship between the directions (zenith angles) where the co-polarization, $|F_{co}^{[n]}|$, peaks and the substrate relative permittivity for modes 2 and 3. For the n=1 mode, $|F_{co}^{[n]}|$, always peaks at $\theta = 0°$.

Figure 3.5 shows polar plots of $|F_{co}^{[n]}|$ and $|F_{cr}^{[n]}|$ of CP circular patches of different radii, cut at ϕ=0°, i.e., $|F_{co}^{[n]}(\theta, 0)|$ and $|F_{cr}^{[n]}(\theta, 0)|$, for n=1, 2, and 3. The major changes to the pattern occur near a relative permittivity of 1. For $\epsilon_r \geqslant 2$, the elevation-cut patterns change very little for each mode, so again, the figure is representative of all practical permittivities in the basic cavity model. Some measured pattern cuts were reported in [Huang, 1984], where higher order patches with a large groundplane (3 wavelengths square) show good agreement with the ring source models, for both polarizations and for low-elevation angles.

3.4.2 Maximum and Distributed CPR

The CPR, $R(\theta, \phi)$, is defined for a dB scale as:

$$R_{\mathrm{dB}}^{[n]}(\theta, \phi) = 20 \log_{10} R^{[n]}(\theta, \phi) = 20 \log_{10} \frac{|F_{cr}^{[n]}(\theta, \phi)|}{|F_{co}^{[n]}(\theta, \phi)|}. \tag{3.9}$$

Using a dB scale circumvents confusion, since CPR is variously used in the literature as either the ratio of powers or amplitudes. The definition of R remains unchanged regardless of the choice of the intended polarization, unlike the circular polarization ratio, ρ_C. ρ_C is defined as the amplitude of the RHCP over that of the LHCP, following a tradition from the precursor [Hollis et al., 1970] to the IEEE standard [IEEE, 1979].

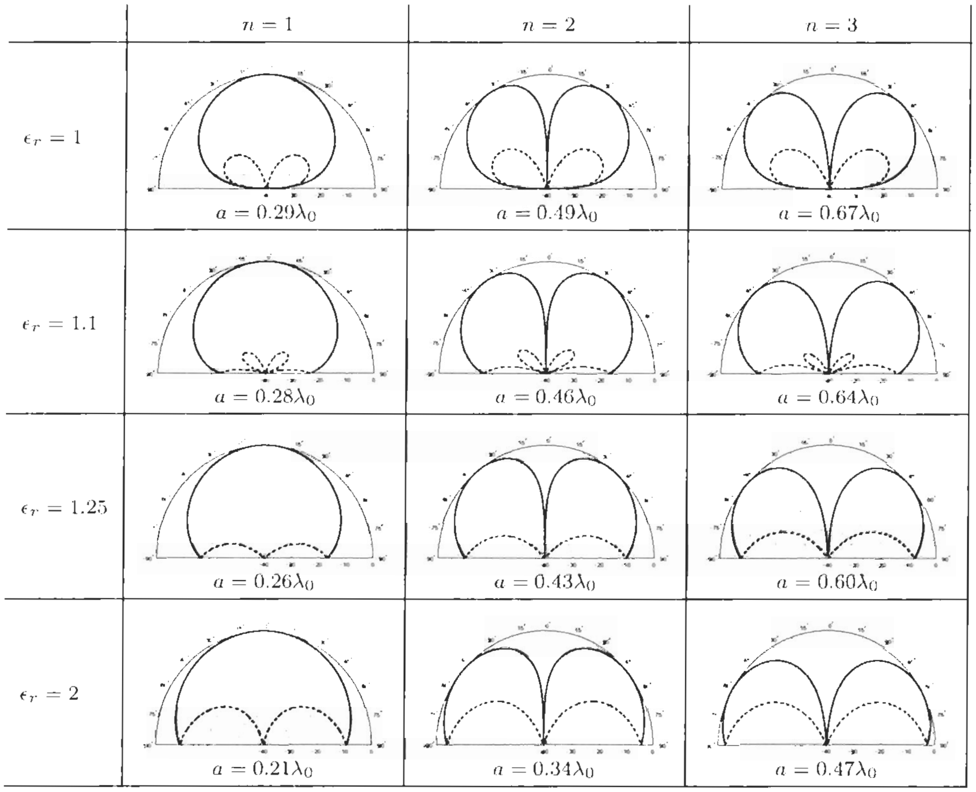

Figure 3.5: Cuts of the dB-scale magnitudes of the co-polar (solid) and cross-polar (dotted) patterns at $\phi = 0°$, of CP circular patch antennas of modes 1, 2, and 3, using different substrate relative permittivities. The corresponding patch radius is listed for each antenna configuration. The patterns are symmetric in ϕ.

The CPR, R, as defined in (3.9), using the amplitude ratio, is related to ρ_C using:

$$R = \begin{cases} \rho_C & \text{if RHCP is the co-polarization,} \\ 1/\rho_C & \text{if LHCP is the co-polarization.} \end{cases} \tag{3.10}$$

ρ_C and R are related to the traditional metric of circular polarization purity, the axial ratio, A, using [IEEE, 1979] and [Stutzman, 1993], respectively:

$$A = \frac{\rho_C + 1}{\rho_C - 1}, \qquad |A| = \frac{1 + R}{1 - R}. \tag{3.11}$$

Therefore, a better polarization purity translates into a low value of the CPR or an axial ratio magnitude which is close to 1. Figure 3.5 shows that, for the n=1 mode, the purest polarization is always achieved at broadside, where $R^{[1]}$=0 ($R_{dB}^{[1]}$=$-\infty$) and $|A^{[1]}|$=1.

In multi-faceted antenna arrays, and other practical scenarios outlined in Section 3.1, the antenna is not required to cover all directions, including along the groundplane. This is fortuitous because a finite groundplane affects the accuracy of the ring source model at low-elevation angles, as noted in Section 3.3.1. Instead, the pattern model is only required to cover a limited scan sector around broadside, viz., an angular interval defined as:

$$\{(\theta,\phi) : \theta \in [\theta_1, \theta_2[, 0 \leqslant \theta_1 \leqslant \theta_2 \leqslant \frac{\pi}{2}, \phi \in [0, 2\pi)\}. \tag{3.12}$$

The minimum CPR (corresponding to the best polarization purity) over this scan sector is defined as:

$$R_{\min}^{[n]} = 20 \log_{10} \min_{\theta,\phi} \big(R^{[n]}(\theta,\phi)\big). \tag{3.13}$$

For the broadside mode, θ_1 can be set to 0°. For higher modes, θ_1 should be set to a larger value to maintain a defined value of CPR. Figure 3.5 shows that for the n=1 mode, $R_{\min}^{[1]}$ always occurs at θ=0°, where $|F_{cr}^{[1]}|$ vanishes and hence $R_{\min}^{[1]}$=$-\infty$. For higher modes, $R_{\min}^{[n]}$ varies depending on the extent of the scan sector (the zenith angles θ_1 and θ_2) and it does not occur in the direction where $|F_{co}^{[n]}|$ is maximum. The maximum, or worst, CPR over the scan sector is similarly defined as:

$$R_{\max}^{[n]} = 20 \log_{10} \max_{\theta,\phi} \big(R^{[n]}(\theta,\phi)\big). \tag{3.14}$$

The value of $R_{\max}^{[n]}$ depends on θ_1 and θ_2, as can be seen in Figure 3.5. In general, a search of the 2D space of the pattern functions is required to find $R_{\max}^{[n]}$, and this is non-trivial. Finally, the distributed, or mean, CPR over the scan sector is defined as:

$$\overline{R}^{[n]} = 20 \log_{10} \int_0^{2\pi} \int_{\theta_1}^{\theta_2} p_{\theta,\phi}(\theta,\phi) R^{[n]}(\theta,\phi) \sin\theta d\theta d\phi. \tag{3.15}$$

Here the weighting (pdf) over the angles, in (3.12), is taken as uniform and the same for each polarization, i.e.,

$$p_{\theta,\phi}(\theta,\phi) = \frac{1}{2\pi(\cos\theta_1 - \cos\theta_2)}. \tag{3.16}$$

For example, for zenith to horizon coverage (θ_1=0° and θ_2=90°), $p_{\theta,\phi}(\theta,\phi)=\frac{1}{2\pi}$. Different applications will have different weightings.

3.5 Results

The maximum and distributed CPRs, defined in Section 3.4, represent the upper bounds on the best polarization purity which could be obtained from a circular patch antenna on a large groundplane. Both parameters depend on the extent of the scan sector in elevation, i.e., θ_1 and θ_2.

Figure 3.6 (left) plots the maximum CPR, $R_{\max}^{[n]}$, versus the patch radius, as a/λ_0, for different scan sectors, i.e., different values of the maximum zenith angle, θ_2. For the n=1 mode, the minimum zenith angle, θ_1, is set to 0°, whereas for higher modes, θ_1 is set to 1°. This is sufficient to eliminate the effect of the vanishing $|F_{co}^{[n]}|$ at θ=0°. Results for higher zenith angles, i.e., ranges that are further away from broadside, can be found using (3.14) and a larger value of θ_1. The range of radii in the figure corresponds to substrate relative permittivities varying between 1 (air) and 10 (alumina), as related by (3.1). The figure shows a clear trend of well-defined minima for all scan sectors. Lowest values of $R_{\max}^{[n]}$ are achieved for a certain range of patch radii, depending on the mode. This range corresponds to substrate relative permittivities between 1 and 2. Of course, the lower ϵ_r is, the larger the patch radius will be. For the n=1 mode, low $R_{\max}^{[1]}$ is achieved for patch radii of about $\lambda_0/4$. Examples of substrate materials with low relative permittivities include honeycomb and foam, as proposed in [Huang, 1984] and [Chair et al., 1999], respectively.

Figure 3.6 (right) presents another way to examine the results, which may also be useful for design. It plots $R_{\max}^{[n]}$ versus the maximum zenith angle, θ_2, for different values of the substrate relative permittivity, ϵ_r. Again, θ_1=0° for the n=1 mode, while θ_1=1° for higher modes. The figure shows that as the scan sector gets larger, $R_{\max}^{[n]}$ increases. This is because the polarization purity deteriorates in directions towards the groundplane. Moreover, the figure illustrates the low $R_{\max}^{[n]}$ behavior for lower relative permittivities. Finally, it shows that $R_{\max}^{[n]}$ does not vary significantly for values of ϵ_r larger than 2 (topmost set of curves).

$R^{[n]}_{\max}$ vs. a | $R^{[n]}_{\max}$ vs. θ_2

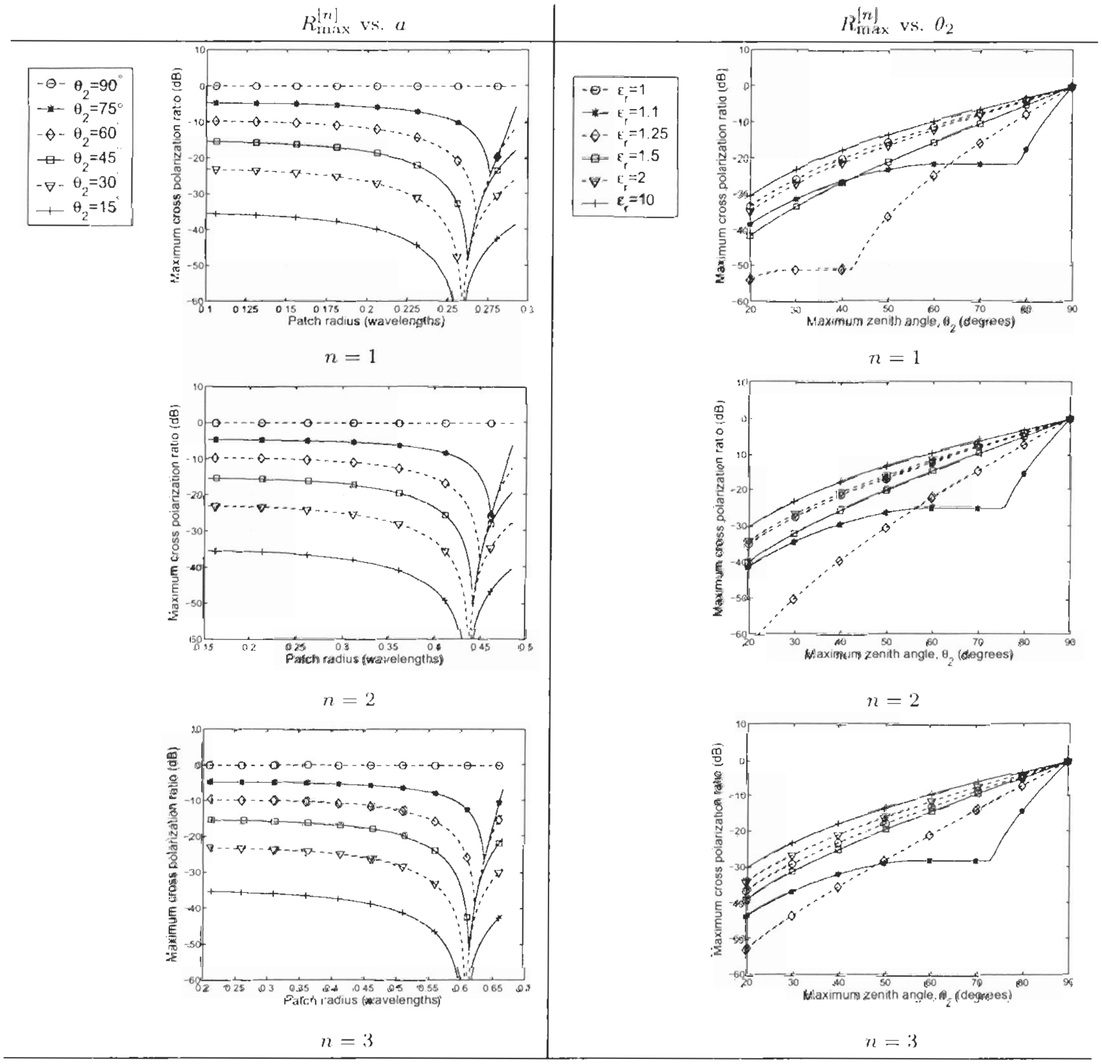

$n = 1$ | $n = 1$

$n = 2$ | $n = 2$

$n = 3$ | $n = 3$

Figure 3.6: The maximum CPR, $R^{[n]}_{\max}$, versus the patch radius, a, (left) and the maximum zenith angle, θ_2, (right) of modes 1, 2, and 3. The range of patch radii (left) is different for each mode. $\theta_1 = 0°$ for $n = 1$, while $\theta_1 = 1°$ for $n \geqslant 2$.

Figure 3.6 (right) also shows a sudden change in the value of $R^{[n]}_{\max}$, for all three modes, near θ_2=75° when ϵ_r=1.1. The reason for this change is that the cross-polar pattern decreases near that angle and then increases rapidly as θ increases, until the co-polar and cross-polar patterns eventually become equal at θ=90°. This can be seen from the pattern cuts shown in Figure 3.5 (second row). The change in the ϵ_r=1.25 curve near θ_2=40° for the broadside mode (n=1) can also be explained using the pattern cuts in Figure 3.5 (left-most figure on the third row). The co-polar pattern starts to decrease near θ=40° while the cross-polar pattern starts to increase near that angle. On the other hand, for the higher modes both the co-polar and cross-polar patterns change smoothly as θ varies between 0° and 90°.

Figure 3.7 shows similar results for the distributed CPR, $\overline{R}^{[n]}$, which is of course less than or equal to $R^{[n]}_{\max}$. It is clear that $\overline{R}^{[n]}$ exhibits similar trends as those exhibited by $R^{[n]}_{\max}$ in Figure 3.6. The results here provide the designer with knowledge of the limiting polarization purity for a large groundplane implementation. For example, Figures 3.6 and 3.7 show that for the n=1 mode, when $\theta \in (0, 30°)$, both $R^{[1]}_{\max}$ and $\overline{R}^{[1]}$ can be reduced dramatically by using a modelled patch radius of $0.26\lambda_0$ (ϵ_r=1.25) instead of, for example, $0.29\lambda_0$ (ϵ_r=1).

Since the magnitude of the axial ratio, $|A|$, and the CPR, R, are related using (3.11), $|A|$ exhibits similar trends as those exhibited by R in Figures 3.6 and 3.7. In other words, a low value of R corresponds to a value of $|A|$ that is close to 1, i.e., 0 dB. Figure 3.8 illustrates an example for the n=1 mode. It plots the maximum axial ratio, $|A^{[n]}_{\max}|$, which corresponds to the maximum CPR, versus the patch radius and the maximum zenith angle, respectively. It exhibits similar behavior to that of $R^{[n]}_{\max}$ shown in Figure 3.6.

Finally, we note that the choice of relative permittivity of about 1.25 for the element has an important impact on an array system. If the array is constructed with a continuous substrate, then this is also near the value which has the least surface wave, and least mutual coupling (Private communication with L. Shafai). So there is a double benefit for array performance by using $\epsilon_r \approx 1.25$. Some foam materials are available for this substrate value.

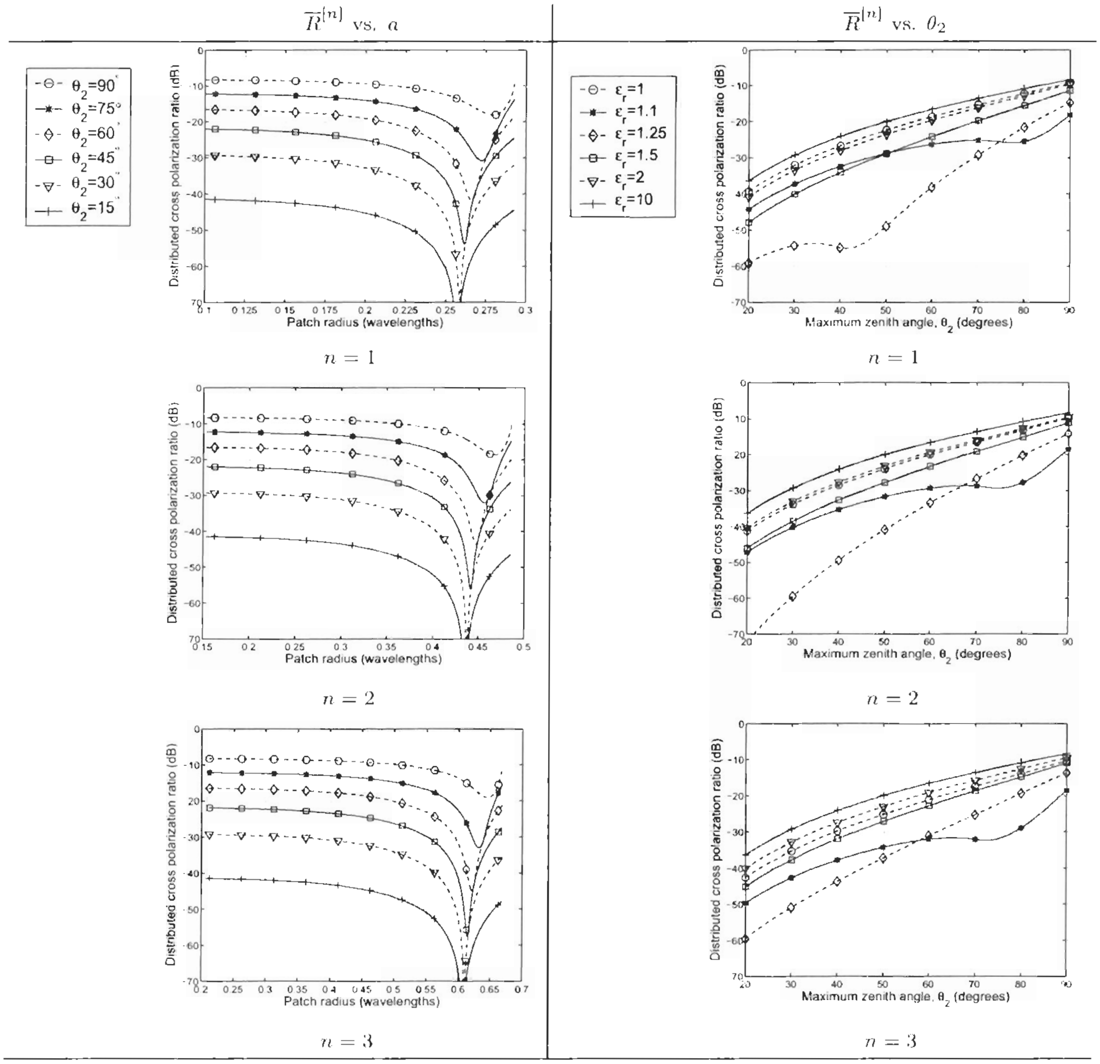

$n = 1$ $n = 1$

$n = 2$ $n = 2$

$n = 3$ $n = 3$

Figure 3.7: The distributed CPR, $\overline{R}^{[n]}$, versus the patch radius, a, (left) and the maximum zenith angle, θ_2, (right) of modes 1, 2, and 3. The range of patch radii (left) is different for each mode. $\theta_1 = 0°$ for $n = 1$, while $\theta_1 = 1°$ for $n \geqslant 2$.

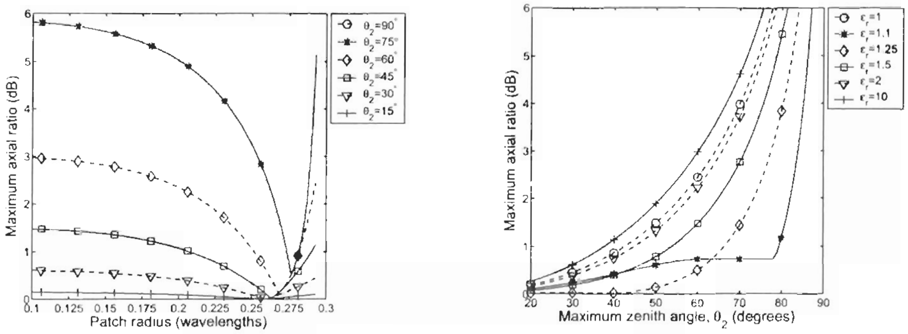

$|A^{[n]}_{\max}|$ vs. a $|A^{[n]}_{\max}|$ vs. θ_2

Figure 3.8: The maximum axial ratio, $|A^{[n]}_{\max}|$, versus the patch radius, a, (left) and the maximum zenith angle, θ_2, (right) of the broadside mode.

3.5.1 Modelled CPR as a Bound for Implemented Patch Antennas With Finite Groundplanes

The results presented in above are accurate for antennas on large groundplanes, including arrays where the mutual coupling can be neglected. In practice, single antennas are often mounted on small groundplanes. As noted above, the results for low-elevation angles cannot be expected to be accurate in such a case. The smaller groundplane can act to improve the circular polarization purity at low-elevation angles since the horizontal component can now propagate in the groundplane directions. A critical comparison of radiation patterns from the idealized ring source model and real-world patch antennas has not been previously discussed in the literature.

Figure 3.9(a) compares the estimated CPR from an alumina patch antenna (ϵ_r=9.9, no centre pin) used for popular commercial GPS antennas from the 1990s [Vaughan and Andersen, 2003, p. 548]. The antenna has a single feed and the mode degeneracy and phasing is introduced by an elliptic patch shape. It has a small $0.33\lambda_0^2$ circular groundplane and this reduces the cross-polar pattern near the groundplane and allows radiation below it as expected. The semimajor axis of the antenna is a=$0.095\lambda_0$, which is equivalent to an *effective* $\epsilon_r^{\mathrm{eff}}$ of 9.5, using (3.1). The measured pattern cut

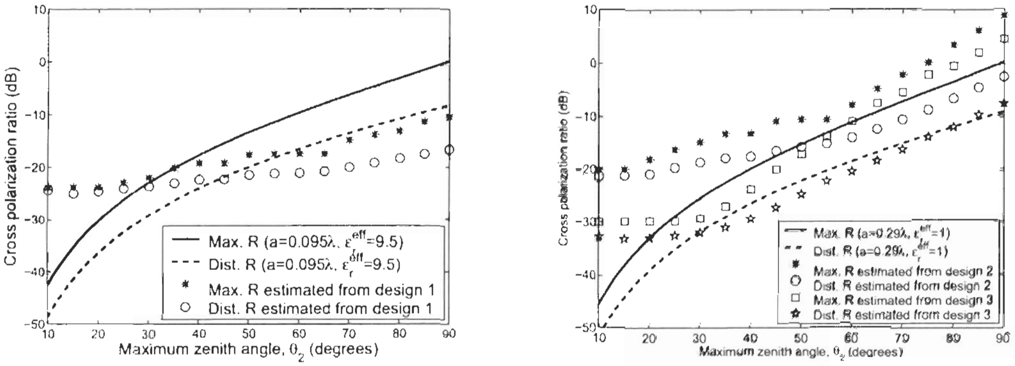

(a) Patch antenna with a small $0.33\lambda_0^2$ groundplane.

(b) Patch antennas with large $21.6\lambda_0^2$ groundplanes.

Figure 3.9: The estimated experimental CPR (points) compared to the bounds found using the ring source model (lines) for the three experimental GPS patch antenna designs reported in [Vaughan and Andersen, 2003], [Boccia et al., 2003], and [Basilio, et al., 2005], respectively.

exhibits a finite cross-polar components around boresight and the difference between the co- and cross-polar CP patterns in that direction is over 20 dB, i.e., $R_{\min}^{[1]} \approx$ -25 dB. Figure 3.9(a) shows $R_{\max}$ and $\overline{R}$ which are estimated from the patterns reported in [Vaughan and Andersen, 2003] compared to the bounds, $R_{\max}^{[1]}$ and $\overline{R}^{[1]}$, derived for a pure-mode ring source using ϵ_r=9.5. (CPR is estimated from the pattern cuts by averaging the two halves of the cut and then taking the pattern as azimuthally symmetric.) The estimated CPRs and those of the ring source differ at low-elevation angles (large θ_2) owing to the small groundplane, and at high-elevation angles (small θ_2) owing to the modal impurity and the limited measurement accuracy.

Figure 3.9(b) compares estimated CPRs from two experimental GPS patch antenna designs, both using a large $21.6\lambda_0^2$ circular groundplane, to the CPR bounds. The first design is a shorted annular elliptical patch with a single feed, ϵ_r=2.55, and a semimajor axis of $0.29\lambda_0$ [Boccia et al., 2003]. The second design is a shorted-annular-ring reduced-surface-wave patch, also with a single feed, ϵ_r=2.94, and a radius of $0.29\lambda_0$ [Basilio et al., 2005]. Using (3.1), the equivalent effective permittivity for both designs is thus $\epsilon_r^{\text{eff}}=1$. Measured pattern cuts of both designs exhibit finite cross-polar components around boresight, similar to the pattern in [Vaughan and Andersen, 2003]. Therefore, the estimated CPRs differ from those of the ring source at high-elevation angles (small θ_2). On the other hand, both designs show reasonably good agreement at low-elevation angles, since they use large groundplanes.

3.5.2 Application to Multi-Faceted Antenna Arrays

To determine the polarization purity achieved by pyramidal and pyramidal frustum arrays, the maximum scan angle, γ, encountered in both structures (Section 2.3) can be combined with the CPR information presented above. Since the individual arrays in either structures are required to scan from their broadside to up to γ, then the broadside mode (n=1) CP patches should be used. Consequently, γ corresponds to the maximum zenith angle, θ_2, in (3.12). The maximum value of θ_2 that needs to be considered is about 63° for pyramids, and about 60° for pyramidal frusta, as can be seen in Figures 2.5(b) and 2.6(b), respectively.

The choice of a certain structure (pyramid or pyramidal frustum) and its number of faces, N, results in a value of γ, and hence θ_2, which can be used to look up the maximum and distributed CPR for an antenna used in that structure. For example, assuming full hemispherical coverage, a 4-face pyramidal frustum has a maximum scan angle of 60°. Using the bottom left sub-figures in Figures 3.6 and 3.7, which correspond to the broadside mode, one can see that the maximum and distributed CPRs for the antenna are about -12 dB and -18 dB, respectively, assuming an air substrate (ϵ_r=1) is used. The maximum CPR is the more relevant quantity here since it represents the worst polarization purity at the specific maximum scan angle of 60°.

Figures 3.10(a) and 3.10(b) depict the maximum and distributed CPRs, respectively, experienced by patch antennas in pyramidal and pyramidal frustum antenna arrays, assuming a full hemispherical coverage requirement. An air substrate is assumed for the patch antenna, i.e., ϵ_r=1. The figure shows how both the maximum and distributed CPRs decrease (or polarization purity increases) as the number of array

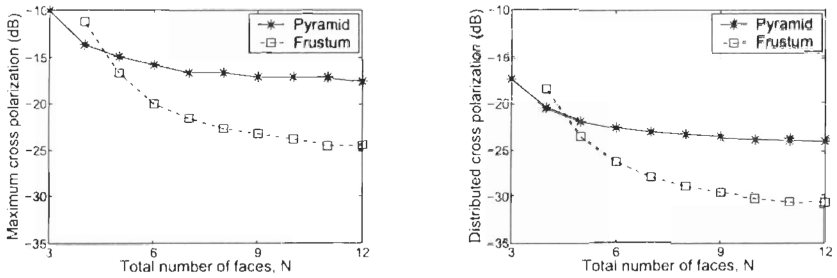

(a) $R_{\max}^{[1]}$ vs. N

(b) $\overline{R}^{[1]}$ vs. N

Figure 3.10: The (a) maximum and (b) distributed CPR for an air-substrate broadside-mode CP circular patch antenna in pyramidal and pyramidal frustum antenna arrays. Full hemispherical coverage is assumed.

faces, N, increases. Similar to the trends exhibited by the maximum scan angle in Figures 2.5(b) and 2.6(b), no significant improvement in the polarization purity is gained by increasing the number of faces of pyramids beyond 7, or pyramidal frusta beyond 10. The figure also shows how using pyramidal frusta results in better polarization purity (lower CPR) than using pyramids, with the exception of the 4-face pyramidal frustum. Again, the maximum CPR is the more relevant quantity because it represents the worst case polarization purity in the coverage range. The distributed CPR gives a metric which allows different elements of different structures to be compared for averaged behavior, suitable for statistical specifications.

3.6 Effect of Implementation Tolerances

Amplitude, phase shift, and feed position tolerances (or deviations from prescribed values) may arise when a circular patch antenna is constructed. For example, amplitude tolerances typically occur due to feed network errors [Smith and Hall, 1994]. Phase shift errors may occur if sections of transmission line are used as phase shifters [Hall et al., 1989]. Feed position tolerances occur when the exact angular separation between feeds, e.g., $\frac{90^\circ}{n}$ for mode n, is not realized in the manufactured antennas, due to limited precision, for example.

Given these three types of tolerances, and assuming a RHCP patch, (3.5) may be re-written as:

$$\mathbf{f}^{[n]}(\theta,\phi) = f_\theta^{[n]}(\theta,\phi)\hat{\theta} + f_\phi^{[n]}(\theta,\phi)\hat{\phi}, \tag{3.17}$$

where the θ- and ϕ-components of the far-field pattern are:

$$\begin{aligned} f_\theta^{[n]}(\theta,\phi) &= E_\theta^{[n]}(\theta,\phi)|_{\phi_0=0^\circ} + (1+\tau_a)\, e^{\,j(1+\tau_p)\frac{\pi}{2}}\; E_\theta^{[n]}(\theta,\phi)|_{\phi_0=(1+\tau_f)\frac{90^\circ}{n}}\;; \\ f_\phi^{[n]}(\theta,\phi) &= E_\phi^{[n]}(\theta,\phi)|_{\phi_0=0^\circ} + (1+\tau_a)\, e^{-j(1+\tau_p)\frac{\pi}{2}}\; E_\phi^{[n]}(\theta,\phi)|_{\phi_0=(1+\tau_f)\frac{90^\circ}{n}}\;; \end{aligned} \tag{3.18}$$

where $E_\theta^{[n]}$ and $E_\phi^{[n]}$ are given in (3.3). The parameters τ_a, τ_p, and τ_f represent tolerances in amplitude, phase shift, and feed position, respectively. For an ideal implementation, $\tau_a = \tau_p = \tau_f = 0$.

Figure 3.11 shows linear plots of the co- and cross-polar patterns, $F_{co}^{[1]}(\theta,\phi)$ and $F_{cr}^{[1]}(\theta,\phi)$, for a broadside-mode patch with an air substrate (ϵ_r=1), with and without implementation tolerances. The patterns are computed using (3.8) and (3.18). The cross-polar patterns are enlarged by a linear factor of six. The figure shows that, in the presence of tolerances, the cross-polar pattern no longer vanishes at broadside. In other words, the polarization at broadside is elliptical, rather than perfectly circular.

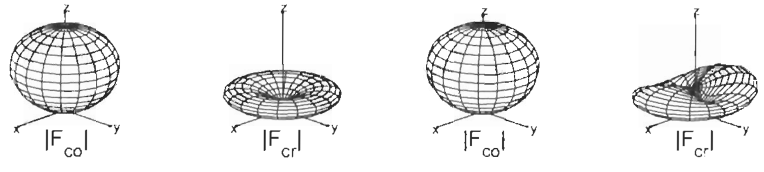

(a) Ideal implementation (b) 10% amplitude tolerance

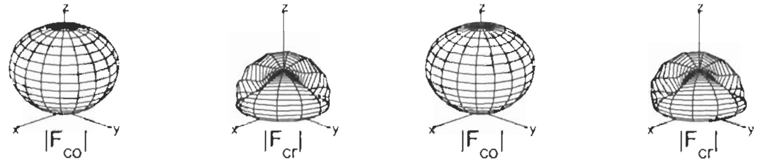

(c) 10% phase shift tolerance (d) 10% feed position tolerance

Figure 3.11: Linear plots of the magnitude of the co- and cross-polar patterns of an air-substrate broadside-mode CP circular patch with and without implementation tolerances. $|F_{cr}(\theta,\phi)|$ is enlarged by a linear factor of 6.

Moreover, tolerances cause the cross-polar patterns to lose their azimuthal symmetry. Finally, the magnitude of the cross-polar pattern increases when tolerances are introduced, resulting in an increased CPR (and hence a decreased polarization purity) in all directions.

Figure 3.12 illustrates how increasing the tolerances τ_a, τ_p, and τ_f, causes the maximum and distributed CPRs to increase, i.e., polarization purity deteriorates. Only broadside mode (n=1) patches are considered, but higher modes exhibit similar behavior. The left, center, and middle columns correspond to τ_a, τ_p, and τ_f, respectively. In each column, one of the tolerances is varied from 0% to 15%, while the other two are set to zero, e.g., in the left column τ_a is varied and τ_p=τ_f=0. Figure 3.12(a) shows the effect of tolerances on the maximum CPR, $R^{[1]}_{\max}$, for four different values of the relative permittivity, ϵ_r, in a fixed scan sector with θ_2=45°. On the other hand, Figure 3.12(b) uses a constant relative permittivity ϵ_r=1 and considers four different scan sectors. Figures 3.12(c) and 3.12(d) show similar results for the average CPR, $\overline{R}^{[1]}$.

The figure shows that the effects of phase shift and feed position tolerances on the CPR are identical as expected. Moreover, the figure shows that the effect of amplitude tolerance is less severe than that of phase shift or feed position tolerances. As the tolerances increase, the increase in CPR is more pronounced for the design parameters that lead to better purity in the ideal (no tolerance) case, shown in Figures 3.6 and 3.7. For example, Figure 3.12(a) (left) shows that an amplitude tolerance of 5% causes an increase of about 12 dB in the maximum CPR when ϵ_r=1.25, while it causes only a 2 dB increase for ϵ_r=10. This is because the CPR for high values of ϵ_r is already much lower than that for low ϵ_r, as can be seen in Figures 3.5, 3.6, and 3.7. Similarly, a phase shift tolerance of 5% causes a deterioration of the maximum CPR of about 12 dB for the narrowest scan sector (θ_2=15°), but only about 1 dB for the widest scan sector (θ_2=60°), as shown in Figure 3.12(b) (center).

3.7 Summary

This chapter presented techniques for characterizing the polarization purity of circularly polarized circular patch antennas, in terms of the cross polarization ratio. Simple

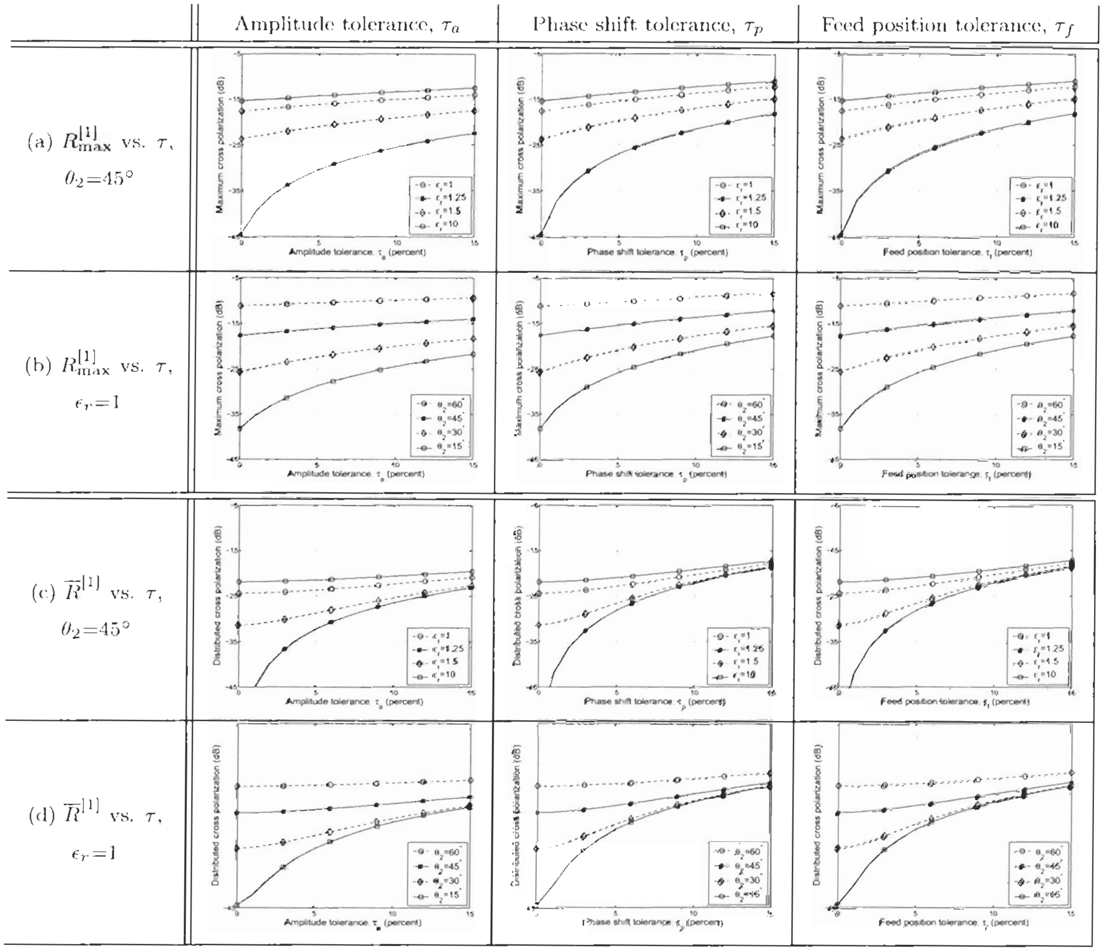

Figure 3.12: The effect of amplitude, phase shift, and feed position tolerances on the maximum and distributed CPRs of broadside mode patches.

models were used to represent the far-field radiation pattern of broadside and higher order mode patches. The broadside mode is the relevant mode for multi-faceted antennas, while higher order modes are used in other applications, e.g., rooftop-mounted vehicular antennas for terrestrial links. The complex vector polarization representation was then used to obtain the co- and cross-polar patterns and cross polarization ratios. The maximum and distributed cross polarization ratios were computed over angular sectors about the broadside direction of the patch, and presented as design curves which are functions of the patch size. These angular sectors correspond to the coverage areas of the arrays in a multi-faceted antenna. The models were also used to investigate the effect of implementation tolerances on polarization purity. The following conclusions can be drawn from the presented results:

- Numerical results show how the polarization purity degrades as the coverage area of the antenna is enlarged.
- The results show that there is a well-defined optimal patch size for each mode which produces extremely pure polarization. From the cavity model, this occurs for patch antennas with specific substrate relative permittivities between 1 and 2. For the broadside radiation mode, this corresponds to patch radii around $\lambda_0/4$ and a substrate relative permittivity of about 1.25 in a normal patch construction.
- Comparison with experimental patch antenna designs demonstrates that the numerical results serve as upper bounds for the polarization purity of patch antennas on large groundplanes.
- The effect of amplitude tolerance is less severe than that of phase shift or feed position tolerances. However, the presence of any tolerance reduces the polarization purity of the patch.

Moreover, when patch antennas are used as the antenna elements in multi-faceted antenna arrays, the patch coverage only extends to at most 63° degrees about the patch broadside direction. This is fortuitous since the models used cannot be expected to be accurate in directions close to the groundplane. Finally, numerical results were presented to demonstrate how the polarization purity increases as the number of array faces in a multi-faceted antenna array is increased.

Chapter 4

Planar Array Design

The chapter deals with the design of the individual antenna arrays supported by the faces of a multi-faceted antenna. The design of phased array antennas is a research area in its own right and numerous specialized texts have been written on it, e.g., [Mailloux, 1994] and [Hansen, 1998]. Therefore, the work presented here focuses on how the environment and requirements of multi-faceted antennas influence the choice of the different array parameters. A brief overview of related previous work is presented first. This is followed by the details involved in choosing a few key array parameters for the purpose of the evaluation and comparison undertaken in Chapter 5.

4.1 Previous Work

Many of the previous works which addressed multi-faceted antenna arrays or arrays with special limited scan requirements (Section 2.2) also addressed the design of the individual planar arrays. Sharp (1961) showed that the total number of elements in a planar antenna array with a given aperture area can, in general, be reduced by arranging the elements in a equilateral triangular, or hexagonal, grid as opposed to a rectangular grid. This reduction depends on the coverage requirement. The maximum reduction of 13.4% is achieved when the main beam is to be scanned within a conical volume about broadside. Such a coverage requirement applies for the top face of a pyramidal frustum, as explained in Section 2.1.

Knittel (1965) used the hexagonal grid to compare the performance of 3- and 4-face pyramids and 5- and 6-face pyramidal frusta. He set the element spacing to permit only grating lobes (GLs) at endfire for some scan angles and assumed circular radiating apertures were used on each face. Jamnejad, et al. (2002) also assumed the use of circular array apertures. Kmetzo (1967) computed the element spacing of a 5-face pyramidal frustum to avoid the formation of GLs in the visible space. He compared the use of rectangular, hexagonal, and isosceles triangular element grids in that frustum, and showed that the latter requires the least number of elements.

Corey (1985) also used the hexagonal grid and determined the element spacing for a single array given a coverage range that is limited in elevation and azimuth (this requirement is similar to that of a side face in a pyramid or a pyramidal frustum). He used an iterative graphical technique to determine the array elevation and element spacing such that GLs do not appear in visible space while either (a) minimizing the maximum scan angle, or (b) maximizing the element spacing.

Waters, et al. (1998) assumed the use of square array apertures where elements are laid on a hexagonal grid, and applied Corey's method to determine the element spacing, in order to compare 3-, 4-, and 5-face pyramidal arrays. Jablon and Agrawal (2006) also used square arrays, a hexagonal grid, and Corey's method to determine the optimal element spacing, to compare 3- and 4-face pyramidal arrays.

The previous work outlined above is summarized in Table 4.1. Details about the definitions of basic and optimal element spacings will be given in Section 4.3 below. All references listed above assumed that the array elements were isotropic, i.e., only the planar array factor rather than some realized radiation pattern is considered. Moreover, all assumed that the element excitation was uniform. The following sections describe the criteria used here for choosing the different array parameters for performance evaluation purposes (Chapter 5).

Table 4.1: A summary of previous work in designing the individual planar arrays supported by the faces of pyramidal and pyramidal frustum antenna arrays.

Source	Grid	Element spacing	Aperture shape
Sharp (1961)	Hexagonal	Basic†	None*
Knittel (1965)	Hexagonal	Basic†	Circular
Kmetzo (1967)	Rectangular, hexagonal, isosceles triangular	Optimal†	None*
Corey (1985)	Hexagonal	Optimal†	None*
Waters, et al. (1998)	Hexagonal	Optimal†	Square
Jamnejad, et al. (2002)	None*	None*	Circular
Jablon and Agrawal (2006)	Hexagonal	Optimal†	Square

* No specific assumption were made about the corresponding array parameter.

† The definitions of basic and optimal spacing will be given in Section 4.3.

4.2 Element Grid

The element grid, or lattice, refers to how the antenna elements are laid out in a planar array. The element grid, together with the element spacing, determine the location of the GLs of the array factor, as will be shown in Section 4.3. Regular grid layouts are commonly used in planar arrays. Examples of such grids include rectangular, square, equilateral triangular, and isosceles triangular grids. Figure 4.1 depicts the structure of these grid shapes and illustrates the relationship between the element spacing in the x and y directions in each of them, d_x and d_y, respectively. Of course, the square grid is a special case of the rectangular grid, while the equilateral triangular grid is a special case of the isosceles triangular grid. The equilateral triangular grid is also referred to as "hexagonal". This notation is adopted here.

In a rectangular or an isosceles triangular grid, there are two degrees of freedom for placing the array elements, i.e., d_x and d_y are independent. On the other hand, there is only one degree of freedom in square and hexagonal grids, where $d_x = d_y$ and $d_x = \sqrt{3}d_y$, respectively. Therefore, it is simpler to optimize the element spacing when

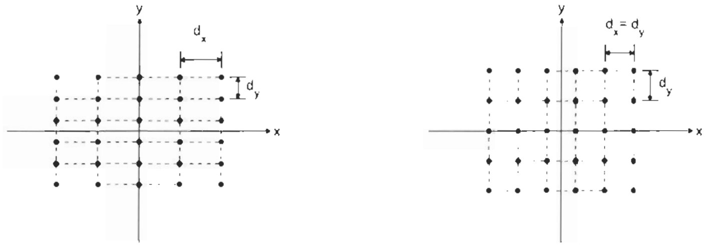

(a) Rectangular (b) Square

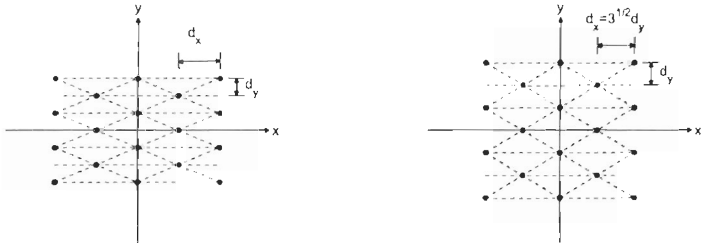

(c) Isosceles triangular (d) Equilateral triangular (hexagonal)

Figure 4.1: The structure of commonly used regular element grids. Array elements are shown as filled circles.

a square or a hexagonal grid is used. Moreover, the grid shape also affects the shape of the main beam of the array factor at broadside. Both the square and hexagonal grids result in main beams with equal beamwidths in the xz and yz planes. For these two reasons, both square and hexagonal grids will be considered for the antenna array evaluation in Chapter 5. Another reason for using hexagonal grids is that they reduce the total number of elements (and hence the overall system cost) for a given aperture area [Sharp, 1961], as noted in Section 4.1.

Another alternative for element layout is the use of thinned arrays. In such arrays, elements may be randomly spaced, space tapered, or removed from a regular grid, thereby reducing the array gain without significantly changing its beamwidth [Mailloux, 1994]. The gain reduction corresponds to also having higher sidelobes. Algorithms for thinning of regular grids include statistical and pseudo-random thinning, or thinning using some optimization method such as genetic algorithms, e.g., [Haupt, 2006]. The topic of thinned arrays, however, is out of the scope of this work, and only regular grids will be considered.

4.3 Element Spacing

The spacing between array elements is determined to prevent the formation of GLs in the visible space. For regular grids, the location of GLs is determined only by the grid shape and the element spacing (d_x and d_y), and is independent of the array aperture size and shape [Sharp, 1961].

To prevent the peaks of GLs from forming in the visible space when the array is scanned in the principal planes (ϕ=0° and ϕ=90°), the element spacing should be chosen such that, e.g., [Hansen, 1998]:

$$\begin{aligned} \frac{d_x}{\lambda} &\leqslant \frac{1}{1+\sin\gamma}, \\ \frac{d_y}{\lambda} &\leqslant \frac{1}{1+\sin\gamma}, \end{aligned} \tag{4.1}$$

where γ is the maximum scan angle of the array, measured from its broadside. The equality in (4.1) means that GLs will form at endfire (i.e., in the plane of the array). For a given element spacing, as the scan angle increases, GLs appear in the principal planes before they appear in the inter-cardinal planes. This is why the element spacing is chosen using (4.1). Equation (4.1) applies for the four grid types shown in Figure 4.1. For square and hexagonal grids, since d_x and d_y are related, as noted in Section 4.2, (4.1) reduces to:

$$\frac{d_x}{\lambda} \leqslant \frac{1}{1+\sin\gamma}, \qquad d_y = \begin{cases} d_x & \text{for a square grid,} \\ d_x/\sqrt{3} & \text{for a hexagonal grid.} \end{cases} \tag{4.2}$$

The spacing computed using (4.2) will be referred to here as the "basic spacing".

Equation (4.2) assumes that the beam is scanned within a cone with an opening angle of 2γ. This coverage range applies only for the top face of a pyramidal frustum, but not for the side faces of a pyramid or a pyramidal frustum, as explained in Section 2.1. Corey (1985) proposed a graphical technique to determine the element spacing, which makes use of the special shape of the coverage region. Hence, his technique is believed to result in a larger element spacing (i.e., less elements) than that computed using (4.2). The spacing computed using Corey's method is referred to here as the "optimal spacing". Only the minimum scan design criteria will be used here owing to its relevance to the evaluation methodology used in Chapter 5.

Figure 4.2(a) illustrates the difference between the two methods, with the aid of a GL diagram. The figure assumes a 4-face pyramid with full hemispherical coverage. The diagram plots the GL regions and scan coverage regions on the *uv*-, or direction cosine, plane. For a given element spacing on a hexagonal grid, the centers of the six closest GL circles to the scan regions are located at the *uv* pairs (starting on the positive u axis and going counterclockwise) $(\frac{\lambda}{d_x}, 0)$, $(\frac{\lambda}{2d_x}, \frac{\lambda}{2d_y})$, $(\frac{-\lambda}{2d_x}, \frac{\lambda}{2d_y})$, $(\frac{-\lambda}{d_x}, 0)$, $(\frac{-\lambda}{2d_x}, \frac{-\lambda}{2d_y})$, and $(\frac{\lambda}{2d_x}, \frac{-\lambda}{2d_y})$. The first method assumes a conical coverage region, $\theta \in [0, \gamma]$, which translates into the thick dashed circle on the diagram. The values of d_x and d_y computed using (4.2) are such that the GLs (thin dashed lines) are tangent to the coverage region, which locates the GLs at endfire. If the spacing is made any smaller, the GL circles intersect with the scan region and the peaks of the grating move into the visible space.

Corey's method makes use of the actual shape of the coverage region, bounded by the thick solid curves. By considering this shape, it is easy to see that the GL circles can be moved further towards the coverage region until they touch. This translates into a larger element spacing, and hence a saving in the number of elements required. The significance of this saving is, of course, influenced by the amount of spacing

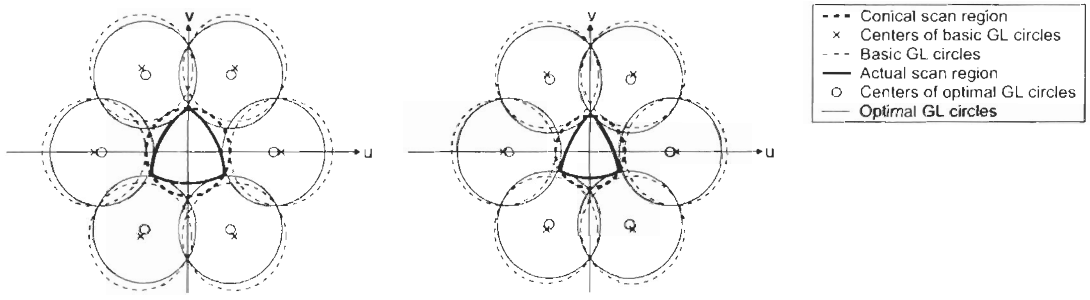

(a) 4-face pyramid, $\theta \in [0°, 90°]$ (b) 5-face pyramid, $\theta \in [5°, 75°]$

Figure 4.2: Illustration of how the basic and optimal element spacings are computed.

increase as well as the aperture size, i.e., the larger the spacing increase and the aperture size are, the more significant the cost saving will be. Figure 4.2(b) shows another example which considers a 5-face pyramid with a limited coverage range, $\theta \in [5°, 75°]$. The coverage range for a side face in a pyramidal frustum will have a similar shape.

Corey's method has been widely used for multi-faceted antenna arrays, e.g., [Waters et al., 1998], [Jablon and Agrawal, 2006]. Therefore, it is useful to compare it thoroughly to the basic method. As part of this work, Corey's method has been implemented numerically in order to carry out the comparison. The implementation makes use of the symmetry of the GL diagram about the v-axis, as shown in Figure 4.2, and hence only 3 GL circles are considered. The points on the coverage region that are closest to the GL circles resulting from the basic spacing are then determined. Finally, the optimal spacing is determined such that the new GL circles touch the coverage region at these points.

Figure 4.3 compares the optimal spacing, d_o, to the basic spacing, d_b, for pyramidal and pyramidal frustum arrays with different numbers of faces. The figure considers all valid coverage ranges, i.e., $\theta_1 < \theta_2$. It displays the percentage difference computed as:

$$\delta = 100 \times \frac{d_o - d_b}{d_b}. \tag{4.3}$$

The value of δ is gray-scale coded. So, for example, white areas indicate that $d_o = d_b$, while the darkest shade of gray indicates that $5\% < \delta \leqslant 10\%$. The figure shows that the improvement obtained using Corey's method is always less than 10%, and is within 2% for most coverage ranges.

In practice, however, the element spacing may need to be reduced below the values computed above to avoid array, or scan, blindness. Array blindness is a phenomenon that results from the mutual coupling between array elements and leads to the cancellation of the element radiation at certain scan angles [Knittel et al., 1968]. Several studies examined the effects of array blindness for different types of array elements, e.g., [Pozar and Schaubert, 1984], [Pozar, 1985]. Such studies have led to design guidelines that require the element spacing to be a few percent below the values computed above [Mailloux, 1994]. Therefore, although the improvement gained using

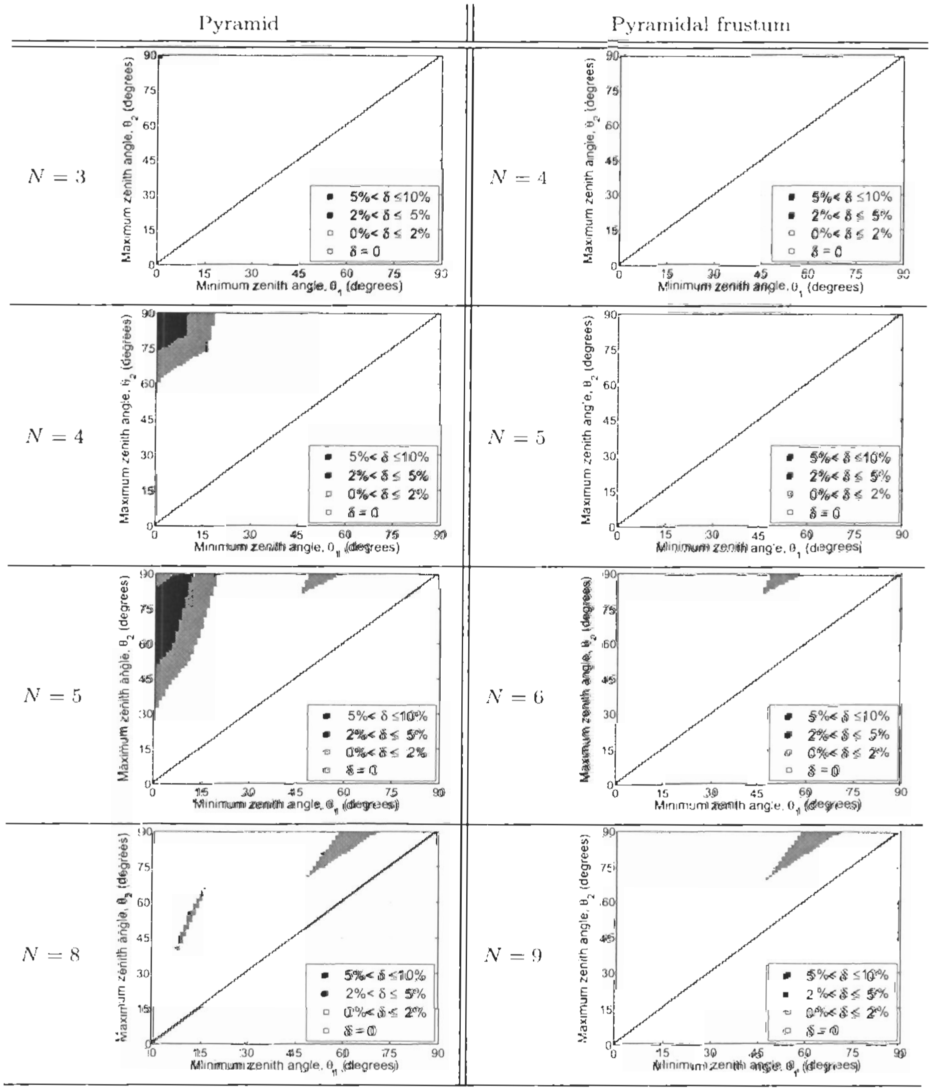

Figure 4.3: The percentage difference between the optimal, d_o, and basic, d_b, element spacing, $\delta = 100 \times (d_o - d_b)/d_b$, for pyramidal and pyramidal frustum arrays. The darker the shade, the larger the value of δ. Valid coverage ranges have $\theta_1 < \theta_2$.

Corey's method does not seem to be significant (only a few percent), it can certainly offset some or all of the element spacing reduction required to avoid scan blindness, especially for large arrays.

4.4 Element Excitation

The isotropic array factor of a planar antenna array scanned to a direction (θ_0, ϕ_0) is given by (Section A.5.2):

$$F_A(\theta, \phi) = \sum_m \sum_n a_{mn} e^{jk\left(md_x(\sin\theta\cos\phi - \sin\theta_0\cos\phi_0) + nd_y(\sin\theta\sin\phi - \sin\theta_0\sin\phi_0)\right)}, \tag{4.4}$$

where the array elements are laid out on a rectangular grid with spacing d_x and d_y, N_x and N_y are the numbers of elements in the x and y directions, respectively, and $m = 0, 1, \ldots, (N_x - 1)$, $n = 0, 1, \ldots, (N_y - 1)$. a_{mn} is the relative excitation of the element at row m and column n in the array. The array factors of arrays with triangular grids can be computed as the superposition of the array factors of two arrays with a rectangular grid. Alternatively, the appropriate a_{mn} may be set to zero to reflect the triangular grid, e.g., $a_{mn} = 0$ if $m + n$ is odd.

The relative excitation of the elements of an array affects the beam shape, in terms of the beamwidth and sidelobe ratio. Uniform excitation, where elements are excited with currents that are equal in amplitude and in phase, results in a smaller beamwidth and a higher gain, at the cost of a higher sidelobe ratio. Alternatively, tapered excitation, where currents are in phase but their amplitudes are monotonically decreased for elements away from the array center, generally results in a lower sidelobe ratio at the expense of a larger beamwidth and a reduction in gain.

A lot of research work has been done on the topic of planar array synthesis and various methods exist for synthesizing different array patterns, e.g., [Elliott, 2003]. However, this work only considers uniform element excitation similar to previous work in multi-faceted antennas, as outlined in Section 4.1. Arrays with uniform excitation are simpler to model and more generic than arrays with other illumination distributions. Hence, they are more appropriate for the performance evaluation presented in Chapter 5.

4.5 Array Aperture Shape

The shape of a uniformly illuminated array aperture affects the distribution of the sidelobes of its array factor. Figure 4.4 illustrates contour plots of the array factor for square and circular apertures. Both square and hexagonal grids are considered. All apertures have roughly the same area, $\approx 7.5\lambda_0^2$, and number of elements (between 121 and 129). The figure shows that the sidelobe distribution is dominated by the aperture shape, while the grid shape has a minor influence. The figure also shows that for the circular aperture, the sidelobe envelope decays more or less uniformly with θ. Such a behavior can be achieved using square apertures but only when special element excitations (other than uniform) are considered, e.g., [Kim and Elliott, 1988].

For multi-faceted antenna arrays, other aperture types may be used such as triangles for pyramidal arrays, trapezoids for the side faces of pyramidal frusta, and

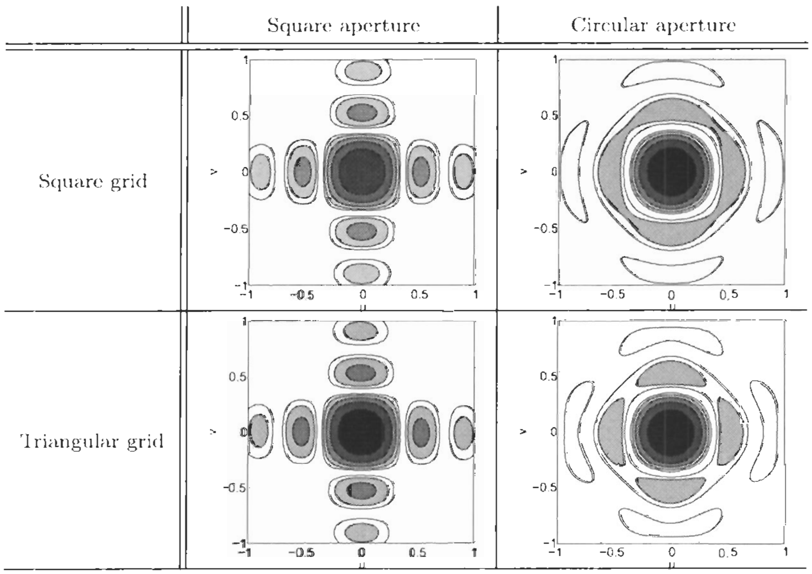

Figure 4.4: The effect of aperture shape and grid type on the distribution of the sidelobes of the array factors. All apertures shown have an area of about $7.5\lambda_0^2$ and contain between 121 and 129 elements.

$(N-1)$-side regular polygons for the top faces of pyramidal frusta. However, to facilitate the comparison between the planar, pyramidal, and pyramidal frustum antenna arrays, only square and circular apertures will be considered, since they can easily be inscribed within any face shape.

4.6 Summary

This chapter focused on the design of the planar antenna arrays supported by the faces of a multi-faceted antenna array. An overview of previous work was presented. Then, a detailed explanation for the choice of a few key array parameters was presented. These chosen parameters will be used in the following chapter for evaluation. They include:

- Using square or hexagonal element grids. These grids result in broadside beams with circular cross sections and lend themselves to easier determination of the element spacing.
- Using an optimized method, which makes use of the special shape of the coverage regions in multi-faceted antennas, to determine the largest possible element spacing.
- Using uniformly excited elements in square or circular array apertures because they are simple and appropriate for the purpose of performance evaluation and comparison.

Furthermore, an assessment of the improvement gained by using the optimized method to determine the element spacing, over all valid coverage ranges of moderate-size pyramids and pyramidal frusta, was presented. A comparison between the optimized method and the basic formula typically used to determine the element spacing showed that the optimized method reduces spacing by at most 10% below the basic formula, and is generally within about 2% for most coverage ranges. Although this improvement may not seem significant enough, it can be used to compensate for some or all of the element spacing reduction needed to avoid array blindness.

Chapter 5

Performance Evaluation and Comparison

This chapter concerns the performance evaluation of multi-faceted antenna arrays. It is emphasized that the different performance metrics presented here are only estimates of the performance of implemented antennas. The assumptions used for performance estimation are outlined wherever necessary. For brevity, "performance" is used here to refer to the "estimated performance".

In this chapter, previous work is first reviewed, then the performance evaluation and comparison framework developed here is presented. The comparison includes planar, pyramidal, and pyramidal frustum antenna arrays. The evaluation is performed at different levels of details, i.e., using the geometric structure alone, then incorporating the isotropic array factor, and finally including both the modelled and the simulated element pattern of the CP patch antenna.

5.1 Previous Work

The purpose of the evaluation stage is to determine the optimal multi-faceted antenna array structure by comparing the different structures with respect to meaningful cost functions. Traditionally, structures were compared based on the number of array faces, N, as elaborated below.

Knittel (1965) considered 3- and 4-face pyramids and 5- and 6-face pyramidal frusta. He computed the degradation in the beamwidth and gain caused by beam scanning, by modelling the phased array as an infinite flat current sheet [Wheeler, 1965] which is impedance matched at broadside and has a resistive mismatch over the scan range. He compared the relative total number of elements and individual array diameters (assuming circular arrays) of the four antenna structures, given equal gain or equal beamwidth at the maximum scan angles. The comparison showed that the 4-face pyramid and the 6-face frustum required the least number of elements for equal gain and equal beamwidth at maximum scan, respectively. The results also showed that the 6-face frustum required the smallest array diameter and had the lowest degradation in gain and beamwidth, since it has the smallest maximum scan angle among the four antenna structures.

Waters, et al. (1998) compared 3-, 4-, and 5-face pyramids supporting active arrays for surveillance radars with respect to volume scanning time. The volume scanning time refers to the time required to point the antenna beam in all possible positions within a hemispherical volume, such that the beams overlap at their 3 dB points. They assumed that the detection performance is the same in all beam positions and that the total number of elements (T/R modules) was constant and divided equally among the arrays. The individual arrays had a square aperture and elements were laid out on a hexagonal grid. They also assumed that the array gain varies as the cosine of the scan angle, $\cos^n \gamma$, and used two different values of n; 1 and 1.5. The comparison showed that the 3-face pyramid was the best choice, i.e., it had the least volume scanning time, for both values of n and for coverage extending from zenith (θ_1=0°) to horizon (θ_2=90°) or to 45° elevation (θ_2=45°).

Jamnejad, et al. (2002) compared the diameters of the individual arrays in a 4-face pyramid and a 7-face pyramidal frustum such that they provide the same gain as a 70-meter diameter reflector, operating in the Ka-band, at 10° elevation. The gain was assumed to vary as the cosine of the scan angle. The diameters were found to be 83 and 75 meters, respectively. Alternatively, if each face supported a 70-meter circular array, the gain at maximum scan would be 1.5 dB and 0.6 dB lower than that at broadside for the pyramid and the frustum, respectively. Therefore, the 7-face frustum is better than the 4-face pyramid in the sense that it has lower scan loss and smaller array diameter, at the expense of a larger footprint and 3 extra arrays.

Trunk (2003) compared 3- and 4-face pyramids, also with respect to the scanning time for volume surveillance. He used a slightly different model for the gain variation from that used in [Waters et al., 1998]: gain was assumed to vary as $\cos^n \gamma$, where n was set to 1.25 till 45° scan and increased linearly to 1.4 at 60° scan. He also included the effects of fill pulses for the pulse-Doppler waveforms used to detect targets in clutter. He concluded that the 3- and 4-face systems were essentially equivalent in performance.

Jablon and Agrawal (2006) compared the total number of elements required in 3-face and 4-face pyramidal active array radars used for shipboard and land-based tracking and discrimination functions. They assumed that the both structures had equal power-aperture-gain (PAG) product at the respective maximum scan angles. The individual arrays were assumed to have a square aperture and elements were laid out on a hexagonal grid. The two criteria proposed in [Corey, 1985] were used to determine the array face elevation angle (Section 4.1). Finally, the gain was assumed to vary as $\cos^n \gamma$ and two sets of values were considered: n=1.4 for the 3-face system and 1.25 for the 4-face system; and n=2 for the 3-face system and 1.4 for the 4-face system. The results showed that in all scenarios considered (i.e., two face elevation angles and two sets of n) the 4-face system required less elements than the 3-face system.

Josefsson and Persson (2006) compared 3- and 4-face pyramids with respect to the minimum effective area, given that both antennas fit within a constant base diameter. The minimum effective area is defined as the projection of the array aperture area in the direction perpendicular to the direction of maximum scan, i.e., the aperture area times $\cos \gamma$. They showed that the the 4-face pyramid was better since it had a larger minimum effective area than the 3-face pyramid, since its maximum scan angle, γ, is smaller.

Table 5.1 summarizes the previous work outlined above. The table shows that previous evaluation methods only considered the geometric structure of the arrays, i.e., the face elevation and the corresponding maximum scan angles. Every method

Table 5.1: A summary of previous work in performance evaluation of multi-faceted antenna arrays.

Source	Structures considered	Cost function	Optimal structure
Knittel (1965)	3- and 4-face pyramids and 5- and 6-face pyramidal frusta	Total number of elements	4-face pyramid for equal gain, 6-face frustum for equal beamwidth
Knittel (1965)	3- and 4-face pyramids and 5- and 6-face pyramidal frusta	Array diameters	6-face frustum
Waters, et al. (1998)	3-, 4-, and 5-face pyramids	Volume scanning time	3-face pyramid
Jamnejad, et al. (2002)	4-face pyramid and 7-face frustum	Gain	7-face frustum
Trunk (2003)	3- and 4-face pyramids	Volume scanning time	Both are equivalent
Jablon and Agrawal (2006)	3- and 4-face pyramids	Total number of elements	4-face pyramid
Josefsson and Persson (2006)	3- and 4-face pyramids	Minimum effective area	4-face pyramid

only compared a few structures (e.g., 3-, 4-, 5-face pyramids) and most methods dealt only with pyramids. Moreover, most methods considered specific applications, e.g., radar surveillance, and hence the results are not readily applicable or easily extendable to other applications. It is worth noting that no single structure is optimal based on all cost functions, a fact that is typical in many engineering problems where different specifications and tradeoffs must be considered.

5.2 Evaluation Framework

In this work, previously used cost functions (Table 5.1), along with a new set of generic cost functions, are applied to N-face pyramids and N-face pyramidal frusta, as well as planar antenna arrays. The new cost functions include antenna dimensions, scan loss, and directivity. Moreover, four levels of detail are used for evaluation, namely: using the geometric structure only; using the antenna array factor; and using both the modelled; and the simulated radiation patterns of the CP patch antenna chosen here as the antenna element. Finally, all cost functions are used to compare planar, pyramidal, and pyramidal frustum antenna arrays.

5.2.1 Evaluation Based on Geometric Structure

The first level of evaluation considers only the geometric structure of the antenna arrays, i.e., the total number of faces, N, and ignores aspects such as the element pattern and mutual coupling. It is assumed that the optimal face elevation angle computed using the minimax-based approach (Section 2.3.2) is used for each structure.

Maximum Scan Angle

The maximum scan angle encountered by an array is a dominant design factor that affects the system cost. The gain of an array decreases as the beam is scanned away from broadside. Moreover, for the antenna element, gain and polarization purity also fall off away from broadside. In other words, some element types only allow scanning within a very limited range about broadside, without a significant loss in performance, as was demonstrated for the circular patch antenna in Chapter 3.

The maximum scan angle, γ, for a multi-faceted array can be determined based on its geometric structure only, i.e., its face elevation, ψ, and total number of faces, N. Considering factors such as finite distances between the target and the antenna and finite antenna dimensions causes γ to increase. However, since the increase is very small, as shown in Section 2.4, these factors will not be considered here.

Kmetzo (1967) compared the maximum scan angle of N-face pyramids and N-face pyramidal frusta, but only for full hemispherical coverage (Section 2.2). Given a general hemispherical scan coverage requirement of the form:

$$\{(\theta, \phi) : \theta \in [\theta_1, \theta_2], 0 \leqslant \theta_1 < \theta_2 \leqslant \frac{\pi}{2}, \phi \in [0, 2\pi)\}, \tag{5.1}$$

the maximum scan angle for a planar array is always equal to θ_2 (Section 2.5). For the pyramidal and pyramidal frustum arrays, the maximum scan angles are computed using the minimax-based approach, as described in Section 2.3.2.

Figure 5.1 compares the maximum scan angles for the three structures for two different coverage ranges. The figure shows how using multi-faceted arrays significantly reduces the maximum scan angle compared to planar arrays, for both coverage ranges. It also shows that for a given number of array faces, N, pyramidal frusta are better than pyramids, with the exception of the 4-face pyramidal frustum. Finally, no significant reduction in the maximum scan angle, γ, is achieved by using pyramids with $N > 7$ or frusta with $N > 10$, as explained in Section 2.6.

An alternative way for comparison is shown in Figure 5.2. It illustrates how (a) enlarging and (b) shrinking the coverage range affects the maximum scan angle for a planar, a 5-face pyramidal, and a 6-face pyramidal frustum array. For θ_1=0°, Figure 5.2(a) shows that as θ_2 increases, the pyramidal frustum exhibits the largest reduction in γ. The reduction becomes more pronounced as θ_2 increases. On the other hand, Figure 5.2(b) shows how γ changes as θ_1 increases, given a constant θ_2. For small values of θ_1, the pyramidal frustum has the lowest maximum scan angle. However, as θ_1 increases that it satisfies the condition in (2.14), γ for both the pyramid and the pyramidal frustum become identical. This means that θ_1 is so far below zenith that the top face becomes unnecessary, as explained in Section 2.3.1.

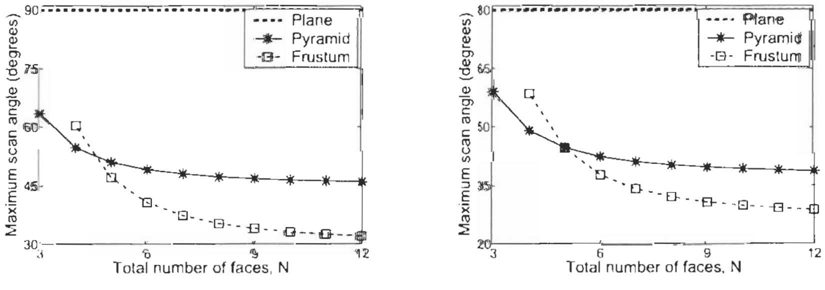

(a) $\theta \in [0°, 90°]$

(b) $\theta \in [5°, 80°]$

Figure 5.1: The maximum scan angle of planar, pyramidal, and pyramidal frustum antenna arrays, for two different coverage ranges.

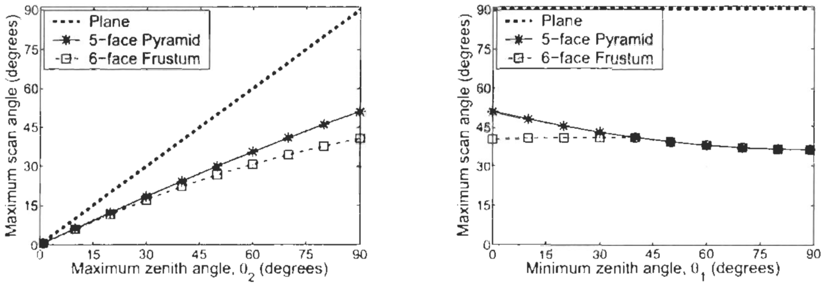

(a) $\theta_1=0°$, $\theta_2 \in (0°, 90°]$

(b) $\theta_1 \in [0°, 90°)$, $\theta_2=90°$

Figure 5.2: The maximum scan angle of a planar, a 5-face pyramidal, and a 6-face pyramidal frustum antenna array, versus: (a) the maximum zenith angle, θ_2 with $\theta_1=0°$; and (b) the minimum zenith angle, θ_1 with $\theta_2=90°$.

Beamwidth Broadening

The beamwidth of an antenna is a measure of the angular extent over which the largest portion of the radiated power is concentrated. The resolution of an antenna, when used for surveillance and tracking, for example, is inversely proportional to the beamwidth: the smaller the beamwidth, the higher the resolution. The beamwidth of a phased array antenna broadens as the beam is scanned away from broadside. For very large arrays with narrow beams, the beamwidth increases by approximately a factor of $1/\cos\gamma$, as a result of scanning, where γ is the scan angle [Elliott, 2003]. In other words, the ratio of the broadside to scanned beamwidth is:

$$R_{\mathrm{BW}}(\gamma) = \cos\gamma. \tag{5.2}$$

This relationship is valid provided that the beam is not scanned to within a beamwidth of endfire, which is the case for multi-faceted antenna arrays. At and near endfire, other formulas that incorporate the size of the antenna array and the wavelength should be used [Mailloux, 1994].

Figure 5.3 plots the ratio R_{BW} versus the total number of faces, N, in pyramids and pyramidal frusta, as well as for a single planar array. The coverage range considered is $\theta \in [0°, 75°]$. The plot exhibits a similar trend to the maximum scan angle (shown

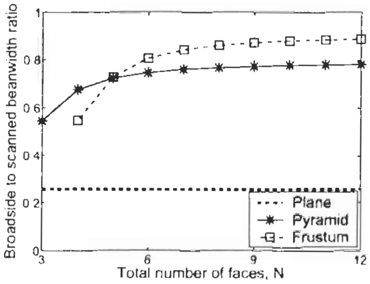

Figure 5.3: The approximate ratio of broadside to scanned beamwidth for planar, pyramidal, and pyramidal frustum arrays, assuming large arrays with narrow beams. The coverage range used is $\theta \in [0°, 75°]$.

in Figure 5.1), as can be seen in (5.2). Therefore, multi-faceted arrays have lower variation in beamwidth ratio than planar arrays. Also, for a given number of faces, pyramidal frusta are better than pyramids, for values of N larger than 4 or 5.

Antenna Dimensions

The height and footprint of the antenna are important design factors that affect the system cost, as in shipboard and vehicular applications, for example. To illustrate, assume that the antenna is enclosed within a footprint of radius R and that each face supports a circular planar arrays as shown in Figure 5.4. For the multi-faceted arrays, it is assumed that all faces support identical arrays for simplicity. (The antenna dimensions are computed as described in Appendix C).

Figure 5.5(a) depicts the antenna height H, normalized by R, versus the total number of faces for the coverage range $\theta \in [0°, 75°]$. For the multi-faceted arrays, this is the height of the pyramidal frustum or the pyramid when it is truncated just above the arrays on the side faces, as shown in Figure 5.4. The planar array has the smallest height; it is set to zero, since only the geometric structure is considered, i.e., the height of elements, groundplane, or feed networks is ignored. The figure shows how the pyramidal structure is shorter than the pyramidal frustum for $N > 4$. This is because the optimal face elevation of the pyramid is lower than that of the frustum for this coverage range.

Figure 5.5(b) plots the area, A, of the circular arrays supported by each of the

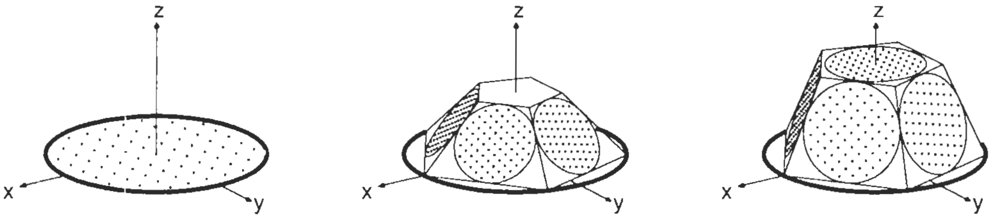

(a) Plane (b) Pyramid (c) Pyramidal frustum

Figure 5.4: Illustration of the constant footprint radius, R, enclosing planar, pyramidal, and pyramidal frustum antenna arrays. The circle of radius R is shown using the thick line.

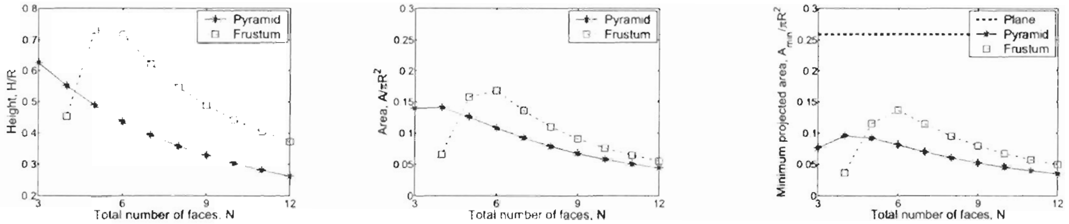

(a) Antenna height (b) Physical aperture area (c) Minimum projected aperture area

Figure 5.5: The antenna dimensions given a footprint of constant radius, R, for planar, pyramidal, and pyramidal frustum antenna arrays. The coverage range used in this figure is $\theta \in [0°, 75°]$. The height of the planar array is zero and its physical aperture area is πR^2.

faces, normalized by πR^2, versus the total number of faces. The planar array has the largest normalized area, which is equal to 1. The figure shows that, for a given footprint, the pyramidal frustum supports arrays that are larger than those supported by a pyramid, with the exception of the 4-face frustum.

Figure 5.5(c) plots the minimum projected area, $A_{\min}$, of the circular arrays supported by each of the faces, normalized by πR^2, versus N. $A_{\min}$ is the same as the minimum effective area used in [Josefsson and Persson, 2006] for pyramidal arrays, as mentioned in Section 5.1. It follows a similar trend as the physical area, A. Figures 5.5(b) and 5.5(c) also show that for a given footprint, A and $A_{\min}$ are maximized when using 4-face pyramids and 6-face pyramidal frusta.

Geometric Directivity

The directivity of an antenna compares the radiation intensity in a given direction to the average intensity (Section A.4). For large arrays, the maximum directivity, or "geometric directivity", is achieved using uniformly illuminated isotropic elements. At broadside, the geometric directivity is expressed as [Mailloux, 1994]:

$$\tilde{D}_{\text{broadside}} = \frac{4\pi A}{\lambda_0^2}, \tag{5.3}$$

where A is the physical aperture area and λ_0 is the wavelength. Therefore, the geometric directivity is directly proportional to the number of array elements for a given element spacing, regardless of the aperture shape. For a given footprint and wavelength, $\tilde{D}_{\text{broadside}}$ is thus directly proportional to the area, A, depicted in Figure 5.5(b). Therefore, the figure shows that the planar array has the largest geometric directivity at broadside, followed by the pyramidal frustum, then the pyramid, with the exception of the 4-face frustum. The figure also shows how the geometric directivity decreases as N increases, for the pyramid and pyramidal frustum.

When the array antenna is scanned, the geometric directivity varies as the projected aperture area [Mailloux, 1994], i.e.:

$$\tilde{D}_{\text{scanned}} = \frac{4\pi A}{\lambda_0^2} \cos\gamma, \tag{5.4}$$

where γ is the scan angle. Therefore, the minimum geometric directivity is proportional to the minimum projected area, A_{min}, depicted in Figure 5.5(c). This reduction in geometric directivity is due to the increased beamwidth, and does not include scan loss. The figure shows that, with the exception of the 4-face frustum, the pyramidal frustum exhibits larger geometric directivity than that of the pyramid at maximum scan. It also shows that the 6-face frustum has the largest geometric directivity among frusta, while the 4-face pyramid has the largest geometric directivity among pyramids. Although the planar array has the largest geometric directivity among the three structures for the coverage range $[0°, 75°]$, once scan losses are considered, the multi-faceted arrays outperform the planar array, as will be shown below.

Scan Loss

The gain of an antenna is also an important design parameter that affects the cost of the antenna system. It compares the radiation intensity in a given direction to the average intensity, while accounting for the power losses in the antenna material [Elliott, 2003]. The relationship between the gain, G, of an antenna array and the antenna directivity, D, is given by [Mailloux, 1994]:

$$G(\theta, \phi) = \epsilon_L(1 - |\Gamma|^2)D(\theta, \phi), \tag{5.5}$$

where ϵ_L accounts for circuit element losses and Γ is the voltage reflection coefficient. It can be seen that Γ is taken as an effective value which is the same for each element and that ϵ_L covers losses in both the elements and the combiner. D is computed using (A.8) and thus includes the element pattern and the array factor, unlike the geometric directivity, $\tilde{D}$. For very large arrays, as the beam is scanned away from broadside, the beamwidth broadens by a factor of $1/\cos\gamma$, as seen in (5.2). The directivity is inversely proportional to the beamwidth, i.e., the smaller the beamwidth, the larger the directivity. The directivity is thus directly proportional to the aperture projection, and is reduced by $\cos\gamma$ as a result of scanning. A decrease in directivity results in a decrease in gain, as seen from (5.5). This reduction in gain is referred to as the scan loss.

Two models are commonly used to approximate the mismatch loss term, L_m=$(1 - |\Gamma|^2)$, in (5.5). The first model, used in [Knittel, 1965] and [Josefsson and Persson, 2006], uses the infinite current sheet model [Wheeler, 1965]. The infinite current sheet is the limiting case for an array of many closely spaced small electric dipoles. It is impedance matched at broadside and has a purely resistive impedance which varies as $\cos\gamma$ in the E-plane and as $1/\cos\gamma$ in the H-plane. The magnitude of the resulting voltage reflection coefficient in both planes is thus $|\Gamma|$=$\tan^2\gamma/2$. Therefore, the mismatch loss, L_m, is expressed as:

$$L_m(\gamma) = (1 - |\Gamma(\gamma)|^2) \approx 1 - \tan^4\frac{\gamma}{2}. \tag{5.6}$$

The second model, used in [Mailloux, 1994], [Waters et al., 1998], [Trunk, 2003], and

[Jablon and Agrawal, 2006], approximates L_m as:

$$L_m(\gamma) = (1 - |\Gamma(\gamma)|^2) \approx \cos^{n-1} \gamma, \tag{5.7}$$

where $n \geqslant 1$ is the loss exponent which depends on the array elements and plane of scan. Different values of n have been proposed as shown in Section 5.1. Therefore, the dB scan loss at the maximum scan angle, γ, may be expressed as:

$$L(\gamma) = 10 \log_{10} \frac{1}{L_m(\gamma) \cos \gamma} = \begin{cases} 10 \log_{10} \frac{1}{(1 - \tan^4 \frac{\gamma}{2}) \cos \gamma} & \text{Model 1,} \\ 10 \log_{10} \frac{1}{\cos^n \gamma} & \text{Model 2,} \end{cases} \tag{5.8}$$

where L_m represents the mismatch loss and the $\cos \gamma$ term reflects the aperture projection. Note that neither model incorporates the circuit losses. L is a positive quantity that measures the difference between the gain at broadside and that at the maximum scan angle.

Figure 5.6 illustrates the relationship between L computed using the two models and γ. The figure shows that the difference between the two models is within a fraction of a dB for scan angles less than about 30°, regardless of the value of n. It also shows that the two models are very similar for n=1.25, as suggested in [Josefsson and Persson, 2006]. Lower values of n may be used for slot or dipole arrays in one plane of scan, while higher values of n are needed for arrays of printed elements, e.g., microstrip patches, since they suffer more severe degradation [Mailloux, 1994]. Therefore, n is set to 1.5 here, a value also suggested by R. C. Hansen (Private communication with R. Vaughan).

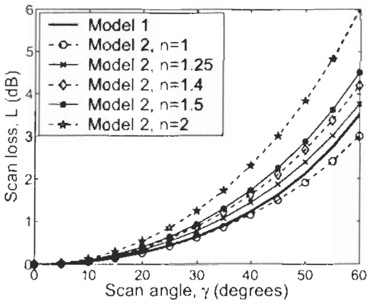

Figure 5.6: The relationship between the scan loss computed using the infinite current sheet model and the $\cos^n \gamma$ model for commonly used values of n.

Figure 5.7 compares the scan loss encountered in planar, pyramidal, and pyramidal frustum antenna arrays, using the second scan loss model, for the coverage range $\theta \in [0°, 75°]$. It shows how multi-faceted arrays encounter much lower scan loss than the planar array. Using $N \geqslant 5$ array faces results in a scan loss that is less than 3 dB, and pyramidal frusta are superior to pyramids for such values of N.

Equation (5.8) can be used to choose among the three array structures as follows. Given a maximum acceptable value of L, $L_{\max}$, (5.8) is used to map it into a maximum acceptable value of γ, $\gamma_{\max}$. Then, based on the required coverage range, one can use design curves such as those given in Figure 5.1 to choose the simplest array structure having a maximum scan angle that is less than or equal to $\gamma_{\max}$.

An example is shown in Figure 5.8(a). $L_{\max}$ is set to 3 dB and all valid coverage ranges are considered with increments of 1° in θ_1 and θ_2. $L_{\max}$ is translated into a $\gamma_{\max}$ of 51° using (5.8). Then, for every coverage range, the three array structures are examined in descending order with respect to simplicity. In other words, a plane is considered first, then a 3-face pyramid, then a 4-face pyramid, then a 4-face frustum, then a 5-face pyramid, and so on. Finally, the simplest array structure with $\gamma \leqslant \gamma_{\max}$ is selected. In the figure, the symbols l, p_i, and f_j refer to planar, i-face pyramidal, and j-face pyramidal frustum arrays, respectively. Figure 5.8(a) shows that a planar array is sufficient for coverage ranges with $\theta_2 \leqslant 51°$. Then, pyramidal arrays should be used, since they reduce γ below θ_2.

Three other examples are shown in Figures 5.8(b) through 5.8(d), where $L_{\max}$ is set to 2.5 dB, 2 dB, and 1.5 dB, respectively. The corresponding values of $\gamma_{\max}$

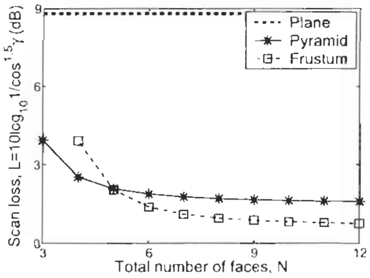

Figure 5.7: The scan loss, L=$10 \log_{10} \cos^{-1.5} \gamma$, for planar, pyramidal, and pyramidal frustum antenna arrays. The coverage range used in this figure is $\theta \in [0°, 75°]$.

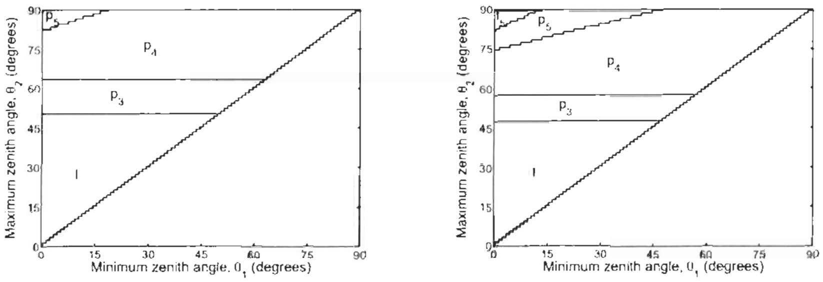

(a) $L_{\max}$=3 dB, $\gamma_{\max}$=51° (b) $L_{\max}$=2.5 dB, $\gamma_{\max}$=47°

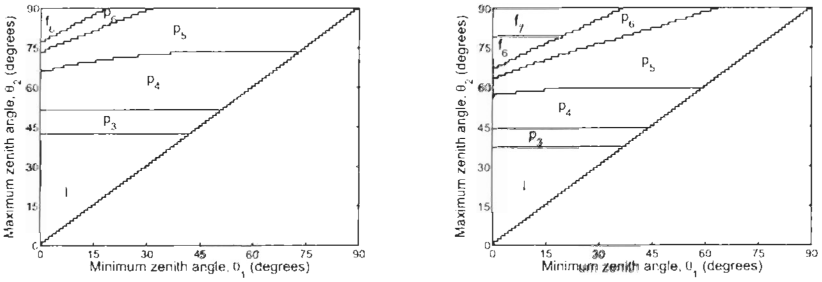

(c) $L_{\max}$=2 dB, $\gamma_{\max}$=43° (d) $L_{\max}$=1.5 dB, $\gamma_{\max}$=37°

Figure 5.8: Choosing among planar, pyramidal, and pyramidal frustum arrays based on a maximum acceptable scan loss, $L_{\max}$, of (a) 3 dB, (b) 2.5 dB, (c) 2 dB, and (d) 1.5 dB. The symbols l, p_i, and f_j refer to planar, i-face pyramid, and j-face pyramidal frustum, respectively. Valid coverage ranges have $\theta_1 < \theta_2$.

are 47°, 43°, and 37°. In these cases, a planar array is good only for $\theta_2 \leqslant \gamma_{\max}$. Then, pyramidal arrays need to be used for larger coverage ranges. For the largest ranges, pyramidal frusta should be used, since they provide a significant reduction in γ, compared to pyramids. The conclusions are that (i) planar arrays are sufficient for narrow coverage ranges around zenith, (ii) pyramidal arrays should be used for narrow coverage ranges away from zenith or when high scan losses can be tolerated, and (iii) pyramidal frusta should be used when only low scan losses are acceptable. Although these conclusions are intuitively obvious, the design curves shown in Figure 5.8 present explicit quantitative boundaries between the different decision regions.

Total Number of Elements

A large portion (70-80%) of the total cost of an antenna array is due to components such as antenna elements, phase shifters or time delay modules, and power supplies [Jablon and Agrawal, 2006]. The cost of these components is directly proportional to the total number of array elements. A simple model was presented in [Knittel, 1965] to compare the total number of elements in pyramidal arrays to achieve either equal gain or equal scan plane beamwidth at the respective maximum scan angle. The model represents the array using the infinite current sheet model described above, and thus the element pattern is not included. This model is adapted and extended here to consider pyramidal frustum and planar arrays, as well as incorporate the two scan loss models presented above and two different methods to compute the element spacing.

The number of elements required to achieve equal gain at the maximum scan angles is determined as follows. Since gain is directly proportional to the face aperture area, and gain is also proportional to the scan loss, L, (the ratio of gain at broadside to that at maximum scan given in (5.8)), then:

$$\begin{array}{rcll} \text{Single array area} & \propto & L(\gamma), & \\ E_a(\gamma) \times \text{Element area} & \propto & L(\gamma), & E_a : \text{Number of element per array}, \\ E_a(\gamma) & \propto & \frac{1}{d^2}L(\gamma), & d : \text{Element spacing}, \end{array} \qquad (5.9)$$

where $\propto$ denotes "proportional to", and a linear (rather than a dB) scale is used for L. The above formula is valid for square or hexagonal element grids, where the element areas are equal to d^2 and $2d^2$, respectively. Therefore, the total number of elements, E_t, in planar, pyramidal, and pyramidal frustum arrays is given by:

$$E_t(\gamma) \propto \begin{cases} E_a(\gamma_l) & \text{plane}, \\ NE_a(\gamma_p) & \text{pyramid}, \\ E_a(\gamma_{f_1}) + (N-1)E_a(\gamma_f) & \text{frustum}, \end{cases} \qquad (5.10)$$

where γ_l, γ_p, and γ_f are the maximum scan angles encountered by planar, pyramidal, and pyramidal frustum arrays, respectively, for a given coverage range. γ_{f_1} is the maximum scan angle for the top face of the frustum. It is always less than or equal to γ_f, and hence the element spacing, d, for the top face is always greater than or equal to that of the side faces.

The number of elements required to achieve equal scan plane beamwidth at the maximum scan angles can be determined in a similar manner. The scan plane beamwidth is inversely proportional to the array length along that plane. Therefore, the face area is inversely proportional to the square of the beamwidth, i.e.,

$$\begin{aligned} \text{Single array area} &\propto \frac{1}{(R_{\mathrm{BW}}(\gamma))^2}, \\ E_a(\gamma) \times \text{Element area} &\propto \frac{1}{(R_{\mathrm{BW}}(\gamma))^2}, \\ E_a(\gamma) &\propto \frac{1}{d^2}\frac{1}{(R_{\mathrm{BW}}(\gamma))^2}, \end{aligned} \tag{5.11}$$

where $R_{\mathrm{BW}}(\gamma)$ is the ratio of broadside to scanned beamwidth given in (5.2). The total number of elements, E_t, can then be computed using (5.10).

Figure 5.9 illustrates how the total number of elements, E_t, varies in planar, pyramidal and pyramidal frustum antenna arrays, for the coverage range $\theta \in [0°, 75°]$. The two methods presented in Section 4.3 to compute the element spacing are used (left and right columns). For equal gain at the maximum scan angles (top), E_a is computed using (5.9), and E_t is normalized by the total number of elements in a 4-face pyramid. For equal beamwidth (bottom), E_a is computed using (5.11), and E_t is normalized by the total number of elements in a 7-face frustum. The thin dashed lines mark $\pm 10\%$ around the values of E_t used for normalization.

The figure shows that the 4-face pyramid requires the least number of elements among pyramids. The total number of elements in 6- and 7-face frusta are roughly the same, and are the lowest among frusta. However, depending on the scan loss model and the element spacing, other structures require a comparable (within $\pm 10\%$) number of elements, such as the 5-face pyramid. For small values of N, both pyramids and pyramidal frusta require less elements than the planar array, since their maximum scan angles are much lower. Finally, for large N, E_t increases almost linearly. This is because such large values of N reduce the maximum scan angle very slightly causing E_a to remain more or less constant, while E_t still increases as NE_a, as shown in (5.10).

	Basic element spacing	Optimal element spacing
Equal gain at the maximum scan angles	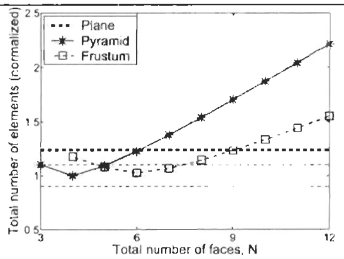 (a) $L=1/\left((1-\tan^4\frac{\gamma}{2})\cos\gamma\right)$	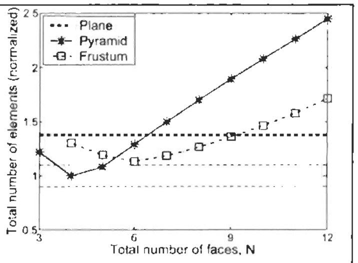 (b) $L=1/\left((1-\tan^4\frac{\gamma}{2})\cos\gamma\right)$
	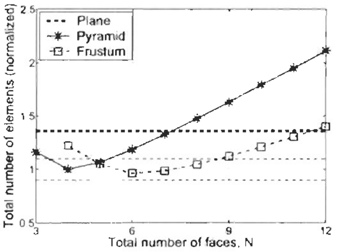 (c) $L=1/\cos^{1.5}\gamma$	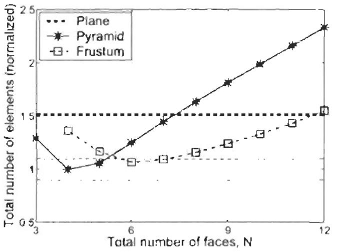 (d) $L=1/\cos^{1.5}\gamma$
Equal scan plane beamwidth at the maximum scan angles	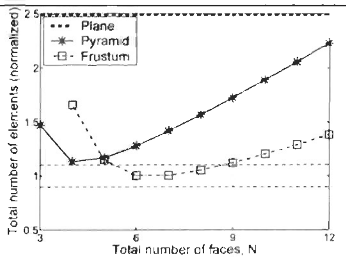 (e) $R_{BW}=\cos\gamma$	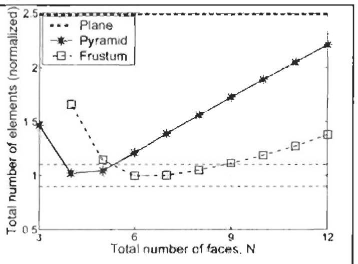 (f) $R_{BW}=\cos\gamma$

Figure 5.9: The total number of elements, E_t, in planar, pyramidal and pyramidal frustum antenna arrays, for the coverage range $\theta \in [0°, 75°]$. Two methods to compute the element spacing are used. For equal gain at the maximum scan angles (top), two models for the scan loss, L, are used and E_t is normalized by E_t of the 4-face pyramid. For equal beamwidth (bottom), E_t is normalized by E_t of the 7-face frustum.

5.2.2 Evaluation Using The Array Factor

The second level of evaluation considers not only the geometric structure of each antenna, but also its array factor. The array factor considers the layout, number, and excitation of the array elements, assuming all elements are isotropic (Section A.5), i.e., the element pattern is not included at this level. Therefore, while the cost functions computed in Section 5.2.1 typically assumed very large arrays, this section explicitly considers the structure of the planar antenna arrays supported by each face in a pyramidal of pyramidal frustum antenna. The planar array structure refers to the array aperture size and the distribution of antenna elements within it.

It is important to note that the maximum scan angles and the antenna dimensions computed in Section 5.2.1 still apply at this level, as well as the two following levels. This is because both cost functions are only affected by the geometry of the antenna structure. Beamwidth broadening and directivity will be considered at this level, since they are influenced by the planar array structure. The scan loss can be computed at this level, since the gain is approximately equal to the product of the directivity and the mismatch loss, as shown in (5.5). Either one of the two models of the mismatch loss introduced in (5.8) may be used. Because these relations are approximate, it is sufficient here to compute the directivity, since computing the approximate gain will not add any more insight than that presented in Section 5.2.1. The total number of elements required by the different structures, for a given footprint, is also examined.

The antenna is assumed to fit within a footprint of radius R. All array elements are assumed to be identical, isotropic, and uniformly excited, and mutual coupling is ignored. Two aperture shapes are considered, namely, square and circular. Two element grids are used: a square grid using the basic element spacing, and a hexagonal grid using the optimal element spacing. More details on the choice of these array parameters can be found in Chapter 4.

Beamwidth

The half-power, or 3 dB, beamwidth, $\theta_{3\text{dB}}$, of a large, uniformly illuminated linear array is given by [Hansen, 1998]:

$$\theta_{3\text{dB}} = \sin^{-1}\left(\sin\theta_0 + 0.4429\frac{\lambda_0}{Nd}\right) - \sin^{-1}\left(\sin\theta_0 - 0.4429\frac{\lambda_0}{Nd}\right), \tag{5.12}$$

where, θ_0 is the scan angle, N is the number of elements and d is the element spacing. The constant 0.4429 is the half-power point of the sinc function, which approximates the array factor of a large, uniformly illuminated linear array. Equation (5.12) can be used to compute the beamwidth in either of the principal scan planes of a uniformly illuminated square array, with elements laid out on a square grid. In this case, $N = N_x = N_y$ is the number of elements along either side of the square, and $d = d_x = d_y$ is the corresponding element spacing. The beam collapses near endfire, where the beamwidth may be approximated using:

$$\theta_{3\text{dB}} \approx \sqrt{\frac{0.8858\lambda_0}{Nd}}, \quad \text{if } \theta_0 > \sin^{-1}\left(1 - 0.4429\frac{\lambda_0}{Nd}\right), \tag{5.13}$$

if the array is over a ground screen. Without the ground screen, $\theta_{3\text{dB}}$ is double that is given in (5.13). Equations (5.12) and (5.13) are used here to compute the beamwidth when square apertures with square grids are used. Scanning the beam to endfire may result in increased directivity (The Hansen-Woodyard condition). However, this condition is not applicable here.

No exact formulas exist for computing the beamwidth for aperture shapes other than square or rectangular apertures or for element grids that are not square or rectangular. Instead, the beamwidth must be computed graphically or numerically from the array factor (Equation (A.18)). Here, the beamwidth is computed numerically when circular apertures and/or hexagonal grids are used.

Directivity

In general, it is necessary to use approximate formulas to determine the directivity of a planar array [Hansen, 1998]. No simple closed-form formula exists, even for rectangular apertures with rectangular grids. Instead, it is necessary to compute the array directivity using (Section A.4):

$$D(\theta,\phi)=\frac{|F(\theta,\phi)|^2}{\frac{1}{4\pi}\int_0^{2\pi}\int_0^{\pi}|F(\theta',\phi')|^2\sin\theta' d\theta' d\phi'}. \tag{5.14}$$

The integral in the denominator of (5.14) is computed numerically here.

Results

Figure 5.10 depicts the beamwidths and directivities computed for planar, pyramidal, and pyramidal frustum arrays. A circle is first inscribed in each array face, then a square aperture is inscribed inside that circle, and a square element grid is used. Two footprint radii are considered, $R = 8\lambda_0$ (top) and $R = 16\lambda_0$ (bottom). The coverage range used in this figure is $\theta \in [0°, 75°]$.

Figure 5.10(a) plots the ratio of the beamwidth at broadside to that at the maximum scan angle for each antenna structure (plane, pyramid, and pyramidal frustum). The figure exhibits a similar trend, with slightly different values, as Figure 5.3, which only assumed a very large aperture and did not consider the planar array structure. A very good match, however, is obtained using the larger footprint radius as shown in Figure 5.10(f).

Figures 5.10(b) and 5.10(g) depict the broadside directivity for the two footprint radii, respectively. The figures show similar trends as those shown in Figure 5.5(b), i.e., (i) the planar array has the largest directivity, (ii) the 4-face pyramid has the largest directivity among pyramids but the 3- and 5-face pyramids are within 2 dB from it, and (iii) the 6-face frustum has the largest directivity among frusta but the directivities of the 5- and 7-face frusta are very similar. The results obtained using the larger footprint, $R = 16\lambda_0$, more closely resemble those in Figure 5.5(b).

Figures 5.10(c) and 5.10(h) depict the directivity at maximum scan for the two footprint radii. respectively. The planar array still has the largest directivity. However, its directivity at maximum scan is about 9 dB less than the directivity at broadside, as opposed to a drop of 4 to 5 dB for the multi-faceted antennas. The 4-face pyramid has the largest directivity among pyramids, followed by the 3- and 5-face pyramids, while the 6-face frustum has the largest directivity among frusta, followed by the 5- and 7-face frusta. Again, a better match to Figure 5.5(c) is obtained using the larger footprint, $R = 16\lambda_0$.

To put these results into perspective, Figures 5.10(d) and 5.10(e), and 5.10(i) and 5.10(j), compare the number of elements and the planar array aperture areas used by the planar array, and that used by each face array in pyramidal and pyramidal frustum antennas, for the two footprint radii, respectively. Although the planar array has the largest directivity at broadside and maximum scan, it requires roughly 10 times as many elements and 6 times the area as a single face array. Therefore, for a small number of faces, N, multi-faceted antennas require a smaller total number of elements than the planar array.

Figures 5.11 and 5.12 show similar results for square and circular array apertures, respectively. Hexagonal grids with optimal element spacing are used in both apertures. The trends exhibited in the figures are very similar to those of the square apertures with square element grids (Figure 5.10), in terms of beamwidth ratio, broadside and maximum scan directivities, number of elements, and aperture area. The circular apertures are directly inscribed in each array face, and thus their areas are larger than the square apertures. Consequently, they also require more elements. Also, the advantage of the 4-face pyramid and the 6-face frustum, in terms of the directivity at maximum scan, is only noticeable for the large footprint ($R = 16\lambda_0$), while it disappears for the small footprint ($R = 8\lambda_0$).

5.2.3 Evaluation Using the Modelled Element Pattern

This level of the evaluation framework deals with the modelled array pattern. In other words, it considers the geometric structure of each antenna, the array factor of the individual planar array, and the modelled element pattern. A broadside LHCP ideal patch with a foam substrate ($\epsilon_r = 1.25$) is assumed, and its element pattern is computed using (3.6). The array pattern is computed as the product of the modelled element pattern and the array factor using (A.11), i.e., mutual coupling is neglected.

The results presented in Section 5.2.2 were more or less the same, regardless of the

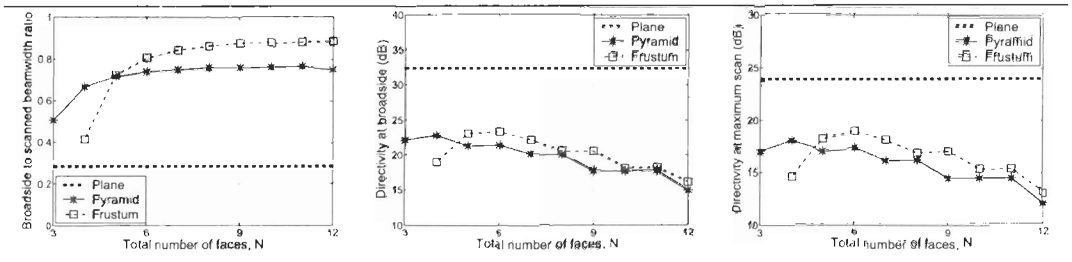

(a) Beamwidth ratio (b) Directivity at broadside (c) Directivity at maximum scan

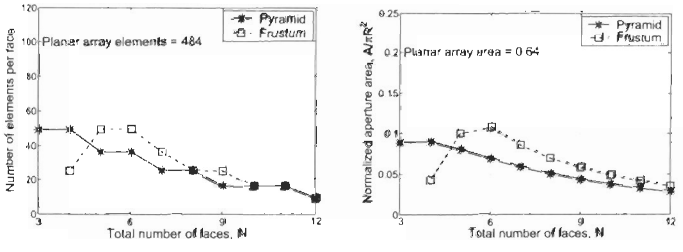

(d) Number of array elements (e) Normalized array area

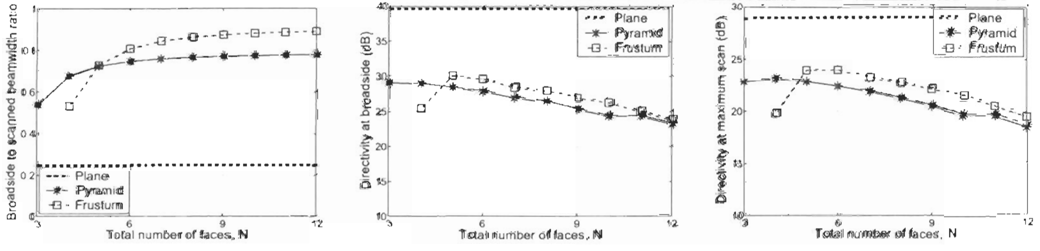

(f) Beamwidth ratio (g) Directivity at broadside (h) Directivity at maximum scan

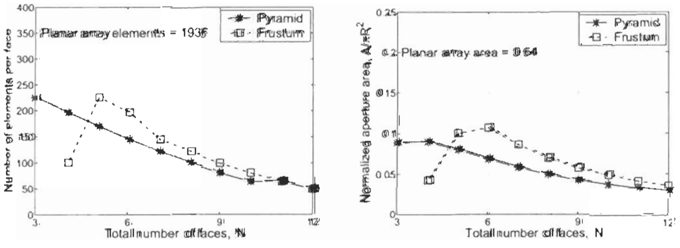

(i) Number of array elements (j) Normalized array area

Figure 5.10: Evaluation using the array factor. Square array apertures and square element grids, with the basic element spacing, are used. Two different values of footprint radius, $R = 8\lambda_0$ (top) and $R = 16\lambda_0$ (bottom). The coverage range used is $\theta \in [0°, 75°]$.

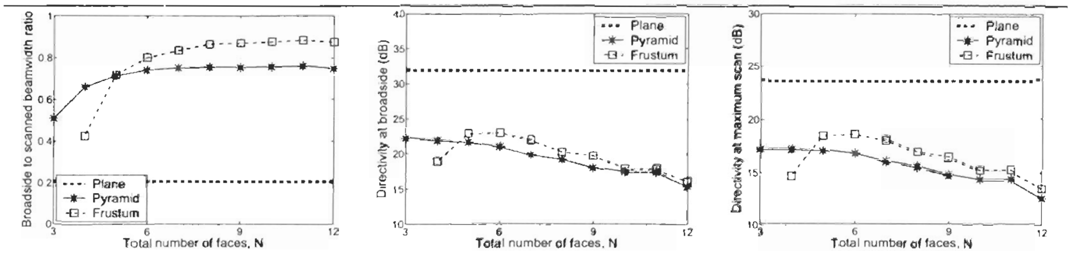

(a) Beamwidth ratio (b) Directivity at broadside (c) Directivity at maximum scan

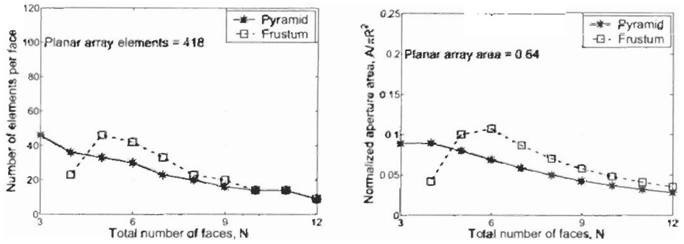

(d) Number of array elements (e) Normalized array area

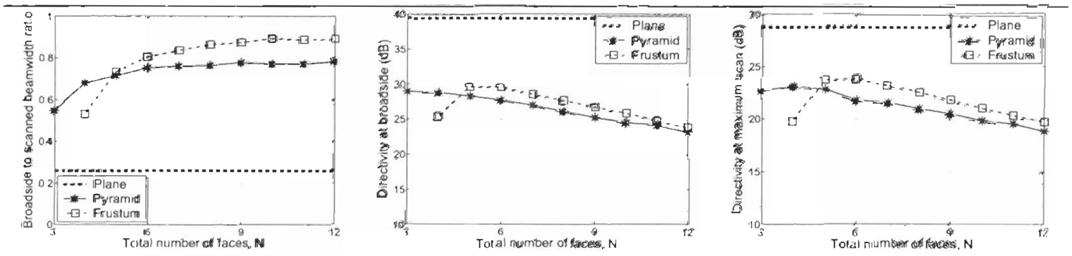

(f) Beamwidth ratio (g) Directivity at broadside (h) Directivity at maximum scan

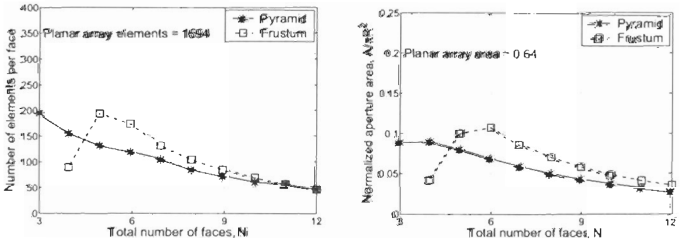

(i) Number of array elements (j) Normalized array area

Figure 5.11: Evaluation using the array factor. Square array apertures and hexagonal element grids, with the optimal element spacing, are used. Two different values of footprint radius, $R = 8\lambda_0$ (top) and $R = 16\lambda_0$ (bottom). The coverage range used is $\theta \in [0°, 75°]$.

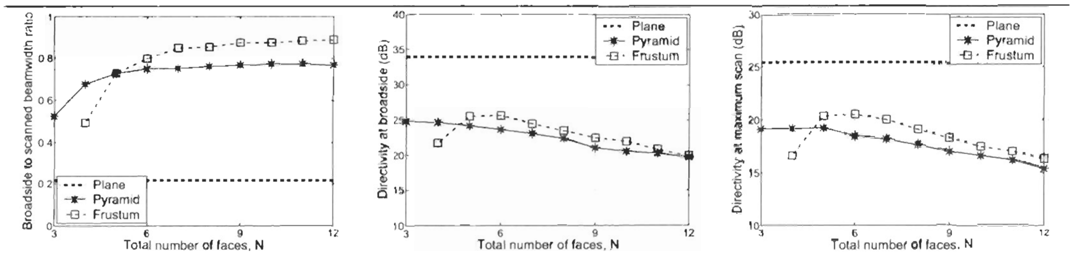

(a) Beamwidth ratio (b) Directivity at broadside (c) Directivity at maximum scan

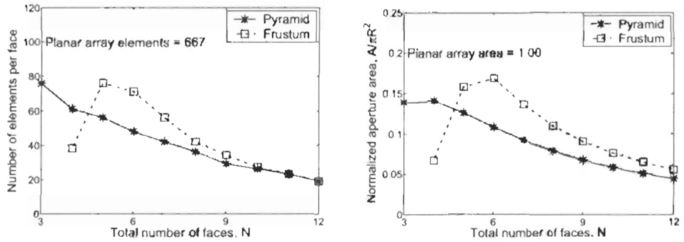

(d) Number of array elements (e) Normalized array area

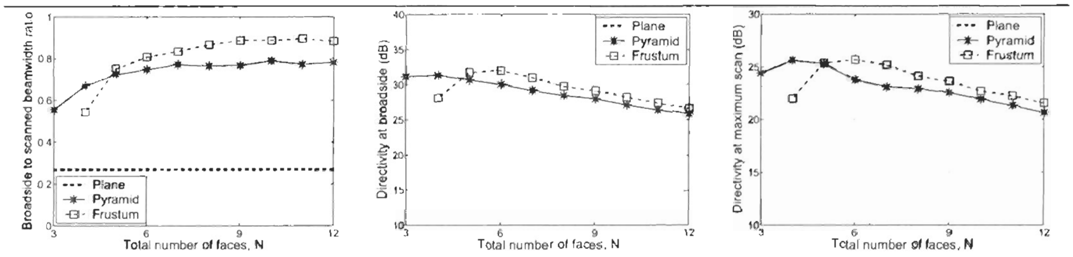

(f) Beamwidth ratio (g) Directivity at broadside (h) Directivity at maximum scan

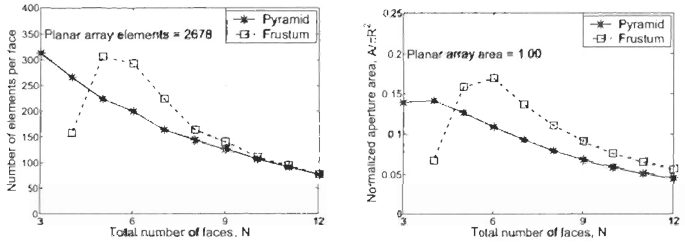

(i) Number of array elements (j) Normalized array area

Figure 5.12: Evaluation using the array factor. Circular array apertures and hexagonal element grids, with the optimal element spacing, are used. Two different values of footprint radius, $R = 8\lambda_0$ (top) and $R = 16\lambda_0$ (bottom). The coverage range used is $\theta \in [0°, 75°]$.

aperture shape and element grid. Therefore, a circular aperture with a hexagonal grid is used here. Consequently, the number of elements per aperture and the aperture areas are exactly the same as those shown in Figures 5.12(d) and 5.12(e), and 5.12(i) and 5.12(j), for the two footprint radii.

Figure 5.13 depicts the beamwidth ratio, and the directivities at broadside and maximum scan, for the two footprint radii, and using the coverage range $\theta \in [0°, 75°]$. The trends are very similar to those shown in Figure 5.12. The major difference is the large reduction in the directivity of the planar array at the maximum scan angle, about 15 dB. The reason for this sharp drop is that the far-field pattern of the patch antenna decays rapidly at large zenith angles (near the array plane) and that the single planar array needs to scan up to 75° while the multi-faceted arrays need to scan to at most 57°. In this case, the 6- or 7-face frusta are a better choice than a single planar array or any N-face pyramid.

5.2.4 Evaluation Using the Simulated Element Pattern

The final level of the evaluation framework uses the simulated array pattern, computed as the product of the simulated isolated element pattern and the array factor. Therefore, the geometric structure of each antenna, the planar array factor, and the simulated element pattern are included, but the mutual coupling is neglected. A broadside LHCP patch with a foam substrate ($\epsilon_r = 1.25$) was designed for a frequency of 1.48 GHz and the array patterns were computed using Microwave Studio®, an EM simulation software package by Computer Simulation Technology (CST).

The simulated antenna structure is similar to that shown in Figure 3.1 and the parameters used for simulation are summarized in Table 5.2. Figure 5.14 shows the far-field radiation patterns, co- and cross-polar patterns, and cuts of the co- and cross-polar patterns in the $\phi = 0°$ and $\phi = 90°$ planes, for both the modelled and simulated antenna elements. The figure shows that the θ-components of the far-field patterns and the cross-polar patterns differ slightly between the modelled and simulated elements. There is also a difference in the lobes of the cross-polar patterns. The differences are due to the fact that the simulator accounts for more structural details than the model (Refer to the model assumptions in Section 3.3.1), and therefore the effective radius of the simulated patch will be different from the ring source radius from the cavity mode.

The simulations were performed using a footprint radius $R = 8\lambda_0$, and hence the number of elements per aperture and the aperture areas are exactly the same as those shown in Figures 5.12(d) and 5.12(e), respectively. The simulation results are shown in Figure 5.15. The beamwidth ratio curves shown in Figure 5.15(a) are very similar to those obtained using the modelled element, shown in Figure 5.13(a). The broadside directivity shows a similar behavior to that in Figure 5.13(b), which was computed using the modelled element pattern.

The most interesting result is the behavior of the directivity at maximum scan curves shown in Figure 5.15(c). The figure shows an even larger drop in the planar

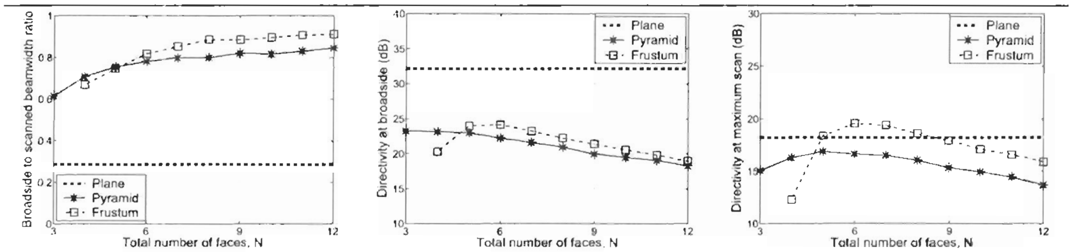

(a) Beamwidth ratio (b) Directivity at broadside (c) Directivity at maximum scan

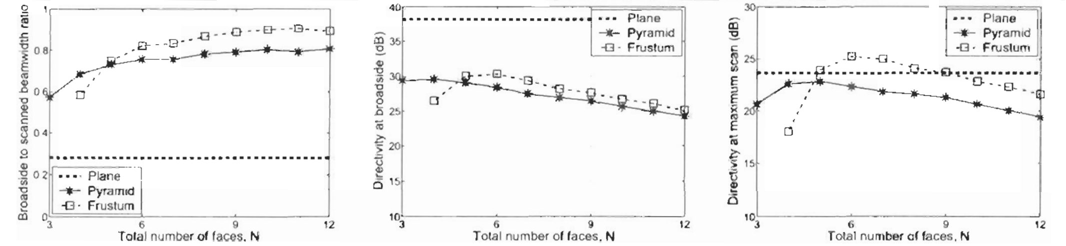

(d) Beamwidth ratio (e) Directivity at broadside (f) Directivity at maximum scan

Figure 5.13: Evaluation using the modelled pattern of the CP patch antenna element. Circular array apertures and hexagonal element grids, with the optimal element spacing, are used. Two different values of footprint radius, $R = 8\lambda_0$ (top) and $R = 16\lambda_0$ (bottom). The coverage range used is $\theta \in [0^\circ, 75^\circ]$.

array directivity (about 20 dB) than that computed using the modelled element pattern. This is due to the faster decay of the θ-component of the simulated element pattern as θ increases, as shown in Figure 5.14 (top) (Recall that the scan angle γ is measured from the broadside direction of the array, and hence the patch, i.e., θ here is equivalent to γ). Clearly, the multi-faceted antennas have a significant advantage over the single planar array, with the best performers being pyramidal frusta with 6 to 10 faces.

5.3 Results

Table 5.3 summarizes the results of all four levels of evaluation discussed in Section 5.2. The terms "small", "moderate", and "large" margins used in the table indicate differences of around 10%, between 10% and 100%, and larger than 100%, respectively. The results are based on Figures 5.1 through 5.15 which use the coverage range $\theta \in [0°, 75°]$. However, similar trends are expected to hold for other coverage ranges, with multi-faceted antenna arrays having a larger advantage over planar arrays as the coverage range becomes wider or closer to horizon. This is because all cost functions are affected by the maximum scan angle, which in turn is determined by the total

Table 5.2: Parameters of the simulated CP circular patch antenna. The patch structure is shown in Figure 3.1.

Parameter	Value
Frequency	1.48 GHz
Relative substrate permittivity	1.25
Patch radius, a	50.9 mm
Distance from feed to patch center, d	15.3 mm
Patch height, h	0.1 mm
Substrate height	1 mm
Groundplane height	3 mm
Feed conductor radius	1 mm
Feed dielectric radius	4 mm

	Modelled antenna element	Simulated antenna element
Linear scale plots of the θ- and ϕ-components of the far-field radiation pattern	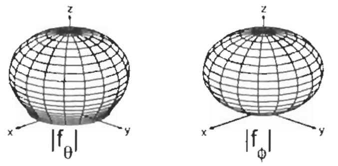	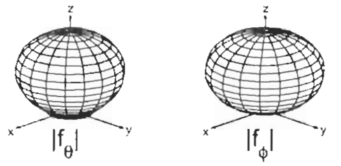
Linear scale plots of the co- and cross-polar patterns ($\lvert F_{cr} \rvert$ enlarged by a factor of 2)	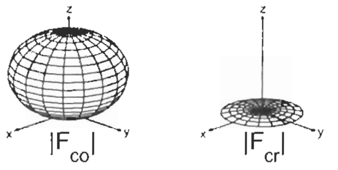	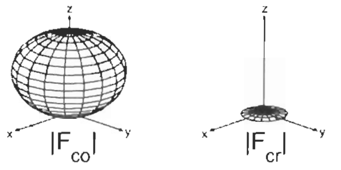
Cuts of the co- and cross-polar patterns at $\phi = 0°$ (dB scale)	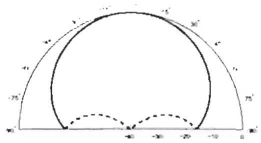	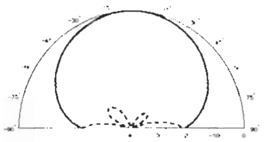
Cuts of the co- and cross-polar patterns at $\phi = 90°$ (dB scale)	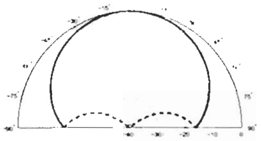	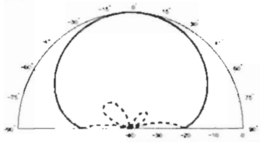

Figure 5.14: The far-field radiation patterns, the co- and cross-polar patterns, and cuts of the co- and cross-polar patterns in the $\phi = 0°$ and $\phi = 90°$ planes, for the modelled (left) and the simulated (right) antenna elements. See text for comments on the difference between the patterns of the modelled and the simulated patches.

number of array faces used, as elaborated in Section 2.6.

The comparison results with respect to the maximum scan angle and antenna dimensions apply at all levels of evaluation. This is because they are mainly affected by the geometric structure of the antenna. The beamwidth broadening results appear to remain more or less unchanged (especially using large arrays), regardless of the level of evaluation. The planar array always has the largest directivity at broadside regardless of the level of evaluation, owing to its larger aperture area and number of elements for a given antenna footprint.

Planar arrays also seem to have an advantage, in terms of the directivity at the maximum scan angle (minimum directivity), when considering the geometric structure

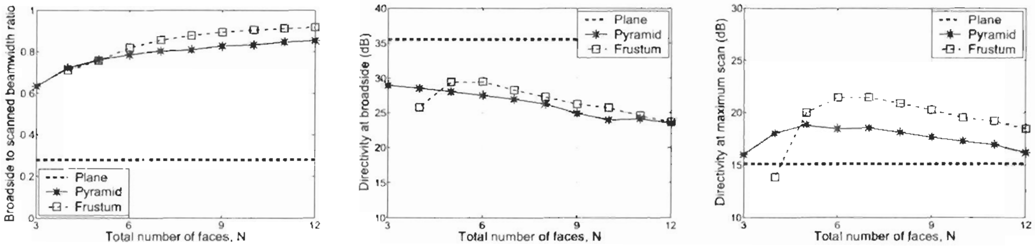

(a) Beamwidth ratio (b) Directivity at broadside (c) Directivity at maximum scan

Figure 5.15: Evaluation using the simulated pattern of the CP patch antenna element. Circular array apertures and hexagonal element grids, with the optimal element spacing, are used. The footprint radius used is $R = 8\lambda_0$ and the coverage range is $\theta \in [0°, 75°]$.

and the array factor. However, once the element pattern is included, the advantage of using multi-faceted antennas becomes more pronounced. In fact, when the evaluation is performed using the simulated element pattern (which is a more realistic scenario that better resembles the working antenna), the advantage of using pyramidal or pyramidal frustum antenna arrays is significant.

The multi-faceted antenna arrays are also better than planar arrays in the sense that they require a smaller total number of elements to achieve a better minimum directivity, for a given antenna footprint. Moreover, the scan loss model and the method used for computing the element spacing seem to have little impact on the number of elements required, as shown in Figure 5.9. Finally, the aperture shape and the element grid type appear to have a very minor influence on the results obtained using all of the cost functions.

5.4 Summary

This chapter presented the performance evaluation and comparison framework developed here to compare the different array structures. Unlike previously reported evaluation methods, this framework:

Table 5.3: A summary of the performance evaluation results.

Cost function	Optimal structure(s)
Evaluation based on geometric design	
Maximum scan angle	Frusta with N=6 to 10, followed by pyramids with N=4 to 7 by a moderate margin, then the planar array by a large margin.
Beamwidth broadening	Frusta with N=6 to 10, followed by pyramids with N=4 to 7 by a small margin, then the planar array by a large margin.
Antenna dimensions†	• Height: planar arrays, followed by pyramids and frusta by a large margin. The larger the number of faces the better. • Physical aperture area: planar arrays, followed by frusta with N=5 to 7 and pyramids with N=3 to 5 by a large margin. • Minimum projected aperture area: planar array by a moderate margin, followed by frusta with N=5 to 7 and pyramids with N=3 to 6.
Broadside geometric directivity†	Planar arrays by a large margin, followed by frusta with N=5 to 7 and pyramids with N=3 to 5.
Minimum geometric directivity†	Planar arrays by a moderate margin, followed by frusta with N=5 to 7, then pyramids with N=3 to 6.
Scan loss	Frusta with N=6 to 8, followed closely (within 1dB) by pyramids with N=4 to 5. Both are better than the planar array by a large margin.
Total number of elements	• Equal gain at maximum scan: pyramids with N=4 to 5 and frusta with N=5 to 7 are very similar, followed by planar arrays by a moderate margin. • Equal scan plane beamwidth at maximum scan: pyramids with N=4 to 5 and frusta with N=5 to 9 are very similar, followed by planar arrays by a large margin.
Evaluation using the array factor	
Beamwidth broadening	Frusta with N=6 to 10, followed by pyramids with N=4 to 7 by a small margin, then the planar array by a large margin.
Broadside directivity†	Planar arrays by a large margin, followed by frusta with N=5 to 7 and pyramids with N=3 to 5.
Minimum directivity†	Planar arrays by a moderate margin, followed by frusta with N=5 to 7, then pyramids with N=3 to 6.
Total number of elements†	Pyramids with N=3 to 7, followed by frusta with N=4 to 8 by a small margin, then planar arrays by moderate margin.

† Given a constant antenna footprint.

Table 5.3: A summary of the performance evaluation results (continued).

Cost function	Optimal structure(s)
Evaluation using the modelled element pattern	
Beamwidth broadening	Similar results as those found using the array factor only.
Directivity at broadside†	Similar results as those found using the array factor only.
Minimum directivity†	Frusta with N=5 to 8, followed by planar arrays with a small margin, then pyramids with N=4 to 8 by a moderate margin.
Total number of elements†	Exact same results as those found using the array factor.
Evaluation using the simulated element pattern	
Beamwidth broadening	Similar results as those found using the array factor only.
Directivity at broadside†	Similar results as those found using the array factor only.
Minimum directivity†	Frusta with N=5 to 9, followed by pyramids with N=4 to 8 by a moderate margin, then planar arrays by a moderate margin.
Total number of elements†	Exact same results as those found using the array factor.

† Given a constant antenna footprint.

- Compares N-face pyramidal, N-face pyramidal frustum, and planar array structures.
- Evaluates the three structures at four different levels of detail, first using only the geometric structure, then incorporating the isotropic array factor, and finally including both the modelled and the simulated element patterns.

The patch antenna was used as the antenna element, and owing to its wide use, the results presented here should be useful for a wide range of practical designs.

The results demonstrate how the multi-faceted antennas have a clear advantage over planar arrays. Once the element pattern is considered in the evaluation, as will be done when designing a working antenna, this advantage becomes clearly significant. Moreover, although only a few coverage ranges were used for comparison using the different cost functions, similar trends are expected to hold for other coverage ranges, with multi-faceted antenna arrays showing a larger advantage over planar arrays as the coverage range becomes wider and/or closer to horizon. For narrow coverage ranges that are close to zenith or when high scan losses can be tolerated, it is sufficient to use planar arrays. Although these qualitative conclusions seem intuitive, the results presented here provide quantitative guidelines that can be used by the antenna designer.

The results also show that no clear improvement is gained by using more than about 10 array faces, given the added area, cost, and complexity involved. Also, under most circumstances, there is no significant difference in performance between pyramids and pyramidal frusta with a moderate number of faces (N=4 to 7 for pyramid, and 5 to 9 for pyramidal frusta). However, the design curves presented here will help the antenna designer select the number of faces based on the cost functions that are most relevant for the underlying application.

Chapter 6

Conclusion

This chapter summarizes the material presented in this thesis. It also outlines the contributions of the conducted research work and summarizes the conclusions that can be drawn from them.

6.1 Summary

This work involved the modelling and design of multi-faceted antenna arrays for providing general hemispherical scan coverage. Two classes of multi-faceted antenna arrays were used, namely, pyramids and pyramidal frusta, and four stages of their design process were considered. A review of related previous work in each of the four stages was presented in the respective chapters.

The first stage dealt with the geometric design of the antenna. The optimal antenna geometry, in terms of the face elevation for a given number of faces, was determined subject to minimizing the maximum scan angle encountered by the individual face arrays. The second stage focused on the design of the circularly polarized circular patch antenna, chosen here as the array element. The polarization purity of the antenna was examined over different angular intervals which are related to the coverage areas of the individual array faces. The third stage dealt with the design of the individual antenna array, which is supported by each of the antenna faces. Key array parameters including the element grid, spacing, and excitation, and aperture shape, were selected based on the special requirements of the multi-faceted antenna arrays. The final stage involved the evaluation of the estimated performance of multi-faceted antenna arrays, and a comparison between them and planar arrays, using widely applicable cost functions.

6.2 Contributions and Conclusions

The research work presented here resulted in many contributions to the area of multi-faceted antenna design. The contributions in the geometric design stage include:

- Simple equalization-based and novel minimax-based methods to determine the optimal face elevation of pyramids and pyramidal frusta given a general hemispherical scan coverage requirement.
- An investigation of the impact of far-field approximation on the maximum scan angle when the optimal geometry is used.
- An investigation of the impact of the total number of array faces on the maximum scan angle.

The results demonstrated that increasing the number of faces of pyramids beyond 7, or pyramidal frusta beyond 10, brings only diminished returns to reducing the maximum scan angle. The results also showed that the maximum scan angle increases only slightly at distances equal to or larger than the far-field approximation, $10D^2/\lambda$, typically used for far-field pattern measurement.

In the circular patch antenna design stage, an investigation of the antenna circular polarization purity, over angular sectors about the antenna broadside, was performed. The investigation showed that:

- There is a well-defined optimal patch size for each mode which produces extremely pure polarization. For the broadside radiation mode, this corresponds to patch radii around $\lambda/4$ and a substrate relative permittivity of about 1.25.

- The effect of amplitude tolerance is less severe than that of phase shift or feed position tolerances. However, the presence of any tolerance reduces the polarization purity of the patch.

A comparison with experimental patch antenna designs demonstrate that the numerical results serve as upper bounds for the polarization purity of patch antennas on a large ground plane. These results are not only relevant to multi-faceted antennas but also to a wider variety of wireless and mobile communication applications that use circular polarization.

In the planar antenna array design stage, an assessment was presented of the improvement gained by computing the element spacing, such that the special coverage extent of the array faces is utilized. A comparison with the basic method typically used to determine the element spacing showed an improvement of only a few percent. This improvement, although minor, can compensate for some or all of the spacing reduction needed to avoid array blindness.

Finally, the performance evaluation framework compared planar, pyramidal, and pyramidal frustum antenna arrays. Four different levels of evaluation were performed: using the geometric structure alone; then incorporating the isotropic array factor; and finally including both the modelled; and the simulated element patterns. The results demonstrated that the performance advantages of multi-faceted antenna arrays over planar arrays increase as the coverage range becomes wider and/or closer to horizon, while planar arrays are sufficient for narrow coverage ranges that are close to zenith. These advantages become even more significant once the radiation characteristics of the antenna element are considered. The results also show that no clear improvement is gained by using more than about 10 array faces, given the added area, cost, and complexity involved. Moreover, under most circumstances, there is no significant difference in performance among pyramids with 4 to 7 faces or among pyramidal frusta with 5 to 9 faces.

Appendix A

Antennas and Antenna Arrays

This appendix provides a brief overview of important concepts in the theory of antennas and antenna arrays. These concepts are frequently referred to in Chapters 2 through 5.

A.1 Antennas, Waves, and Polarization

An antenna is the part of a wireless communication system that radiates or receives electromagnetic waves. A transmitting antenna converts electrical power into radiated electromagnetic energy, whereas a receiving antenna collects energy and converts it to electrical power [Wright, 1987]. An antenna is typically required to operate over a relatively narrow frequency band, described by its free-space center frequency, f_0, and bandwidth. Efficient transmission or reception is achieved by tuning the antenna characteristics to that frequency band.

Electromagnetic Waves

Electromagnetic waves are composed of coexistent, time-varying, electric and magnetic fields which are related through Maxwell's equations. An electromagnetic wave is characterized by its frequency of oscillation, intensity, direction of propagation, and polarization. A transverse electromagnetic wave is one in which the electric field vector, **E**, and the magnetic field vector, **H**, are perpendicular to each other and are confined in a plane that is perpendicular to the direction of wave propagation. The phase front, which is the surface of constant phase, of a wave depends on the shape and extent of the wave source. Although all sources have finite dimensions, the phase fronts at sufficiently large distances from the source are spheres, i.e. finite sources radiate spherical waves. Moreover, such large spherical phase fronts can be approximated by planes, giving rise to plane waves [Stutzman, 1993]. The instantaneous electric and magnetic fields of a plane wave traveling in the positive z direction can be expressed as [Balanis, 1989]:

$$\begin{aligned}
\mathbf{E} &= \mathbf{E}(t,z) \\
&= E_x\hat{x} + E_y\hat{y} \\
&= E_{x0}\cos(\omega t - kz + \delta_x)\hat{x} + E_{y0}\cos(\omega t - kz + \delta_y)\hat{y}, \\
\mathbf{H} &= \mathbf{H}(t,z) \\
&= H_x\hat{x} + H_y\hat{y} \\
&= -\tfrac{E_{y0}}{\eta}\cos(\omega t - kz + \delta_y)\hat{x} + \tfrac{E_{x0}}{\eta}\cos(\omega t - kz + \delta_x)\hat{y},
\end{aligned} \tag{A.1}$$

where $\hat{x}$ and $\hat{y}$ are unit vectors along the x and y directions, E_{x0} and E_{y0} are the amplitudes of **E** in the x and y directions, $\omega = 2\pi f$ is the radian frequency of the wave, $k = \frac{2\pi}{\lambda}$ is the wave number, λ is the wavelength, and δ_x and δ_y are the initial phases of the x and y components of **E**. $\eta = \sqrt{\mu/\epsilon}$ is the intrinsic impedance of the medium where the wave is traveling, where ϵ is the medium permittivity and μ is the medium permeability. The intrinsic impedance of free space, η_0, is equal to 120π or 377Ω.

Polarization

The polarization of an antenna is that of the plane wave transmitted by that antenna. The polarization of a field vector, associated with a wave, describes the behavior of that field at a fixed point in space as a function of time, in terms of shape (linear, circular, or elliptical), orientation (or tilt), and rotation sense (right- or left-handed) of the extremity of the field [IEEE, 1983]. Polarization is typically associated with the electric field vector, **E**, which can be decomposed into two orthogonal components, as shown in Equation A.1.

A wave is linearly polarized (LP) if **E** is always oriented along a straight line at every instance of time at a fixed point in space. This occurs when either of the components E_x or E_y vanishes, or if both components exist and are in phase or 180° out of phase. The former case yields horizontal or vertical polarization, while the later yields linear polarization with a tilt angle $\psi = \tan^{-1}(E_{y0}/E_{x0})$. Circular polarization (CP), on the other hand, requires that the two components of **E** have equal amplitudes and be in phase quadrature. The sense of polarization is determined by viewing the polarization plane, which is the plane containing **E**, with the wave direction approaching the observer. At a fixed point in space, if the tip of **E** rotates counterclockwise as a function of time, the wave is right-hand polarized. Alternatively, if the tip of **E** rotates clockwise, the wave is left-hand polarized [Stutzman, 1993]. Both linear and circular polarizations are generalizations of elliptical polarization (EP), where the tip of **E** traces an ellipse whose major axis may be tilted by an angle ψ from the x axis.

It is important that the transmit and receive antennas in a communication system use the same polarization. A mismatch in polarization shape, orientation, or sense of rotation, between the two antennas typically causes significant degradation of the signal. For example, an orientation mismatch of 45° between two linear polarizations, or a shape mismatch (e.g. linear and circular), may cause degradations of up to 3 dB. Using circular polarizations with opposite senses of rotation causes similar or more severe losses. The wanted, or reference, polarization is referred to as the *co-polarization*, while the polarization orthogonal to it is called *cross-polarization*. For example, if right-hand circular polarization (RHCP) is the intended polarization of an antenna, the cross-polarization is the left-hand circular polarization (LHCP).

A.2 Radiation Pattern Representation

The radiation pattern of an antenna describes the relative intensity of the field radiated from a transmit antenna, or collected by a receive antenna, at different directions in space and at a constant distance from the antenna. It is typically represented using the spherical coordinate system. The radiation pattern, $F(\theta, \phi)$, at a point $p = (x, y, z)$ in space is a function of the direction (θ, ϕ) of p with respect to the antenna. The relationship between Cartesian and spherical coordinates is illustrated in Figure A.1 and is given by:

$$\begin{aligned} x &= r \sin\theta \cos\phi & \qquad r &= \sqrt{x^2 + y^2 + z^2} \\ y &= r \sin\theta \sin\phi & \qquad \theta &= \tan^{-1} \sqrt{x^2 + y^2}/z \\ z &= r \cos\theta & \qquad \phi &= \tan^{-1} y/x \end{aligned} \tag{A.2}$$

The far-field radiation pattern is the pattern measured at large distances from the antenna, as opposed to the near-field radiation pattern. The far-field distance, $r_{\min}$, which is the transition between the near and far fields of an antenna, is given by:

$$r_{\min} = \frac{2D^2}{\lambda}, \tag{A.3}$$

where D is the largest dimension of that antenna.

The radiation pattern may be represented graphically in a variety of ways. To illustrate such representation, consider the isotropic antenna. It is a hypothetical antenna that radiates, or receives, equally in all directions in space. In other words, its radiation pattern is given by:

$$F(\theta, \phi) = 1, \text{ for } \theta \in (0, \pi) \text{ and } \phi \in (0, 2\pi). \tag{A.4}$$

Possible graphical representations include three-dimensional spherical plots, and two dimensional polar and rectangular plots. Either linear or logarithmic (dB) scales

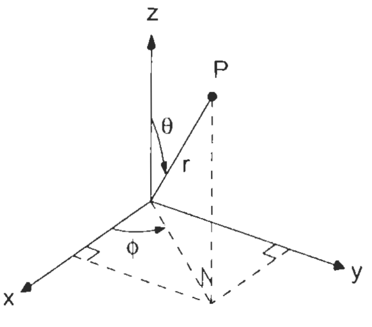

Figure A.1: Illustration of the relationship between the Cartesian coordinates, (x, y, z) and the spherical coordinates, (r, θ, ϕ).

can be used for each of the three types of plots. Figure A.2(a) shows a linear-scale spherical plot of $F(\theta, \phi)$, which is perfectly spherical. Figure A.2(b) shows a dB-scale polar plot of F versus θ in the $\phi = 0°$ plane. This is also referred to as a pattern *cut* in that plane. Finally, Figure A.2(c) shows a linear-scale rectangular plot of F versus θ in the $\phi = 0°$ plane.

A.3 Impedance, Impedance Matching, and Bandwidth

A lossless antenna is a circuit element that may be characterized by a self-impedance of the form:

$$Z_A = R_A + jX_A. \tag{A.5}$$

The self-impedance depends on the antenna shape and dimensions, as well as the frequency of operation. The radiation resistance, R_{rad} is the real part of the self-impedance, i.e. $R_{\text{rad}} = \text{Re}[Z] = R_A$. It is a hypothetical quantity that represents the power radiated by the antenna. In other words, if a resistance R_{rad} is inserted in place of the antenna, it would consume the same amount of power as that radiated by the antenna. In practice, some of the total power fed to an antenna is dissipated

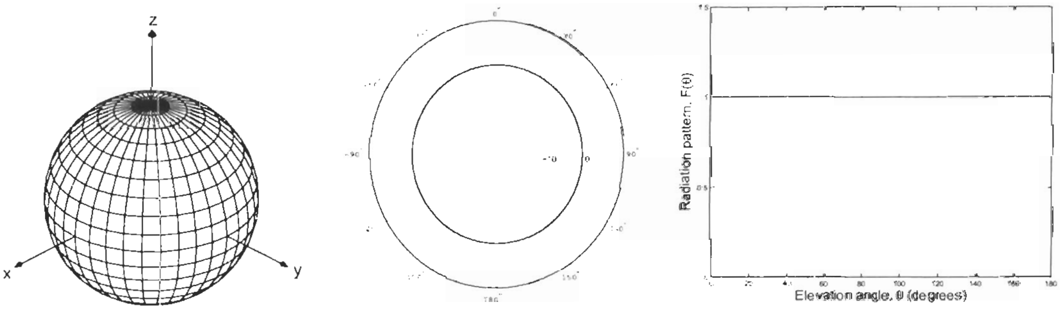

(a) Spherical plot (b) Polar plot (c) Rectangular plot

Figure A.2: Examples of the graphical representations of the radiation pattern of an isotropic antenna: (a) spherical plot, (b) polar plot, and (c) rectangular plot.

through ohmic and leakage resistances, which represent losses in the antenna and the dielectric materials, respectively [Carr, 1998].

For efficient transfer of energy from the voltage source to the antenna, the impedance of the transmission line feeding the antenna must be matched to that of the antenna. This is done by minimizing the voltage reflection coefficient defined as:

$$\Gamma = \frac{Z_A - Z_0}{Z_A + Z_0}, \tag{A.6}$$

where Z_0 is the characteristic impedance of the transmission line (typically 50 Ω). Impedance matching is, therefore, achieved when $Z_A = Z_0$.

Impedance mismatch mixes the reflected wave with the incident wave and a standing wave is formed. The voltage standing wave ratio (VSWR) is defined as the ratio of the maximum to the minimum standing wave voltage, i.e.,

$$VSWR = \frac{V_{\max}}{V_{\min}} = \frac{1 + |\Gamma|}{1 - |\Gamma|}. \tag{A.7}$$

The bandwidth of an antenna refers to the range of frequencies over which the antenna can operate correctly. This may be taken as the range where the VSWR exhibited by the antenna is less than 2. Alternatively, it may be defined by the frequency limits at which the antenna gain is reduced to half power [Mailloux, 1994].

A.4 Directivity and Gain

The antenna design goal is to find an arrangement of sources such that the radiation pattern $F(\theta, \varphi)$ is enhanced in certain directions while it is suppressed in all other directions [Elliott, 2003]. This is measured by the Directivity. Directivity in a certain direction (θ, ϕ) is the ratio of the radiated power density in that direction to the average radiated power density over all possible directions, i.e.,

$$D(\theta, \phi) = \frac{|F(\theta, \phi)|^2}{\frac{1}{4\pi} \int_0^{2\pi} \int_0^{\pi} |F(\theta', \phi')|^2 \sin\theta' d\theta' d\phi'}. \tag{A.8}$$

The term directivity is typically used to refer to peak directivity. Peak directivity is defined in a single direction (θ_0, ϕ_0) which corresponds to the direction of maximum radiated power. Therefore,

$$D(\theta_0, \phi_0) = \max_{\theta,\phi}(D(\theta, \phi)). \tag{A.9}$$

By definition, the power lost in the antenna itself is not included in the directivity. Instead, it is included in the gain, G, given by [Elliott, 2003]:

$$G(\theta, \phi) = \frac{D(\theta, \phi)}{K_L}, \tag{A.10}$$

where K_L is a real constant greater than unity that is specific to the antenna material. Thus, gain is always $10 \log_{10} K_L$ dB less than directivity.

A.5 Antenna Arrays

An antenna array is composed of multiple antenna elements. Antenna arrays provide a versatile alternative to fixed-aperture antennas, such as reflectors, since their radiation pattern can be easily shaped by manipulating the element excitation. Pattern shaping refers to controlling features of the radiation pattern such as main beam width, main beam direction, sidelobe level, or number of pattern nulls, In antenna arrays, this is accomplished by varying: (a) the relative amplitude and/or phase of the excitation of each element in the array, (b) the number of antenna elements, and/or (c) the inter-element spacing.

When all elements of the antenna array are identical, the far-field radiation pattern of the array, $F(\theta, \phi)$, is given by the product of the isotropic array factor, $F_A(\theta, \phi)$, and the individual element pattern, $F_E(\theta, \phi)$, i.e.,

$$F(\theta, \phi) = F_A(\theta, \phi) F_E(\theta, \phi). \tag{A.11}$$

The isotropic array factor (or simply the *array factor*) is the radiation pattern of an array of isotropic elements. It is simply the discrete Fourier transform of the array excitation. Therefore, it is a function of the relative excitation and relative element position. On the other hand, the element pattern is a function of its current distribution which is in turn a function of its shape and dimensions.

A.5.1 Linear Antenna Arrays

A linear antenna array is an array where all elements lie along a straight line, called the *array axis*. Without loss of generality, the array axis may be aligned with the z-axis. Figure A.3 depicts the array axis and the layout of antenna elements in a linear array composed of 4 elements. Antenna elements, shown as filled circles, are uniformly-spaced by a distance d. The isotropic array factor of a uniformly-spaced N-element linear antenna array is given by [Rulf and Robertshaw, 1987]:

$$F_A(\theta) = \sum_n a_n e^{jnkd\cos\theta}, \qquad n = 0, 1, \ldots, (N-1), \tag{A.12}$$

where $k = \frac{2\pi}{\lambda}$, d is the element spacing, and a_n is the relative excitation, or *weight*, of the nth element. It is obvious that F_A is not a function of ϕ. Equation A.12 can be rewritten in terms of the angular variable $u = \cos\theta$, i.e.

$$F_A(u) = \sum_n a_n e^{jnkdu}, \qquad n = 0, 1, \ldots, (N-1). \tag{A.13}$$

Figures A.4(a) and A.4(b) show rectangular plots of the array factor in dB scale, i.e. $20\log_{10}|F_A(.)|$, versus θ and u, respectively, for different values of N and an element spacing of $\frac{\lambda}{2}$. The array factor has a single global maximum at *broadside*, which is the direction perpendicular to the array axis, i.e. $\theta = 90°$. The part of the radiation pattern between the two nulls around this maximum is referred to as the

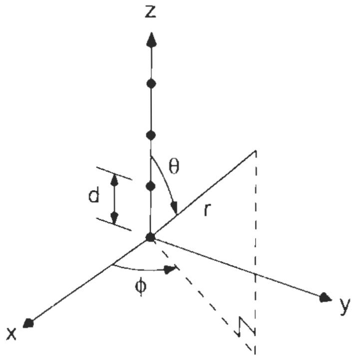

Figure A.3: The layout of elements in a uniform linear antenna arrays with $N = 4$.

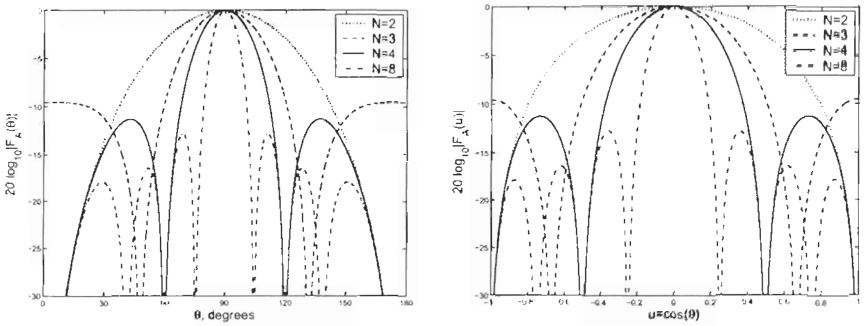

(a) $20\log_{10}|F_A(\theta)|$ vs. θ (b) $20\log_{10}|F_A(u)|$ vs. u

Figure A.4: Rectangular plots (dB scale) of the isotropic array factors of linear antenna arrays with $N = 2, 3, 4, 8$ elements and $d = \frac{\lambda}{2}$.

main beam. The other maxima of $F_A(.)$ are called *side lobes*. Note how the nulls of $F_A(u)$ are equally spaced in the u-parameter space.

Figure A.5(a) shows a linear-scale polar plot of the array factor of a linear array with 8 elements and an element spacing of $\frac{\lambda}{2}$. The figure shows the main beam which is perpendicular to the antenna array axis (the z axis), as well as the side lobes. Since $F_A(\theta)$ is independent of ϕ, then the spherical plot is simply obtained by rotating the array factor about the z-axis. The spherical plot is shown in Figure A.5(b).

It is worth noting that some authors, e.g. [Mailloux, 1994], orient the array axis such that it is perpendicular to the z-axis. However, aligning the array axis with the z-axis, e.g. [Rulf and Robertshaw, 1987], simplifies the visualization of the array factor, as shown in Figure A.5. It also allows utilizing the ϕ-independence of the array factor when computing quantities such as the directivity, as will be shown below.

Beam Scanning

The main beam of the array factor can be pointed in directions other than broadside ($\theta = 90°$), by adding a linearly increasing, or *progressive*, phase shift to the excitation of the individual array elements. This operation is referred to as *scanning* and the resulting main beam is called a scanned beam. More specifically, it is said that

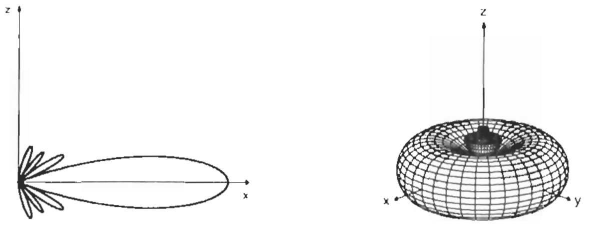

(a) Polar plot (b) Spherical plot

Figure A.5: Linear-scale polar and spherical plots of the isotropic array factor of a linear antenna array with $N = 8$ and $d = \frac{\lambda}{2}$. The spherical plot is obtained by rotating the polar plot about the z-axis.

the beam is *electronically* scanned, since the beam is scanned by simply changing the element excitation, as opposed to mechanically changing the element position or orientation.

To scan the main beam to a direction θ_0, a phase shift of $nkd\cos\theta_0$ is applied to element n, where $n = 0, 1, \ldots, N-1$. Therefore, Equations A.12 and A.13 become:

$$\begin{aligned} F_A(\theta) &= \sum_n a_n e^{jnkd(\cos\theta - \cos\theta_0)}, & 0 \leqslant n \leqslant N-1, \\ F_A(u) &= \sum_n a_n e^{jnkd(u - u_0)}, & 0 \leqslant n \leqslant N-1, \end{aligned} \tag{A.14}$$

where $u_0 = \cos\theta_0$. It is evident from Equation A.14 that the global maximum of $F_A(.)$ occurs when $\theta = \theta_0$, or equivalently $u = u_0$. Therefore, the direction of the main beam becomes $\theta = \theta_0$, as opposed to $\theta = 90°$. When θ_0 is set along the array axis, i.e. 0° or 180°, the array is said to be scanned to *endfire*.

Figure A.6 (top) shows linear-scale polar plots of the array factor of a 16-element array with an element spacing of $\frac{\lambda}{4}$ at broadside ($\theta_0 = 90°$), a scan angle of $\theta_0 = 60°$, and endfire ($\theta_0 = 0°$), respectively. At a scan angle of $\theta_0 = 60°$, the main beam is at a 60° angle from the array axis, whereas at endfire, the main beam coincides with the array axis. Also, as the beam is scanned away from broadside, some of the side lobes between the main beam and the array axis disappear (from the visible space, $0 \leqslant \theta \leqslant \pi$), while side lobes on the other side of the main beam start to appear. The spherical plots, Figure A.6 (bottom), are obtained by rotating the polar plots about

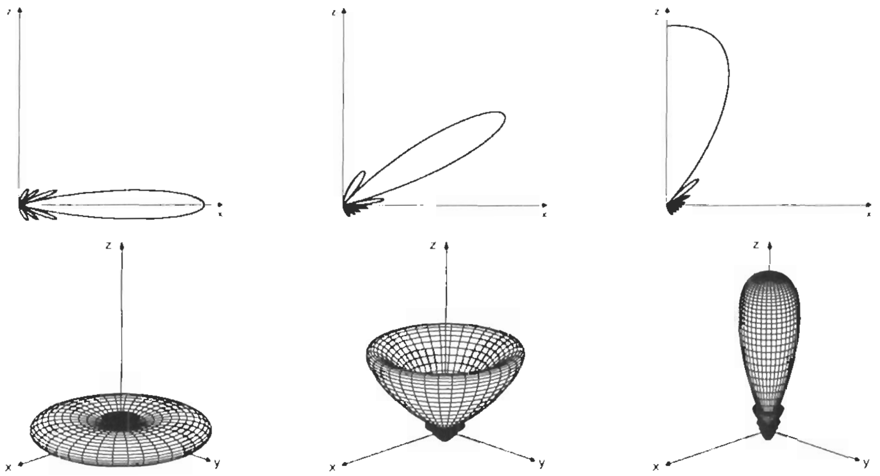

(a) Broadside (b) Scanned (c) Endfire

Figure A.6: Linear-scale polar plots (top) and spherical plots (bottom) of the array factor of a linear antenna array with $N = 16$ and $d = \frac{\lambda}{4}$ at (a) broadside ($\theta_0 = 90°$), (b) a scan angle $\theta_0 = 60°$, and (c) endfire ($\theta_0 = 0°$).

the z axis. The main beams at broadside and endfire are typically termed *fan beam* and *pencil beam*, respectively, which can be seen from the figure.

Figure A.7 shows rectangular plots of the array factors, corresponding to Figure A.6, in dB-scale versus θ and u. The figure shows how some side lobes disappear while others appear, as a result of scanning. Moreover, it shows that beam scanning is equivalent to a linear shift of $F_A(u)$ in the u-parameter space.

Grating Lobes

All of the array factors presented so far exhibited a single main beam. The main beam is formed when the contribution from each antenna element in the array is maximum. Using Equation A.14, maxima of the array factor occur when the argument of the

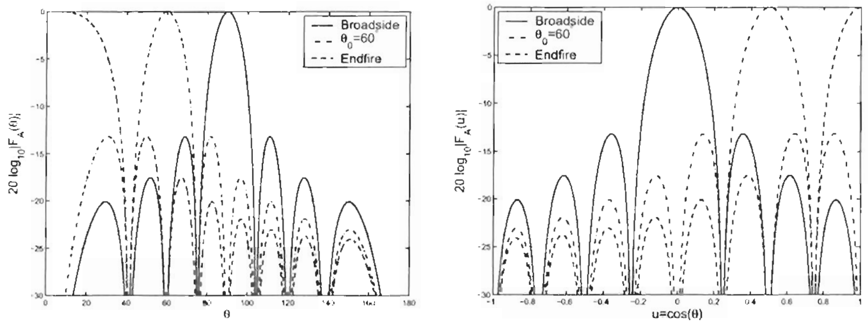

(a) $20\log_{10}|F_A(\theta)|$ vs. θ (b) $20\log_{10}|F_A(u)|$ vs. $u = \cos\theta$

Figure A.7: Rectangular plot of the array factor of a 16-element linear antenna array with $d = \frac{\lambda}{4}$ at different scan angles.

exponential term $e^{jnkd(\cos\theta - \cos\theta_0)}$ is a multiple of 2π, i.e.

$$\begin{aligned}
e^{jnkd(\cos\theta - \cos\theta_0)} &= 1, & 0 \leqslant n \leqslant N-1 \\
kd(\cos\theta - \cos\theta_0) &= 2\pi p, & p = 0, \pm1, \pm2, \ldots \\
\tfrac{2\pi}{\lambda}d(\cos\theta - \cos\theta_0) &= 2\pi p, & \\
\cos\theta - \cos\theta_0 &= p\tfrac{\lambda}{d}, & \\
\cos\theta &= \cos\theta_0 + p\tfrac{\lambda}{d}. &
\end{aligned} \tag{A.15}$$

The main beam is thus formed in the direction θ that satisfies Equation A.15 when $p = 0$. Additional main beams, called *grating lobes*, will be formed in other directions θ when $p \neq 0$, provided that they are in the visible space, $0° \leqslant \theta \leqslant 180°$.

Grating lobes, therefore, may be formed as the beam is scanned away from broadside and/or the element spacing is increased. For example, consider an 8-element linear antenna array; when the main beam is at broadside ($\theta_0 = 90°$), two grating lobes (GL) will appear at $\theta = 0°$ and $\theta = 180°$, when the elements are spaced by $d = \lambda$. This can be seen from Figure A.8(a), which depicts the array factor, $F_A(\theta)$. Alternatively, using a smaller spacing of $d = 3\lambda/4$, a single grating lobe will form at $\theta = 146.4°$ when the beam is scanned 30° away from broadside ($\theta_0 = 60°$), as shown in Figure A.8(b).

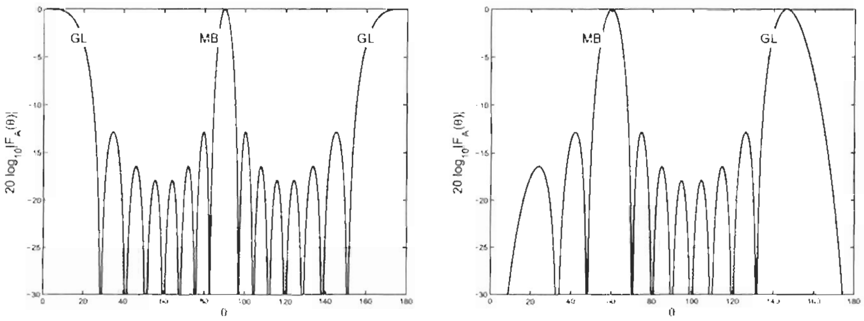

(a) $d = \lambda$, $\theta_0 = 90°$ (b) $d = 3\lambda/4$, $\theta_0 = 60°$

Figure A.8: The formation of grating lobes in an 8-element linear array factor (a) by increasing the element spacing, and (b) by scanning the main beam away from broadside. MB and GL denote main beam and grating lobe, respectively.

Directivity

The directivity of the array factor of a linear antenna array can be computed using Equation A.8, by substituting $F_A(\theta, \phi)$ for $F(\theta, \phi)$. The directivity in a direction (θ_0, ϕ_0) is thus given by:

$$D(\theta_0, \phi_0) = \frac{4\pi |F_A(\theta_0, \phi_0)|^2}{\int_0^{2\pi} \int_0^{\pi} |F_A(\theta, \phi)|^2 \sin\theta d\theta d\phi}. \tag{A.16}$$

However, since the array factor of a linear antenna array is independent of ϕ, Equation A.16 reduces to:

$$D(\theta_0) = \frac{2|F_A(\theta_0)|^2}{\int_0^{\pi} |F_A(\theta)|^2 \sin\theta d\theta}. \tag{A.17}$$

Figure A.9(a) shows how the array factor directivity (dB scale) varies with the normalized element spacing, d/λ, at different values of the number of array elements, N. The main beam is not scanned, i.e. $\theta_0 = 90°$, and the directivity is computed in the broadside direction. The figure indicates that at a constant N, directivity increases as d increases, then it drops abruptly due to the appearance of the first grating lobe. Also, the element spacing at which the maximum directivity occurs, increases as N increases. For example, for a 2-element array, maximum directivity occurs at $d/\lambda \approx 0.72$, while it occurs at $d/\lambda \approx 0.9$ in an 8-element array.

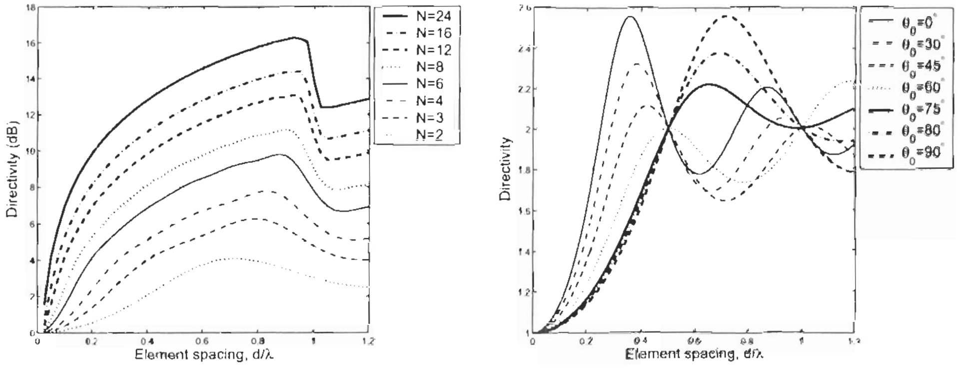

(a) (b)

Figure A.9: Directivity of the linear array factor vs. the normalized element spacing (d/λ) for different values of (a) the number of elements of broadside arrays, and (b) the scan angle for a 2-element array.

Figure A.9(b) shows the effect of scanning on directivity. In this figure, N is set to 2, and directivity is computed in the scan direction, θ_0, and plotted in linear scale. It is obvious that directivity changes as the main beam is scanned. However, directivity is constant and equal to N at element spacings that are multiples of $\frac{\lambda}{2}$, regardless of the scan angle. Moreover, the element spacing at which maximum directivity occurs decreases as the main beam is scanned away from broadside. For example, maximum directivity occurs at $d/\lambda \approx 0.72$ when the beam is at broadside, whereas it occurs at $d/\lambda \approx 0.37$ when the beam is scanned to endfire.

Beamwidth

The beamwidth of a linear antenna array is the distance between the half-power points of its far-field pattern. For a broadside array of isotropic elements, the half-power point occurs in a direction $\theta_{3\text{dB}}$ where the magnitude of the array factor, $|F_A(\theta_{3\text{dB}})|$, is 3 dB lower than its value at broadside, $|F_A(90°)|$. For example, using Figure A.4(a), the beamwidths are approximately 60°, 35°, 25°, and 15°, for the 2-, 3-, 4-, and 8-element arrays, respectively.

Array Bandwidth

The element bandwidth, defined in Section A.3, can limit the array bandwidth. However, the effect of using phase shifters to scan the beam, instead of time-delay devices, on the array bandwidth can be more substantial. In practice, when phase shifters are used, the beam is scanned to the desired angle only at the center frequency, f_0. Otherwise, the beam peak angle is reduced for frequencies above f_0 and increased for frequencies below it. The array bandwidth becomes smaller as the scan angle is increased or the array size is increased [Mailloux, 1994].

A.5.2 Planar Antenna Arrays

A planar antenna array is an array where all elements lie in a plane. Without loss of generality, the this plane may be assumed to be the xy-plane. Figure A.10 depicts the layout of antenna elements in a planar array composed of $N_x = 4$ elements in the x direction and $N_y = 5$ in the y direction. Array elements are uniformly-spaced by d_x and d_y are the spacings along the x and y axes, respectively. The isotropic array factor of a planar antenna array is obtained by extending the array factor of the linear antenna array, given in Equation A.12, to two dimensions. Therefore, it is given by [Rulf and Robertshaw, 1987]:

$$F_A(\theta, \phi) = \sum_m \sum_n a_{mn} e^{jk(md_x \sin\theta \cos\phi + nd_y \sin\theta \sin\phi)}, \tag{A.18}$$

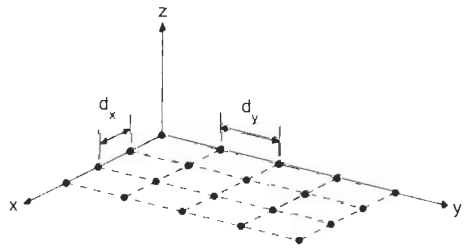

Figure A.10: The layout of elements in a planar antenna array. The number of elements along the x and y directions are $N_x = 4$ and $N_y = 5$, respectively.

where $m = 0, 1, \ldots, (N_x - 1)$, $n = 0, 1, \ldots, (N_y - 1)$, and a_{mn} is the relative excitation of the element at row m and column n in the array. Equation A.18 can be rewritten in terms of the angular variables $u = \sin\theta\cos\phi$ and $v = \sin\theta\sin\phi$. Therefore:

$$F_A(u, v) = \sum_m \sum_n a_{mn} e^{jk(md_x u + nd_y v)}. \tag{A.19}$$

Figure A.11(a) shows a linear-scale spherical plot of the isotropic array factor, $F_A(\theta, \phi)$, of the planar array illustrated in Figure A.10, with $d_x = d_y = \lambda/2$, versus θ and ϕ. Figure A.11(b) shows a surface plot of $F_A(u, v)$ versus u and v.

The main beam of a planar array can be scanned to a direction (θ_0, ϕ_0), by adding a phase shift of $(mkd_x \sin\theta_0 \cos\phi_0 + nkd_y \sin\theta_0 \sin\phi_0)$ to the element at row m and column n in the array. The array factor is, therefore, expressed as:

$$\begin{aligned} F_A(\theta, \phi) &= \sum_m \sum_n a_{mn} e^{jk\left(md_x(\sin\theta\cos\phi - \sin\theta_0\cos\phi_0) + nd_y(\sin\theta\sin\phi - \sin\theta_0\sin\phi_0)\right)}, \\ F_A(u, v) &= \sum_m \sum_n a_{mn} e^{jk(md_x(u-u_0) + nd_y(v-v_0))}, \end{aligned} \tag{A.20}$$

where $u_0 = \sin\theta_0\cos\phi_0$ and $v_0 = \sin\theta_0\sin\phi_0$. Figures A.12(a) and A.12(b) show linear-scale spherical and surface plots of F_A when the planar array illustrated in Figure A.10 is scanned to $(\theta_0, \phi_0) = (10°, 30°)$. Other concepts introduced in Section

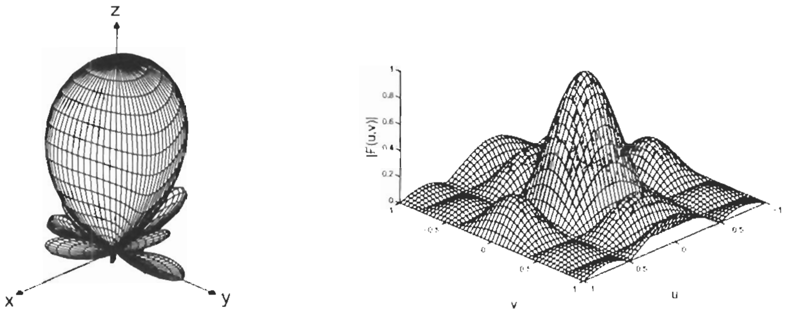

(a) Spherical plot (b) Surface plot

Figure A.11: Linear-scale spherical and surface plots of the isotropic array factor of a broadside planar antenna array with $N_x = 4$, $N_y = 5$, and $d_x = d_y = \frac{\lambda}{2}$.

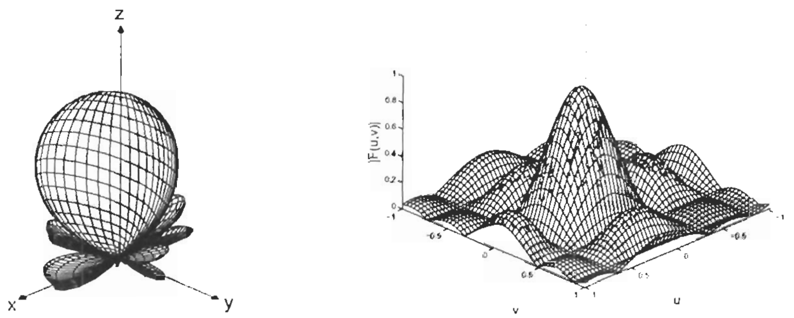

(a) Spherical plot

(b) Surface plot

Figure A.12: Linear-scale spherical and surface plots of the isotropic array factor of a planar antenna array with $N_x = 4$, $N_y = 5$, and $d_x = d_y = \frac{\lambda}{2}$, which is scanned to $(\theta_0, \phi_0) = (10^\circ, 30^\circ)$.

A.5.1 for linear arrays, such as directivity, can be extended to planar arrays in a similar manner.

A.5.3 Scanning Limitations

Since beam scanning is such an integral part of this work, it is worthwhile to summarize the effects and limitations of scanning. As the main beam is scanned away from broadside, the array beamwidth is increased and grating lobes may begin to form, which results in decreasing the array directivity and gain. Scanning may also decrease the array bandwidth.

Additionally, the impact of mutual coupling increases as a result of scanning. Therefore, although impedance matching may be achieved at broadside, scanning will result in impedance mismatch. This reduces the antenna efficiency, as shown in Section A.3. The effects of scanning may be so severe, to the extent of causing array blindness. Array blindness results from the increased impact of mutual coupling and may cause complete cancellation of the array beam at certain scan angles [Mailloux, 1994].

Appendix B

Numerical Solution Methods

This appendix presents the numerical solution methods used in Section 2.3 to compute the face elevation of pyramidal and pyramidal frustum antenna.

The Equalization-based Approach

The face elevation of the pyramidal frustum is computed using the equalization-based approach by numerically solving the system of non-linear design equations in (2.12) using Maple$^{\text{TM}}$ as follows:

```
solution := fsolve({eq1, eq2}, {psi_f, theta_b},
            {psi_f=0..theta_2, theta_b=theta_1..theta_2});
```

where `eq1` and `eq2` represent the two equations in (2.12).

The Minimax-based Approach

The face elevation of the pyramid is computed using the minimax-based approach using the `fmininmax` function in MATLAB$^{\text{TM}}$as follows:

```
options = optimset('MinAbsMax', 2);
[x, fval] = fminimax(@find_max_scan,[0],[],[],[],[],[0],
            [90],[],options);
gamma_p = max(fval); psi_p = x;
```

where `find_max_scan` is a custom function that returns a 2-element vector containing γ_{p_1} and γ_{p_2}, given by (2.5), in degrees.

One of the pitfalls of `fminimax` is that the function to be minimized must be continuous. This is not the case for the pyramidal frustum because γ_{f_1} in (2.6) is actually computed as:

$$\gamma_{f_1} = \begin{cases} \theta_b & \text{if } \theta_b > \theta_1 \\ 0 & \text{otherwise.} \end{cases}$$

Therefore, custom C code was written to perform a two-dimensional linear search in ψ_f and θ_b to find the global minimum of γ_f as defined by (2.16). The pseudo-code of the method used is listed below.

```
increment = 0.05            # radians
$\gamma_{f_{\text{opt}}} = 10000$
$\theta_b = \theta_1$
while $\theta_b < \theta_2$
    $\psi_f = 0$
    while $\psi_f < \frac{\pi}{2}$
        if $\theta_b \leqslant \theta_1$, then $\gamma_{f_1} = 0$
        else Compute $\gamma_{f_1}$ using (2.6)
        end
        Compute $\gamma_{f_2}$ and $\gamma_{f_3}$ using (2.8)
        $\gamma_f = \min(\gamma_{f_1}, \gamma_{f_2}, \gamma_{f_3})$
        if $\gamma_f < \gamma_{f_{\text{opt}}}$, then
            $\gamma_{f_{\text{opt}}} = \gamma_f$
            $\psi_{f_{\text{opt}}} = \psi_f$
            $\theta_{b_{\text{opt}}} = \theta_b$
        end
        $\psi_f = \psi_f$ + increment
    end
    $\theta_b = \theta_b$ + increment
end
Output the optimal parameters: $\gamma_{f_{\text{opt}}}$, $\psi_{f_{\text{opt}}}$, $\theta_{b_{\text{opt}}}$
```

Appendix C

Dimensions of Multi-Faceted Antenna Arrays

This appendix describes how the dimensions of pyramidal and pyramidal frustum antenna arrays are computed, given that their bases fit inside a circular footprint of constant radius, R. These dimensions are valid only for connected, rather than non-connected, planar facets are connected, as explained in Section 1.1.1.

C.1 Pyramid Dimensions

Figure C.1(a) illustrates the geometry of a 5-face pyramidal antenna array used here as an example to show how the pyramid dimensions are determined. Each side face subtends an azimuthal angle, ϕ_s, given by:

$$\phi_s = \frac{2\pi}{N}. \tag{C.1}$$

Since all side faces of the pyramids are identical, only the first face needs to be considered, as shown in Figure C.1(b), and the footprint of radius $R=||\overline{op_2}||$. The apothem of the pyramid base, a, shown in Figure C.1(c) is given by:

$$a = ||\overline{op_4}|| = R\cos\frac{\phi_s}{2}. \tag{C.2}$$

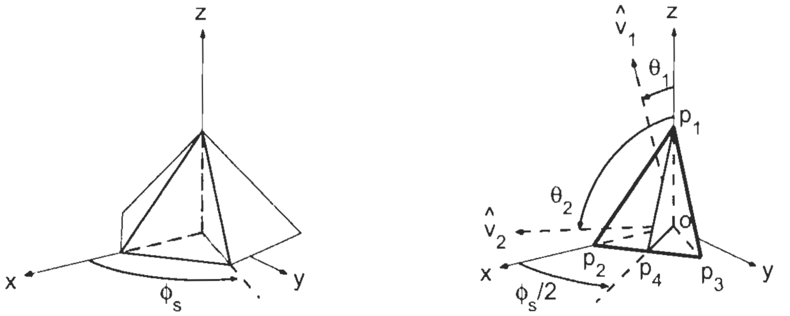

(a) A 5-face pyramid (b) The first face of the pyramid

(c) Pyramid face elevation (d) The circular array supported by the face

Figure C.1: The geometry of a 5-face pyramidal array.

Each face supports a circular antenna array of radius r, as shown in Figure C.1(d), and the pyramid may or may not be truncated just above the arrays. The width and height of the side face, w_s and h_s, are given by:

$$\begin{aligned} w_s &= ||\overline{p_2p_3}|| = 2||\overline{p_2p_4}|| = 2R\sin\tfrac{\phi_s}{2}, \\ h_s &= ||\overline{p_1p_4}|| = \tfrac{a}{\cos\psi_p} = \tfrac{R\cos\frac{\phi_s}{2}}{\cos\psi_p}. \end{aligned} \tag{C.3}$$

The areas of the whole pyramid face, i.e., the triangle $\Delta p_1p_2p_3$ is thus given by:

$$A_\Delta = \frac{1}{2}w_sh_s = \frac{R^2\sin\phi_s}{2\cos\psi_p}, \tag{C.4}$$

and the radius, r, of the circular array (the circle inscribed inside $\Delta p_1p_2p_3$) is given by:

$$r = \frac{A_\Delta}{s}, \qquad s = \frac{1}{2}\left(\sqrt{4h_s^2 + w_s^2} + w_s\right), \tag{C.5}$$

where s is the semiperimeter of the triangle $\Delta p_1p_2p_3$ [Weisstein, 2003].

The area of the circular array is thus given by:

$$A = \pi r^2. \tag{C.6}$$

When the array antenna is scanned by an angle γ_p away from its broadside direction, $\hat{n}_{p_1}$, the minimum projected area of the circular array in (C.4) is given by:

$$A_{\min} = A \cos \gamma_p. \tag{C.7}$$

Finally, the total pyramid height, H, and the truncated pyramid height, H_t, shown in Figure C.1(c) are given by:

$$\begin{aligned} H &= h_s \sin \psi_p, \\ H_t &= 2r \sin \psi_p. \end{aligned} \tag{C.8}$$

C.2 Pyramidal Frustum Dimensions

Figure C.2(a) illustrates the geometry of a 6-face pyramidal frustum antenna array. Each side face of the frustum subtends an azimuthal angle, ϕ_s, given by:

$$\phi_s = \frac{2\pi}{N-1}. \tag{C.9}$$

Owing to symmetry, only the first side face and part of the top face need to be considered, as shown in Figure C.2(b).

Similar to the pyramid, the footprint radius is $R{=}||\overline{op_2}||$, and the width and height of the triangle $\Delta p_1 p_2 p_3$ containing the side of the frustum (the isosceles trapezoid $p_2 p_3 p_6 p_5$) are given by:

$$\begin{aligned} w_s &= ||\overline{p_2 p_3}|| = 2||\overline{p_2 p_4}|| = 2R \sin \tfrac{\phi_s}{2}, \\ h_s &= ||\overline{p_1 p_4}|| = \tfrac{R \cos \frac{\phi_s}{2}}{\cos \psi_f}. \end{aligned} \tag{C.10}$$

It is assumed that identical circular arrays are used on the top and side faces of the frustum. In general, for a given array radius, r, it can either be inscribed in the top face only (Figure C.3(a)), or in the side face only (Figure C.3(b)). The radius of the circle inscribed in the top face, which is an (N-1)-sided regular polygon is given by:

$$r_t = \frac{w_t}{2} \cot \frac{\phi_s}{2}, \tag{C.11}$$

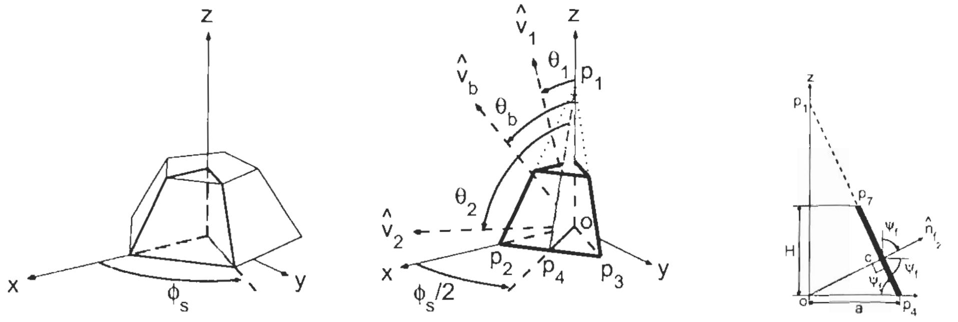

(a) A 6-face frustum (b) First and top faces of the frustum (c) Frustum face elevation

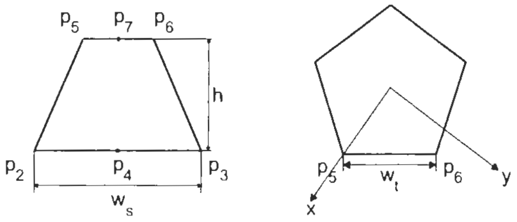

(d) Side face (e) Top face

Figure C.2: The geometry of a 6-face pyramidal frustum array.

where w_t is the side length of the top face as shown in Figure C.2(e).

For the side face, it is only possible to inscribe a circle inside an isosceles trapezoid if, and only if, $h = \sqrt{w_s w_t}$, in which case, the circle radius is equal to $h/2$. If $h > \sqrt{w_s w_t}$, the largest circle that fits inside the trapezoid touches only $\overline{p_2p_3}$, $\overline{p_2p_5}$, and $\overline{p_3p_6}$. On the other hand, if $h < \sqrt{w_s w_t}$, the largest circle that fits inside the trapezoid touches only $\overline{p_2p_3}$ and $\overline{p_5p_6}$. Therefore, the radius, r_s of the largest circle that fits inside the side face is given by:

$$\begin{aligned} r_s &= \min(r_{s_1}, r_{s_2}), \\ r_{s_1} &= \frac{A}{s} = \frac{\frac{1}{2}w_s h_s}{\frac{1}{2}\left(\sqrt{4h_s^2 + w_s^2} + w_s\right)}, \quad h > \sqrt{w_s w_t}, \\ r_{s_2} &= \frac{h}{2}, \quad h \leqslant \sqrt{w_s w_t}, \end{aligned} \tag{C.12}$$

where A is the area of the triangle $\Delta p_1 p_2 p_3$ and s is its semiperimeter.

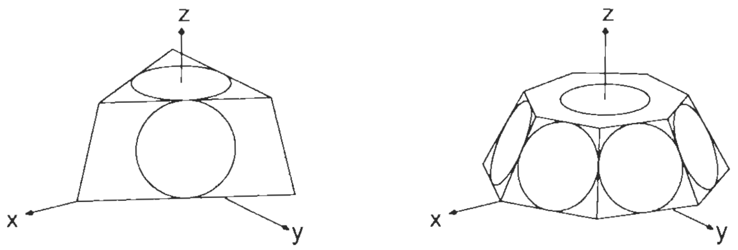

(a) Circle inscribed in top face only (b) Circle inscribed in side face only

Figure C.3: Inscribing circular arrays on the top and side faces of pyramidal frusta.

By equating (C.11) and (C.12), two possible values are obtained for w_t:

$$\begin{aligned} w_{t_1} &= \frac{h_s w_s \tan\frac{\phi_s}{2}}{w_s + h_s \tan\frac{\phi_s}{2}}, \quad r_t = r_{s_1}, \\ w_{t_2} &= \frac{2h_s w_s \tan\frac{\phi_s}{2}}{w_s + 2\sqrt{h_s^2 + \frac{w_s^2}{4}}}, \quad r_t = r_{s_2}; \end{aligned} \tag{C.13}$$

and w_t is set to $\min(w_{t_1}, w_{t_2})$. The array radius, r, and the trapezoid height, $h = ||\overline{p_4 p_7}||$, are then computed using:

$$\begin{aligned} r &= \tfrac{w_t}{2} \cot \tfrac{\phi_s}{2}, \\ h &= 2r. \end{aligned} \tag{C.14}$$

If w_t=$\min(w_{t_1}, w_{t_2})$=w_{t_2}, then w_t is adjusted by setting it to h^2/w_s, which is the case shown in Figure C.3(b). Finally, the height of the pyramidal frustum, H, shown in Figure C.2(c) is computed using:

$$H = h \sin \psi_f. \tag{C.15}$$

C.3 The Maximum Scan Angle at a Finite Distance to the Antenna

C.3.1 Pyramidal Arrays

The derivation in Section 2.3 assumed that the distance from the target to the antenna is sufficiently large. For a pyramidal array, this case is illustrated in Figure C.4(a),

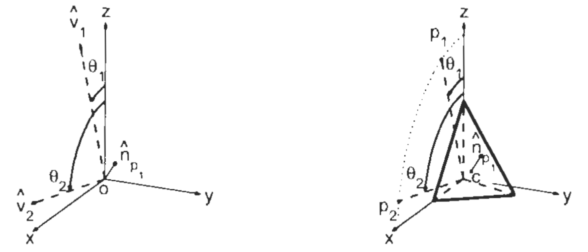

(a) Infinite hemisphere radius (b) Finite hemisphere radius

Figure C.4: Computing the maximum scan angle at (a) infinite, and (b) finite distances from the target to the antenna.

where the antenna dimensions are neglected. The unit vectors $\hat{n}_{p_1}$, $\hat{v}_1$, and $\hat{v}_2$ are thus given by (2.3) and the maximum scan angle is computed using (2.5).

When finite distances are considered, as discussed in Section 2.4, the antenna dimensions cannot be neglected. This case is illustrated in Figure C.4(b). In this case, the maximum scan angle occurs when the beam is scanned from the center of the array, $\mathbf{c}$, along the broadside direction, $\hat{n}_{p_1}$, to either of the points $\mathbf{p_1}$ or $\mathbf{p_2}$. The unit vector $\hat{n}_{p_1}$ is still given by (2.3) and the points $\mathbf{c}$, $\mathbf{p_1}$, and $\mathbf{p_2}$ are given by:

$$\begin{aligned} \mathbf{c} &= \left[(a - r\cos\psi_p)\cos\phi_s/2 \quad (a - r\cos\psi_p)\sin\phi_s/2 \quad r\sin\psi_p\right]^T, \\ \mathbf{p_1} &= d \times \left[\sin\theta_1 \quad 0 \quad \cos\theta_1\right]^T, \\ \mathbf{p_2} &= d \times \left[\sin\theta_2 \quad 0 \quad \cos\theta_2\right]^T, \end{aligned} \tag{C.16}$$

where ϕ_s, a, and r are given by (C.1), (C.2), and (C.5), respectively. d is the hemisphere radius, i.e., the distance from the target to the origin. Therefore, the maximum scan angle occurs when scanning the beam from $\hat{n}_{p_1}$ to the directions $\mathbf{u_1}$ and $\mathbf{u_2}$ given by:

$$\mathbf{u_i} = \mathbf{p_i} - \mathbf{c}, \quad i = 1, 2 \tag{C.17}$$

The individual scan angles, γ_{p_1} and γ_{p_2} are computed using:

$$\gamma_{p_i} = \cos^{-1} \hat{n}_{p_1} \cdot \frac{\mathbf{u_i}}{||\mathbf{u_i}||}. \tag{C.18}$$

Finally, the maximum scan angle, γ_p, is computed using:

$$\gamma_p = \max_{i=1,2} \gamma_{p_i}. \tag{C.19}$$

C.3.2 Pyramidal Frustum Arrays

The maximum scan angle at a finite distance to the pyramidal frustum can be computed in a similar manner. For the top face, the angle γ_{f_1}, is computed using:

$$\gamma_{f_1} = \cos^{-1} \hat{n}_{f_1} \cdot \frac{\mathbf{u_1}}{||\mathbf{u_1}||}, \tag{C.20}$$

where

$$\begin{aligned} \mathbf{u_1} &= \mathbf{p_b} - \mathbf{c_1}, \\ \mathbf{c_1} &= \begin{bmatrix} 0 & 0 & H \end{bmatrix}^T, \\ \mathbf{p_b} &= d \times \begin{bmatrix} \sin\theta_b & 0 & \cos\theta_b \end{bmatrix}^T, \end{aligned} \tag{C.21}$$

and H is given by (C.15).

For the side face, the angles γ_{f_2} and γ_{f_3} are computed using:

$$\begin{aligned} \gamma_{f_2} &= \cos^{-1} \hat{n}_{f2} \cdot \tfrac{\mathbf{u_2}}{||\mathbf{u_2}||}, \\ \gamma_{f_3} &= \cos^{-1} \hat{n}_{f2} \cdot \tfrac{\mathbf{u_3}}{||\mathbf{u_3}||}, \end{aligned} \tag{C.22}$$

where

$$\begin{aligned} \mathbf{u_2} &= \mathbf{p_b} - \mathbf{c_2}, \\ \mathbf{u_3} &= \mathbf{p_2} - \mathbf{c_2}, \\ \mathbf{c_2} &= \begin{bmatrix} (a - r\cos\psi_f)\cos\phi_s/2 & (a - r\cos\psi_f)\sin\phi_s/2 & r\sin\psi_f \end{bmatrix}^T, \\ \mathbf{p_2} &= d \times \begin{bmatrix} \sin\theta_2 & 0 & \cos\theta_2 \end{bmatrix}^T. \end{aligned} \tag{C.23}$$

ϕ_s, r, and $\hat{n}_{f_2}$ are given by (C.9), (C.14), and (2.7), respectively. The overall maximum scan angle, γ_f, is computed using:

$$\gamma_f = \max_{i=1,2,3} \gamma_{f_i}. \tag{C.24}$$

Bibliography

Balanis, C. A., *Advanced Engineering Electromagnetics*, John Wiley & Sons, 1989.

Basilio, L. I., Williams, J. T., Jackson, D. R., and Khayat, M. A., A comparative study of a new GPS reduced-surface-wave antenna, *IEEE Antennas and Wireless Propagation Letters*, 4:233–236, 2005.

Bell Laboratories, ABM research and development at Bell Laboratories: Project history, http://srmsc.org/ref1020.html, 1975.

Boccia, L., Amendola, G., and Massa, G. D., A shorted elliptical patch antenna for GPS applications, *IEEE Antennas and Wireless Propagation Letters*, 2:6–8, 2003.

Borwein, J. M. and Lewis, A. S., *Convex Analysis and Nonlinear Optimization Theory and Examples*, Springer, 2000.

Brandwood, D. H., Phase steering for modified dodecahedral array for mobile SATCOMs, In *IEE Colloquium On Electronic Beam Steering*, pages 6/1–6/6, London, UK, October 28 1998.

Caille, G., Vourch, E., Martin, M., Mosig, J., and Polegre, M., Conformal array antenna for observation platforms in low earth orbit, *IEEE Antennas and Propagation Magazine*, 44(3):103–104, June 2002.

Carr, J. J., *Practical Antenna Handbook*, McGraw-Hill, 1998.

Chair, R., Lee, K. F., and Luk, K. M., Bandwidth and cross-polarization characteristics of quarter-wave shorted patch antennas, *Microwave and Optical Technology Letters*, 22(2):101–103, July 1999.

Corey, L. E., A graphical technique for determining optimal array antenna geometry, *IEEE Transactions on Antennas and Propagation*, 33(7):719–726, July 1985.

Derneryd, A. G., Analysis of the microstrip disk antenna element, *IEEE Transactions on Antennas and Propagation*, 27(5):660–664, September 1979.

Elliott, R. S., *Antenna Theory and Design*, Wiley-IEEE Press, 2003.

Felstead, E. B., Optimum combining of multiple shipboard SATCOM antennas for hemispheric coverage, In *IEEE 21st Century Military Communications Conference, MILCOM 2000*, volume 1, pages 604–608, McLean, VA, October 22-25 2000.

Fourikis, N., *Phased Array-Based Systems and Applications*, John Wiley & Sons, 1997.

Giorgi, G., Guerraggio, A., and Thierfelder, J., *Mathematics of Optimization: Smooth and Nonsmooth Case*, Elsevier, 2004.

Hall, P. S., Dahele, J. S., and James, J. R., Design principles of sequentially fed, wide bandwidth, circularly polarised microstrip antennas, *IEE Proceedings - Microwaves, Antennas and Propagation*, 135(5):381–389, October 1989.

Hansen, R. C., Cross polarization of microstrip patch antennas, *IEEE Transactions on Antennas and Propagation*, 35(6):731–732, June 1987.

Hansen, R. C., *Phased Array Antennas*, John Wiley & Sons, 1998.

Haupt, R. L., Interleaving thinned sum and difference linear arrays, In *Proceedings of the IEEE Antennas and Propagation Society Symposium*, pages 4773–4776, Albuquerque, NM, July 9-14 2006.

Hoft, D. J., Solid state transmit/receive module for the PAVE PAWS (AN/FPS-115) phased array radar, *MTT-S International Microwave Symposium Digest*, 78(1):239–241, June 1978.

Hollis, J. S., Lyon, T. J., and L. Clayton, J., editors, *Microwave Antenna Measurements*, Scientific Atlanta, Inc., Atlanta, GA, 1970.

Huang, J., Circularly polarized conical patterns from circular microstrip antennas, *IEEE Transactions on Antennas and Propagation*, 32(9):991–994, September 1984.

IEEE standard test procedures for antennas, IEEE Std. 149, 1979.

IEEE standard definitions of terms for antennas, IEEE Std. 145, 1983.

Ihara, T., Manabe, T., Iigusa, K., Kijima, T., Murakami, Y., and Iwasaki, H., Switched four-sector beam antenna for indoor wireless LAN systems in the 60 GHz band, In *Proceedings of the Topical Symposium on Millimeter Waves*, pages 115–118, Tokyo, Japan, July 7-8 1997.

Imbriale, W. A., *Large Antennas of the Deep Space Network*, John Wiley & Sons, 2003.

Jablon, A. R. and Agrawal, A., Optimal number of array faces for active phased array radars, In *Proceedings of the IEEE Antennas and Propagation Society Symposium*, volume 4, pages 4096–4099, Monterey, CA, June 20-25 2004.

Jablon, A. R. and Agrawal, A., Optimal number of array faces for active phased array radars. *IEEE Transactions on Aerospace and Electronic Systems*, 42(1):351–360, January 2006.

James, J. R., Hall, P. S., and Wood, C., *Microstrip Antenna Theory and Design*, IEE Peter Peregrinus, 1981.

Jamnejad, V., Huang, J., Levitt, B., Pham, T., and Cesarone, R., Array antennas for JPL/NASA deep space network, In *Proceedings of the IEEE Aerospace Conference*, volume 2, pages 911–921, Big Sky, MT, March 9-16 2002.

Josefsson, L. and Persson, P., *Conformal Array Antenna Theory and Design*, Wiley-IEEE Press, 2006.

Kajiwara, A., Circular polarization diversity with passive reflectors in indoor radio channels, *IEEE Transactions on Vehicular Technology*, 49(3):778–782, May 2000.

Kefalas, G. P., A phased-array ground terminal for satellite communications, *IEEE Transactions on Communication Technology*, 13(4):512–525, December 1965.

Khalifa, I. and Vaughan, R., Bounds on the distributed circular polarization purity of ring sources for broadside mode circular patch antennas, In *Proceedings of the IEEE Antennas and Propagation Society Symposium*, pages 1533–1536, Albuquerque, NM, July 9-14 2006.

Khalifa, I. and Vaughan, R., Optimizing the geometry of pyramidal antenna arrays for hemispherical scan coverage, In *Proceedings of the IEEE Antennas and Propagation Society Symposium*, pages 2233–2236, Albuquerque, NM, July 9-14 2006.

Khalifa, I. and Vaughan, R., Geometric design of pyramidal antenna arrays for hemispherical scan coverage, *To appear in the IEEE Transactions on Antennas and Propagation*, in press.

Kim, Y. U. and Elliott, R. S., Extensions of the tseng-cheng pattern synthesis technique, *Journal of Electromagnetic Waves and Applications*, 2(3/4):255–268, March 1988.

Kishk, A. A. and Shafai, L., The effect of various parameters of circular microstrip antennas on their radiation efficiency and the mode excitation, *IEEE Transactions on Antennas and Propagation*, 34(8):969–976, August 1986.

Kmetzo, J. L., An analytical approach to the coverage of a hemisphere by N planar phased arrays, *IEEE Transactions on Antennas and Propagation*, 15(3):367–371, May 1967.

Knittel, G. H., Choosing the number of faces of a phased-array antenna for hemisphere scan coverage, *IEEE Transactions on Antennas and Propagation*, 13(6):878–882, November 1965.

Knittel, G. H., Hessel, A., and Oliner, A. A., Element pattern nulls in phased arrays and their relationship to guided waves, *Proceedings of the IEEE*, 56(11):1822–1836, November 1968.

Madsen, K. and Schjær-Jacobsen, H., A nonlinear minimax optimization program not requiring derivatives, *IEEE Transactions on Antennas and Propagation*, 25(3):454–456, May 1977.

Mailloux, R. J., *Phased Array Antenna Handbook*, Artech House, 1994.

Martin, E. J., Radiation fields of circular loop antennas by a direct integration process, *IEEE Transactions on Antennas and Propagation*, 8(1):105–107, January 1960.

Miura, A., Yamamoto, S., Li, H., Tanaka, M., and Wakana, H., *ka*-band aeronautical satellite communications experiments using COMETS, *IEEE Transactions on Vehicular Technology*, 51(5):1153–1164, September 2002.

Napier, P. J., Thompson, A. R., and Ekers, R. D., The very large array: Design and performance of a modern synthesis radio telescope, *Proceedings of the IEEE*, 71(11):1295–1320, November 1983.

Padros, N., Ortigosa, J. I., Baker, J., Iskander, M. F., and Thornberg, B., Comparative study of high-performance GPS receiving antenna designs, *IEEE Transactions on Antennas and Propagation*, 45(4):698–706, April 1997.

Pozar, D. M., General relations for a phased array of printed antennas derived from infinite current sheets, *IEEE Transactions on Antennas and Propagation*, 33(5):498–504, May 1985.

Pozar, D. M. and Schaubert, D. H., Scan blindness in infinite phased arrays of printed dipoles, *IEEE Transactions on Antennas and Propagation*, 32(6):602–610, June 1984.

Rulf, B. and Robertshaw, G. A., *Understanding Antennas for Radar, Communications, and Avionics*, Van Nostrand Reinhold Company, 1987.

Sharp, E. D., A triangular arrangement of planar-array elements that reduces the number needed, *IEEE Transactions on Antennas and Propagation*, 9(2):126–129, May 1961.

Smith, M. S. and Hall, P. S., Analysis of radiation pattern effects in sequentially rotated arrays, *IEE Proceedings - Microwaves, Antennas and Propagation*, 141(4):313–320, August 1994.

Stutzman, W. L., *Polarization in Electromagnetic Systems*, Artech House, 1993.

Targonski, S. D., Design of a multiband antenna for satellite communications on the move, In *Proceedings of the IEEE Antennas and Propagation Society Symposium*, volume 3, pages 3011–3014, Monterey, CA, June 20-25 2004.

Trunk, G. V., Optimal number of phased array faces for horizon and volume surveillance - revisited, In *IEEE International Symposium on Phased Array Systems and Technology*, pages 124–129, Boston, MA, October 14-17 2003.

Trunk, G. V. and Patel, D. P., Optimal number of phased array faces and signal processors for horizon surveillance, *IEEE Transactions on Aerospace and Electronic Systems*, 33(3):1002–1006, July 1997.

Vaughan, R. G., Two-port higher mode circular microstrip antennas, *IEEE Transactions on Antennas and Propagation*, 36(3):309–321, March 1988.

Vaughan, R. G. and Andersen, J. B., *Channels, Propagation and Antennas for Mobile Communications*, The IEE Press, 2003.

Waterhouse, R. B., *Microstrip Patch Antennas - A Designer's Guide*, Kluwer Academic Publishers, 2003.

Waters, W. M., Patel, D. P., and Trunk, G. V., Optimal number of faces of a volume-scanning active array radar, *IEEE Transactions on Aerospace and Electronic Systems*, 34(3):1032–1037, July 1998.

Weisstein, E. W., *CRC Concise Encyclopedia of Mathematics, Second Edition*, Chapman & Hall/CRC, 2003.

Wheeler, H. A., Simple relations derived from a phased-array antenna made of an infinite current sheet, *IEEE Transactions on Antennas and Propagation*, 13(4):506–514, July 1965.

Wong, K. and Chiou, T., Broad-band single-patch circularly polarized microstrip antenna with dual capacitively coupled feeds, *IEEE Transactions on Antennas and Propagation*, 49(1):41–44, January 2001.

Wright, H. C., *An Introduction to Antenna Theory*, Bernard Babani Ltd., 1987.

Yang, F. and Rahmat-Samii, Y., A reconfigurable patch antenna using switchable slots for circular polarization diversity, *IEEE Microwave and Wireless Components Letters*, 12(3):96–98, March 2002.